UNIVERSIDADE FEDERAL DE PERNAMBUCO
CENTRO DE CIÊNCIAS EXATAS E DA NATUREZA
PROGRAMA DE PÓS-GRADUAÇÃO EM FÍSICA

ARTHUR CÉSARE MESSIAS VIANA PEREIRA

PHOTOACOUSTIC AND TERAHERTZ TECHNIQUES APPLIED TO BIOPHOTONICS AND PHOTONIC DEVICES IN STUDIES IN 2D MATERIALS

Recife
2025

ARTHUR CÉSARE MESSIAS VIANA PEREIRA

PHOTOACOUSTIC AND TERAHERTZ TECHNIQUES APPLIED TO BIOPHOTONICS AND PHOTONIC DEVICES IN STUDIES IN 2D MATERIALS

Tese apresentada ao Programa de Pós-Graduação em Física da Universidade Federal de Pernambuco, como requisito parcial para obtenção do título de Doutor em Física.

Área de concentração: Óptica.

Orientador: Prof. Dr. Anderson Stevens Leônidas Gomes

Recife

2025

.Catalogação de Publicação na Fonte. UFPE - Biblioteca Central

Pereira, Arthur Cesare Messias Viana.
Photoacoustic and terahertz techniques applied to biophotonics and photonic devices in studies in 2D materials / Arthur Cesare Messias Viana Pereira. - Recife, 2025.
101f.: il.

Tese (Doutorado) - Universidade Federal de Pernambuco, Centro de Ciências Exatas e da Natureza, Programa de Pós-Graduação em Física, 2025.
Orientação: Anderson Stevens Leonidas Gomes.
Inclui referências e apêndices.

1. Photoacoustics; 2. Terahertz; 3. Photoacoustic Imaging; 4. Nanomaterials. I. Gomes, Anderson Stevens Leonidas. II. Título.

UFPE-Biblioteca Central

ARTHUR CÉSARE MESSIAS VIANA PEREIRA

PHOTOACOUSTIC AND TERAHERTZ TECHNIQUES APPLIED TO BIOPHOTONICS AND PHOTONIC DEVICES IN STUDIES IN 2D MATERIALS

Tese apresentada ao Programa de Pós-Graduação em Física da Universidade Federal de Pernambuco, como requisito parcial para a obtenção do título de Doutor em Física.

Área de Concentração: Óptica

Data de aprovação: 30/05/2025.

BANCA EXAMINADORA

_____

Prof. Dr. Anderson Stevens Leônidas Gomes
Orientador
Universidade Federal de Pernambuco

_____

Prof. Dr. Cid Bartolomeu de Araújo
Examinador Interno
Universidade Federal de Pernambuco

_____

Prof. Dr. Marcio Heraclyto Gonçalves de Miranda
Examinador Interno
Universidade Federal de Pernambuco

_____

Prof. Dr. André de Lima Moura
Examinador Externo
Universidade Federal de Alagoas

_____

Profa. Dra. Ingrid David Barcelos
Examinadora Externa
Centro Nacional de Pesquisa em Energia e Materiais

ACKNOWLEDGMENTS

Firs of all, I would like to thank all my heart to my family, for absolutely everything. I'm grateful to everyone who supported me and believed in me, even in the bad times. My mother, father, brother, sister, nephews… I wouldn't have done without all your love and support. There is no word and action that can express how grateful I am to each of you. Thank you!

To my amazing girlfriend, Bruna, for her affection, understanding, and for always being present despite the distance. You always pushed me to the next level and always believed in me. I also extend this acknowledgement to her family, in special Pituco. I love this dog.

To my advisor, prof. Anderson Gomes, for all the support through these 6 years. I am really grateful for the opportunity to work with such an outstanding researcher and person. Thank you for all the lessons and advice. For sure, you are a big reference for me.

To my co-advisor, prof. Roberto Morandotti, for accepting me as an intern and for all contributions to this work.

Of course, it's impossible to forget everyone who made my days happier and funnier. Everyone in LABFOTON: Rosana, Denise, Alyson, Edwin, Emanuel, Cecilia, Jessica, Igor. All of you have a special place in my heart. Thank you for every laugh, joke… You guys are amazing. This lab is unique and special because of each one of you.

To every friendship that I've made in Montreal: Mohammad, Safa, Madhu and, of course, all the POSs: Roberto, Mr. Pochapski, Amine, Gabriele, Merlyn and Zhuohong. This one-year experience was outstanding, and you guys are one of the reasons why.

To every friend that supported me, even before my master's degree, and still have no idea of what I'm doing: Tiago, João Pedro, Breno, Felipe, Dimas, Guilherme, João Paulo, Pedro Ivo.

I also would like to thank Túlio, not only the friendship, but for every conversation and every help. My stay in Montreal was easier also because of you.

The Professors of the Physics Department for their contribution spending in conversations about physics in the corridors of the department and/or in the seminars. Also, to all professors from the classes that I was enrolled in. Administrative staff, particularly Alexsandra Soares, who was always supporting me in any urgent procedure we need. Thanks to Valdomiro da Silva and João de Paula Filho from the mechanics shop by the design of several of the pieces used in the experiments.

Last but not least, to CAPES, for financial support.

ABSTRACT

Nowadays, technological advancements demand smaller, faster, and more efficient devices. This makes nanomaterials essential, as they offer innovative solutions by enhancing performance at the nanoscale and driving the development of new materials. Their applications span a wide range of fields, from next-generation transistors and flexible electronics to high-efficiency solar cells and advanced drug delivery systems. However, one of the major challenges in working with nanomaterials is their characterization, which requires contactless and non-destructive techniques. The electronic, structural, and optical properties of these materials are crucial for the future of materials science. This thesis, divided into five chapters, presents results obtained using two powerful techniques for characterizing different types of two-dimensional (2D) materials: photoacoustics (PA) and terahertz (THz) spectroscopy. Both methods are widely employed in imaging and material analysis. Following the introduction in Chapter 1, Chapter 2 provides a brief review of absorption and refraction, serving as a simple reminder. Chapter 3 is dedicated to photoacoustics, explaining the underlying phenomena, relevant equations, and applications. Photoacoustic microscopy (PAM) is introduced, and results obtained in the laboratory using this setup are presented for four different types of nanoparticles: titanium nitride (TiN), gold nanoparticles (nanospheres and nanorods), erbium-ytterbium (Er^{3+}–Yb^{3+}) co-doped nanoparticles, and an iron oxide (Fe_3O_4) nanocomposite (Fe_3O_4@βCD-PHY). All images acquired using PAM demonstrated excellent resolution and contrast. Moreover, the diversity in optical and electronic properties among the samples confirms the versatility and effectiveness of photoacoustic microscopy. Chapter 4 explores terahertz experiments, particularly Terahertz Time-Domain Spectroscopy (THz-TDS). It presents the theory behind the generation and detection of THz radiation, along with applications within this low-frequency range of the electromagnetic spectrum. Results include the characterization of 2D transition metal dichalcogenides (TMDs) and the design of a continuously tunable filter for THz telecommunication systems. Finally, Chapter 5 outlines future work to be carried out in upcoming THz experiments. Through these chapters, this work aims to contribute to the rapidly advancing field of nanomaterial characterization.

Keywords: photocacoustics; terahertz; photoacoustic imaging; nanomaterials.

RESUMO

Atualmente, os avanços tecnológicos exigem dispositivos menores, mais rápidos e mais eficientes. Isso torna os nanomateriais essenciais, pois oferecem soluções inovadoras ao melhorar o desempenho em escala nanométrica e impulsionar o desenvolvimento de novos materiais. Suas aplicações abrangem diversas áreas, desde transistores de próxima geração e eletrônicos flexíveis até células solares de alta eficiência e sistemas avançados de entrega de fármacos. No entanto, um dos principais desafios ao trabalhar com nanomateriais é a sua caracterização, que requer técnicas sem contato e não destrutivas. As propriedades eletrônicas, estruturais e ópticas desses materiais são fundamentais para o futuro da ciência dos materiais. Dividida em cinco capítulos, esta tese apresenta os resultados obtidos a partir de duas técnicas poderosas utilizadas para caracterizar diferentes tipos de materiais 2D: fotoacústica (PA) e espectroscopia no terahertz (THz). Ambos os métodos são amplamente utilizados para imageamento e análise de materiais. Após uma breve introdução no Capítulo 1, o Capítulo 2 apresenta uma explicação breve sobre absorção e refração como um lembrete conceitual. O Capítulo 3 é dedicado à fotoacústica, explicando os fenômenos envolvidos, suas equações e aplicações. A microscopia fotoacústica (PAM) é introduzida, e os resultados obtidos em laboratório com essa técnica são apresentados para quatro tipos diferentes de nanopartículas: nitreto de titânio (TiN), nanopartículas de ouro (nanocristais esféricos e nanobastões), nanopartículas co-dopadas com érbio-itérbio (Er^{3+}-Yb^{3+}) e um nanocompósito de óxido de ferro (Fe_3O_4@βCD-PHY). Todas as imagens obtidas com a PAM apresentaram excelente resolução e contraste. Além disso, o fato de que todas as amostras possuem propriedades ópticas e eletrônicas distintas confirma a utilidade da microscopia fotoacústica. O Capítulo 4 explora experimentos no terahertz, como a Espectroscopia no Domínio do Tempo no Terahertz (THz-TDS). A teoria para geração e detecção da radiação THz é apresentada, assim como suas aplicações dentro dessa faixa de frequência do espectro eletromagnético. São discutidos os resultados da caracterização de dicalcogenetos de metais de transição (TMDs) bidimensionais e o design de um filtro contínuo sintonizável para sistemas de telecomunicação em THz. O Capítulo 5 apresenta os trabalhos futuros que serão desenvolvidos para os experimentos em THz. Por meio destes capítulos, este trabalho busca contribuir para o crescente campo da caracterização de nanomateriais.

Palavras-Chave: fotoacústica; terahertz; imageamento fotoacústico; nanomateriais.

FIGURES LIST

ABREVIATION LIST

TMD	Transition Metal Dichalcogenide
NPs	Nanoparticles
MNPs	Metal nanoparticles
THz	Terahertz
PA	Photoacoustic
1PA	One photon absorption
TPA	Two photon absorption
PAM	Photoacoustic microscopy
PAS	Photoacoustic spectroscopy
PAI	Photoacoustic imaging
OCT	Optical coherence tomography
TiN	Titanium nitride
Er^{3+}	Erbium ion
Yb^{3+}	Ytterbium ion
Fe_3O_4	Iron oxide
OPO	Optical parametric oscillator
Nd	Neodimium
YAG	Ytttrium aluminum garnet
DoF	Depth of focus
SPR	Surface plasmon ressonance
Au	Gold
NRs	Nanorods
NSs	Nanospheres
RED	Rare-earth-doped
β-CD	β-cyclodextrin
NIR	Near-infrared
PHY	Phyllancanthone
TDS	Time domain spectroscopy

FIR	Far-infrared
PCA	Photoconductive antenna
DFG	Difference Frequency mixing
OR	Optical rectification
EOS	Electro-optic sampling
$LiTaO_3$	Lithium tantalate
$LiNbO_3$	Lithium niobate
ZnTe	Zinc telluride
OPTP	Optical pump – terahertz probe
TRTS	Time resolved terahertz spectroscopy
MoS_2	Molybdenum disulfide
VO_2	Vanadium dioxide
$ZrTe_2$	Zirconium ditellurite
$NbSe_2$	Niobium diselenide
FFT	Fast Fourier Transform
SEM	Scanning Electron Microscopy
CW	Continuos wavelength
HR	High resistivity

SYMBOL LIST

E	Energy
h	Planck's constant
ν	Frequency
ΔE	Energy difference
a	Absorption
I	Intensity of light
a_0	Linear absorption coefficient
b	Nonlinear absorption coefficient
μ	Magnetic susceptibility
ϵ	Electric permittivity
$\vec{E}$	Electric field
$\vec{B}$	Magnetic field
ω	Angular frequency
k	Wavenumber
t	Time
c	Light speed
$\tilde{n}$	Complex refractive index
n	Real part of the complex refractive index
κ	Imaginary part of the complex refractive index
$\hat{n}$	Unit vector
$\vec{k}$	Wavevector
τ_{th}	Thermal confinement time
τ_s	Pressure confinement time
d	Spatial resolution
v	Sound speed
α_{th}	Thermal diffusivity
E_a	Energy density
Γ	Gruneisen parameter

ρ	Density
T	Temperature
H	Thermal energy
$\sigma^{(2)}$	Two photon absorption cross section
C	Concentration
r	Radius
P^{NL}	Nonlinear polarization
ϵ_0	Vacuum permittivity
$\chi^{(2)}$	Second order nonlinear susceptibility
$\Delta\tau$	Temporal width of the pulse
$\Delta\omega$	Bandwidth
Z_0	Free space impedance

CONTENTS

1 INTRODUCTION

In recent years, two-dimensional (2D) materials and nanomaterials have gained significant attention due to their physical, chemical, and mechanical properties, such as mechanical flexibility, tunable electronic behavior, high optical transparency, and low-temperature solution processability, all of which are of great interest for electronic and optical devices [1]. These materials — including graphene, transition metal dichalcogenides (TMDs), MXenes, and metal nanoparticles (MNPs) — possess unique characteristics such as high electrical conductivity, mechanical strength, and tunable optical properties, making them ideal for applications in electronics, energy storage, optoelectronics, electrocatalysis, and medicine. Their applications range from next-generation transistors and flexible electronics to high-efficiency solar cells and drug delivery systems [2,3]. In today's context of rapid technological advancement, there is a growing demand for smaller, faster, and more efficient devices, which makes nanomaterials a fundamental tool by providing innovative solutions and enhancing performance at the nanoscale.

However, one of the major challenges lies in the characterization of these materials, which requires contactless and non-destructive techniques. Transmission and Scanning Electron Microscopy (TEM and SEM), X-ray Diffraction (XRD), Polarized Optical Microscopy (POM), Atomic Force Microscopy (AFM), and X-ray Photoelectron Spectroscopy (XPS) are standard characterization techniques that can provide information about the morphology, structure, particle size, and surface area of the material. Techniques such as UV–Vis spectroscopy, Diffuse Reflectance Spectroscopy (DRS), and photoluminescence (PL) are useful for analyzing the optical properties of 2D materials, including absorption, reflection, and phosphorescence [4,5]. The need for large-scale equipment to perform such measurements, combined with the destructive and ionizing nature of some techniques, underscores the importance of developing alternative methods for characterization.

Photoacoustic and terahertz (THz) techniques can play a crucial role in the characterization of two-dimensional (2D) materials due to their non-destructive and non-ionizing nature, as well as their ability to provide valuable insight into structural, electronic, and optical properties [6]. Photoacoustics enables the analysis of thermal and mechanical characteristics by detecting acoustic waves generated through light absorption, making it particularly useful for evaluating defects and performing imaging of 2D materials [7]. On the other hand, terahertz spectroscopy,

owing to its sensitivity to low-energy excitations, allows the investigation of carrier dynamics, conductivity, and dielectric properties. It is especially effective for studying interlayer interactions, phonon modes, and electronic transitions [8]. By combining these two techniques, a more comprehensive understanding of 2D materials can be achieved, fostering advancements in optoelectronics, nanophotonics, and quantum technologies. Their non-invasive nature and ability to probe fundamental material properties make them indispensable tools in the development of next-generation devices.

Imaging techniques are another important approach for material characterization, commonly used for morphological studies and, in the biomedical field, for a wide range of diagnostic purposes [9]. Today, some of the most widely used techniques include magnetic resonance imaging (MRI), computed tomography (CT), positron emission tomography (PET), ultrasound, and optical coherence tomography (OCT). However, the applicability of each technique is limited, as all of them present certain drawbacks [10].

Magnetic resonance imaging, in addition to being very expensive, requires a long acquisition time. CT and PET scans involve the use of ionizing radiation, which carries a potential risk of inducing cancer [11] and, therefore, should not be used too frequently [12]. Despite these concerns, their use remains widespread due to the implementation of strict safety protocols.

Photoacoustic and terahertz imaging techniques are widely employed due to their non-ionizing and non-destructive nature. Photoacoustic microscopy (PAM) has been extensively applied in biomedical contexts and can be further enhanced through the use of contrast agents. By combining optical contrast with acoustic resolution, PAM is a powerful technique capable of studying the morphology of microscale materials [13]. Meanwhile, terahertz (THz) imaging systems leverage their non-destructive nature for applications in biomedical diagnostics and security screening [14]. In the past, the practical use of this technique was limited by the raster-scanning requirement, which resulted in very low imaging speeds. However, significant progress has been made in recent years, including the achievement of micrometer-scale resolution [15], reduced imaging time, and the development of single-shot ultrafast terahertz photography [16]. Thus, photoacoustic and terahertz techniques offer a broad range of possibilities and pave the way for new studies on emerging materials.

2 LIGHT-MATTER INTERACTION

This chapter provides the fundamental background for the thesis, focusing on two key phenomena: absorption, which is essential for understanding the photoacoustic effect, and refraction, extremely important for terahertz (THz) measurements. But before explaining about these topics, however, it is important to introduce the light sources that can induce these phenomena.

2.1 LIGHT SOURCES AND LASERS

Studying the properties of a given material is a complex task. One effective approach involves analyzing its interaction with light. Among various light sources, discharge lamps deserve special mention, as they were widely used in optical measurements prior to the invention of lasers [17]. These lamps operate by passing an electric current through a tube containing a gas or a mixture of gases. There are noble gas lamps (such as xenon and helium), as well as lamps containing other elements, such as hydrogen and mercury.

The first maser (Microwave Amplification by Stimulated Emission of Radiation) was built in 1955 by Gordon, Zeiger, and Townes, who demonstrated that it was possible to amplify a microwave signal using ammonia molecules [18]. They showed that this could be achieved with a population inversion in the ammonia molecules (meaning that most of the molecules were in an excited state rather than in the ground state) and if they were confined within a cavity. Three years later, Townes and Schawlow detailed the functioning of the maser and proposed that this effect could be extended to the visible and infrared spectrum [19], leading to the first laser (Light Amplification by Stimulated Emission of Radiation), built in 1960 by Maiman, which operates at 694 nm [20]. One crucial requirement for a laser is a pumping energy source to enable population inversion in the active medium (or gain medium), which happens when most of the atoms are in an excited state. This pump can come from flashlamps, electric current, gas discharge, or even another laser. These atoms can then return to the ground state through a process known as stimulated emission.

Stimulated emission is a process in which an atom in an excited state interacts resonantly with a photon. This means that the energy of the incident photon matches the energy difference between the atom's excited and ground states. When this happens, the previously excited atom

transitions to a lower energy state, emitting a photon with the same properties (frequency, phase, and polarization) as the incident one. Figure (2.1) illustrates the stimulated emission process.

Figure 2.1: Stimulated emission diagram.

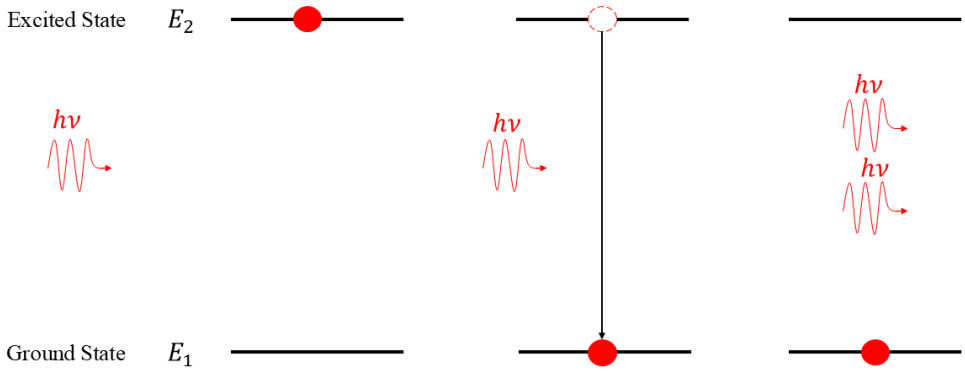

Source: The author (2025)

In the diagram represented in Figure (2.1), a photon with energy $h\nu$ interacts with an atom in the active medium (represented by the red circle), which is already in an excited state due to the pump energy. Notice that the energy difference between the excited state (E_2) and the ground state (E_1) is equal to the energy of the incident photon ($E_2 - E_1 = h\nu$). When this interaction occurs, the atom returns to the ground state, and during this process, it emits a photon with energy $h\nu$, as represented in the final scheme. Since the incident photon was not absorbed at any point, the result of this phenomenon is an atom in the ground state and two emitted photons.

When the gain medium, in which the stimulated emission occurs, is placed inside an optical cavity — consisting of a set of properly aligned mirrors — it allows the photons to interact with the active medium multiple times, acting as a feedback system and enabling more photons to interact with the molecules of the active medium, thereby amplifying the number of photons produced by stimulated emission. To allow part of the beam to exit the optical cavity, one of the mirrors must be partially reflective (< 100% reflectivity). This enables the transmission of photons in a direction defined by the cavity axis. The result is a monochromatic, collimated, and coherent beam — unique characteristics of a laser, illustrated in Figure (2.2).

Figure 2.2: Diagram showing a laser cavity.

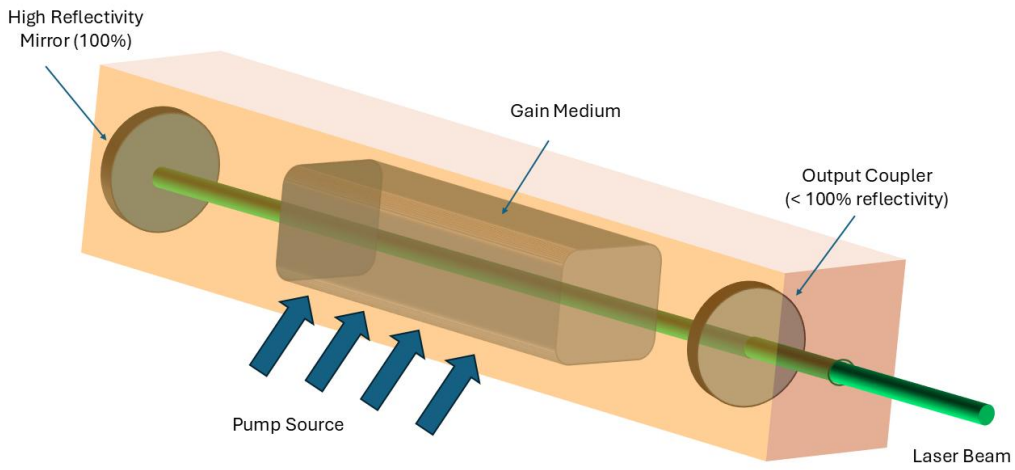

Source: The author (2025)

2.2 ABSORPTION

Light absorption by a medium occurs if the optical frequency is resonant with the resonance frequency of the atoms in the medium. The energy difference between the excited state and the ground state of the atoms (denoted as ΔE) must be equal to the energy of the photon emitted by the light source, which is calculated using the product of Planck's constant (h) and the frequency of the light beam, i.e.:

$$E = h\nu \quad . \tag{2.1}$$

If $\Delta E = E$ and only one photon is absorbed, an electron is ejected into an excited state. This phenomenon is known as photon absorption (1PA).

The invention of lasers made it possible to study processes that depend on a very intense monochromatic source [25], leading to the development of nonlinear optics [26]. It was the advancements in nonlinear optics that led to a more general description of the absorption coefficient, a parameter that characterizes material absorption, as given by [20]:

$$a = a_0 + bI \quad . \tag{2.2}$$

where I represents the beam intensity, while a_0 and b are the linear and nonlinear absorption coefficients, respectively. This shows that there is a dependence on beam intensity for nonlinear materials. For very low intensities, even nonlinear materials will exhibit a linear absorption behavior, but as the intensity of the light incident on the sample increases, nonlinear effects begin to appear. Therefore, the development of the laser was crucial for observing nonlinear phenomena due to its high power. As a result, it became possible to observe the phenomenon of two-photon absorption (TPA) [21]. This phenomenon was theorized in 1930 [22] and describes the possibility of an electronic transition from a lower energy state to a higher energy state through the absorption of two photons, given that the beam intensity is sufficiently high.

As a specific energy per photon (ΔE) is required for absorption to occur, it is strictly necessary that the sum of energies of each photon be equal to the energy difference between the excited and ground states. This doesn't mean that the two photons must be identical, but rather that there is a condition on the sum of the frequencies, which must be precisely defined, so that the sum of the energy of each photon equals the difference between the excited and ground states. Moreover, because it is a nonlinear phenomenon, there is a direct dependence on the beam intensity, as previously mentioned.

2.3 REFRACTION

Refraction is a phenomenon in which a wave passes from one medium to another (with two different refractive indices, as shown later), changing its properties — such as velocity and phase — while maintaining its frequency. It is already known that light is an electromagnetic wave and, therefore, is susceptible to this phenomenon. Starting from Maxwell's equations, one can obtain the Helmholtz wave equation, expressed as:

$$(\nabla^2 - \mu\epsilon\omega^2)\begin{pmatrix}\vec{E}\\ \vec{B}\end{pmatrix} = 0 \quad . \tag{2.3}$$

One possible solution for this equation is proportional to $e^{i(kx-\omega t)}$, considering the electromagnetic wave traveling along the x direction. The quantity "k" is called wavenumber. To satisfy this, we need that:

$$k = \frac{2\pi}{\lambda} = \sqrt{\mu\epsilon}\omega \quad , \tag{2.4}$$

and the phase velocity (v) is:

$$v = \frac{\omega}{k} = \frac{1}{\sqrt{\mu\epsilon}} = \frac{c}{n} \quad . \tag{2.5}$$

The quantity called "n" is of great interest for physical systems. It's called refractive index, and it's usually a complex function:

$$\tilde{n}(\omega) = n + i\kappa \quad . \tag{2.6}$$

From now on, the complex refractive index will be denoted by $\tilde{n}$ while the real part of it will be just n. The real part of the complex refractive index is due to phase shifts, while the imaginary part is related to the absorption of the medium. Understanding how the refractive index plays an important role in physics systems is very important, especially regarding the behavior of an electromagnetic wave is after changing the medium of propagation. To understand this, it's necessary to solve the following boundary conditions [23]:

$$\begin{aligned}
&\left[\epsilon\left(\vec{E}_0 + \vec{E}_o''\right) - \epsilon'\vec{E}_0'\right] \cdot \hat{n} = 0 \\
&\left[\vec{k} \times \vec{E}_0 + \vec{k}'' \times \vec{E}_0'' - \vec{k}' \times \vec{E}_0'\right] \cdot \hat{n} = 0 \\
&\left(\vec{E}_0 + \vec{E}_0'' - \vec{E}_0'\right) \times \hat{n} = 0 \\
&\left[\frac{1}{\mu}(\vec{k} \times \vec{E}_0 + \vec{k}'' \times \vec{E}_0'') - \frac{1}{\mu'}(\vec{k}' \times \vec{E}_0')\right] \times \hat{n} = 0 \quad .
\end{aligned} \tag{2.7}$$

It's possible to have the electric field parallel or perpendicular to the plane of incidence. Therefore, we may have two different equations, one for each case, as represented in Figure (2.3).

Figure 2.3: Refracted waves on an interface with different refractive index. Electric field (a) parallel and (b) perpendicular to the plane of incidence.

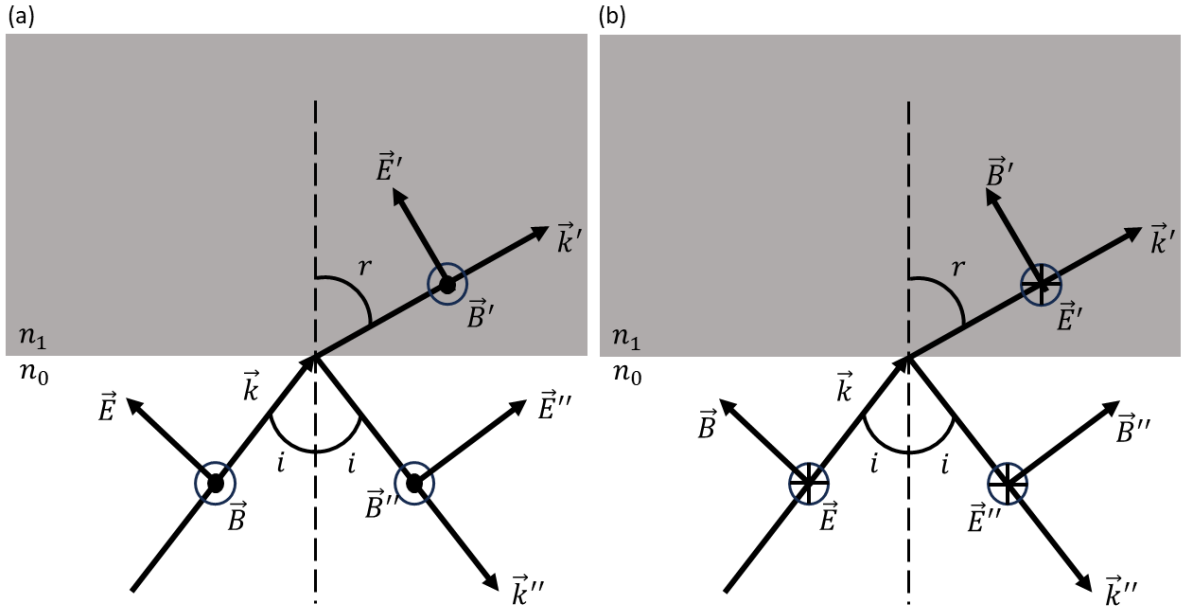

One can solve these equations considering that the interface is at at $x = 0$ (to eliminate the exponentials) and for normal incidence ($i = 0$), the transmitted and reflected electric field are:

$$\frac{E_0'}{E_0} = \frac{2\tilde{n}_0}{\tilde{n}_0 + \tilde{n}_1} \quad , \quad \frac{E_0''}{E_0} = \frac{\tilde{n}_1 - \tilde{n}_0}{\tilde{n}_1 + \tilde{n}_0} \quad . \tag{2.8}$$

It's very important to state that the boundary conditions represented in Equation (2.7) must be solved for every interface where refraction occurs. As will be presented in Chapter 4, this treatment is crucial for terahertz (THz) measurements.

3 PHOTOACOUSTICS

In this chapter, the photoacoustic effect will be presented, as well as one imaging technique called “Photoacoustic Microscopy” (PAM). First, the theoretical background and an explanation of the phenomena will be discussed. Subsequently, the PAM technique is explained, highlighting some useful applications. Finally, four results for different nanoparticles will be presented using this technique.

3.1 THEORY

The first report about photoacoustics was in 1880, when Alexander Bell observed that it was possible to hear a sound coming from solid materials, such as selenium, gold, silver, and platinum, when pulsed light was impinging on the material [24], proposing that it was a fundamental property of matter. One year later, Tyndall [25] and Röntgen [26] observed this phenomenon in gases and started calling it the photoacoustic effect (or optoacoustic effect).

This phenomenon was completely forgotten for a long time because measuring it was extremely challenging due to the fact that the detection system relied on human hearing, making accurate measurements very difficult. It was only with advancements in microphone technology and the development of new light sources that photoacoustic experiments were resumed [27].

In 1976, Rosencwaig and Gersho proposed that thermal diffusion played a role in the generation of the photoacoustic effect, demonstrating that the periodic absorption of light (due to modulated-intensity light) generates a periodic heat flow in a thin layer at the interface between the sample and the surrounding medium. This process induces an oscillatory motion that propagates as an acoustic wave, representing the first theoretical explanation for the photoacoustic effect [28]. Thus, the photoacoustic effect is generated when a modulated-intensity light beam is absorbed by a material, leading to a localized temperature rise. This increase in temperature generates a variation in local pressure, which propagates as an acoustic wave. This wave is then detected by a transducer or microphone, which converts the mechanical signal from the acoustic wave into an electrical signal. This electrical signal is subsequently analyzed by an acquisition device.

However, it is not just any modulated-intensity light that generates the photoacoustic effect. One important feature is that the excitation of the light ends before the heat diffuses through

the medium and before the generated acoustic wave propagates out of the illuminated region. This occurs when two characteristics are considered: the thermal confinement time (τ_{th}) and the pressure confinement time (τ_s), which are given by:

$$\tau_{th} = \frac{d^2}{\alpha_{th}} \qquad \tau_s = \frac{d}{v} \quad , \tag{3.1}$$

where d is the spatial resolution, v is the sound speed in the medium and α_{th} is the thermal diffusivity of the medium. In the situation where the laser pulse width (τ) is smaller than these two characteristics time, the pressure increases as:

$$\mathrm{P_0}(\vec{r}) = \frac{\beta}{\kappa_\mathrm{T}\rho\mathrm{C_V}}\mathrm{E_a} = \Gamma\mathrm{E_a}(\vec{r})\,. \tag{3.2}$$

In Equation (2.16), Γ is the Grüneisen parameter and E_a is the energy density of the beam. It is possible to observe that the variation in local pressure, responsible for generating the photoacoustic wave, is only proportional to the material's absorption. Therefore, effects such as scattering, diffraction, and refraction, which influence optical measurements, do not interfere with the photoacoustic signal. However, this variation in pressure that gives rise to the photoacoustic effect must occur in a pulsed manner. To show this condition, starting with the continuity equation for a mass flow:

$$\frac{\partial\rho(\vec{r},t)}{\partial t} + \nabla\cdot(\rho(\vec{r},t)\vec{u}) = 0 \quad . \tag{3.3}$$

It's possible to derive a wave equation for an infinitesimal variation in pressure p that has the term on the right-hand side as a source, depending on the thermal energy $H(t)$:

$$\left(\nabla^2 - \frac{1}{v^2}\frac{\partial^2}{\partial t^2}\right)p = \frac{1}{TC_P}\frac{\partial H}{\partial t} \quad , \tag{3.4}$$

where *v*, *T*, and *C_p* are the sound speed in the medium, temperature, and heat capacity at constant pressure, respectively. The formalism for deriving these equations is provided in [29]. This equation shows that a time-dependent heat energy flow is fundamental to generating the photoacoustic effect. Therefore, only a modulated-intensity beam, such as pulsed lasers, can generate the photoacoustic effect [30], illustrated in Figure (3.1):

Figure 3.1: Schematization of the photoacoustic effect

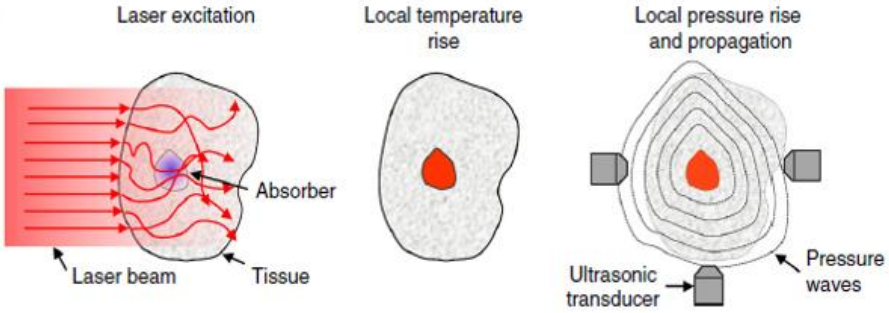

Source: [31]

Accurate measurement of the photoacoustic effect was a major challenge. The first measurements were made using microphones [32,33] and piezoelectric crystals [34,35], which measure the electric field generated by the pressure created from the photoacoustic wave, and can be detected as a voltage. Additionally, ultrasonic transducers [36] are extensively used nowadays, some of which are immersion types, allowing them to be placed in water for better acoustic coupling [37].

Since photoacoustics is a phenomenon that depends solely on the material's absorption, it is highly useful as a spectroscopic technique. Spectroscopy is the study of the interaction between radiation and matter. In most optical spectroscopic techniques, the properties of materials are studied through their interaction with electromagnetic radiation in the optical domain. The materials' properties are determined based on the photons either transmitted through the sample or scattered and reflected [38]. In both methods, obtaining an absorption spectrum is not straightforward and requires relating the light signal before and after it reaches the sample. Although these methods are valuable tools that have been used for centuries, they present certain limitations depending on the type of sample [27]. Since the absorption spectrum is obtained by comparing the emitted and transmitted signals, materials with low absorption make it difficult to extract meaningful data because there will be minimal signal differences

between the beam before and after interacting with the sample. Additionally, samples like powders, amorphous solids, and biological tissues have high scattering properties, which significantly interfere with optical absorption measurements. For opaque materials, where the signal is a combination of specular reflection, diffusivity, and transmission, analyzing the results becomes highly complex [38].

Photoacoustic spectroscopy (PAS), developed in the 1970s, helps to overcome the challenges associated with conventional techniques because it uses the photoacoustic effect to analyze the sample's absorption [38] In this technique, a pulsed light beam strikes the material being studied, generating photoacoustic waves, which are detected by a sensor. Since the emitted signal is directly proportional to absorption, as mentioned before, it is possible to analyze the material's absorption across different wavelengths, thereby generating an absorption spectrum by recording the photoacoustic signal of the sample at each specific wavelength. However, to remove any unwanted contributions from the system, it is necessary to normalize the signal by taking the ratio of the measured signal to a reference. This procedure is often done by using a highly absorbing material, such as carbon powder, with the same light source and power [38]. This technique has proven highly valuable due to its practical applications, such as simulating studies on atmospheric pollution, determining gas concentrations [33], as well as biomedical applications, where spectra of proteins, hemoglobin [38], chemical changes in ocular structures [39] and properties of tissues [40] have already been studied.

Photoacoustics can also be used for imaging techniques, especially for biomedical purposes. Although conventional optical imaging techniques provide images with excellent contrast, they suffer significant losses in resolution and sensitivity due to effects such as scattering [9], leading to low penetration, of approximately 3 cm [41]. Scattering of light by biological tissue is at least one hundred times greater than the scattering of sound waves [42]. On the other hand, the sound scattered by biological tissues is one hundred times lower than the scattering of light, allowing greater penetration (approximately 6 cm) [43]. Although they offer better resolution and sensitivity due to the much lower acoustic scattering, the contrast is much lower, making them unable to provide important information such as chemical composition, absorption, metabolism, and physiological changes [44]. The ideal solution for effective imaging would be to combine the contrast provided by purely optical techniques with the resolution and sensitivity of ultrasound, which can be achieved through the photoacoustic effect [41,45], leading to what is called Photoacoustic Microscopy (PAM).

3.2 PHOTOACOUSTIC MICROSCOPY (PAM)

The study of the morphology of samples on a microscopic scale through the photoacoustic effect became a valuable area of research due to the high sensitivity and non-destructive nature of the technique [46]. To reproduce the image of the surface of the studied material [47], photoacoustic microscopy (PAM) emerged, leading to the development of photoacoustic imaging (PAI) techniques. The direct dependence between the photoacoustic signal and the material's absorption means that the dimensions of the beam incident on the sample determine the size of the region from which the material's information will be obtained, as shown in Equation (2.14), which demonstrates a local dependence regarding the generated signal [48]. Thus, by using a light beam with micrometric dimensions, the absorption of light will occur through a region of the sample with these dimensions, allowing for more detailed material characterization—this is the principle behind photoacoustic microscopy (PAM).

The micrometric beam size for photoacoustic imaging was introduced by von Gutfeld and Melcher [49] to examine material defects. The decrease in beam diameter was achieved through an objective lens to focus it, and the sample was placed near the focus. The first application of this system was to detect defects on the material's surface by shining the beam on different spots of the sample, performing a scanning process. For each illuminated region, a photoacoustic signal is generated and compared with the signals from other regions—a process that was initially performed manually [49]. The differences in the signals from each region, either in amplitude or in the time taken by the photoacoustic wave to reach the detector, served as an indication of a defect in the material.

Figure (3.2) presents a sketch of how it is possible to distinguish and map a material's surface. Two different spots generating the photoacoustic signal will have different times and amplitudes when compared to each other. For example, in the graph presented in Figure (3.2), the time (t_0) is the trigger and represents the moment the optical beam reaches the sample. In this situation, two different places are considered: the green and red spots. The green spot is closer to the transducer and, therefore, the photoacoustic wave will reach the transducer in a shorter time (t_1) when compared to the red spot (t_2). Furthermore, since the distance is shorter, the attenuation will also be smaller, and the amplitude of the signal will be higher. So, by measuring the distance between the transducer and the sample on the timescale from an oscilloscope, it is possible to detect flaws in the material's surface. Of course, for materials with

regions of different absorption, the amplitude of the photoacoustic signal will change according to the material's absorption, as mentioned before.

Figure 3.2: Photoacoustic measurement and signal relation to the point of the photoacoustic source.

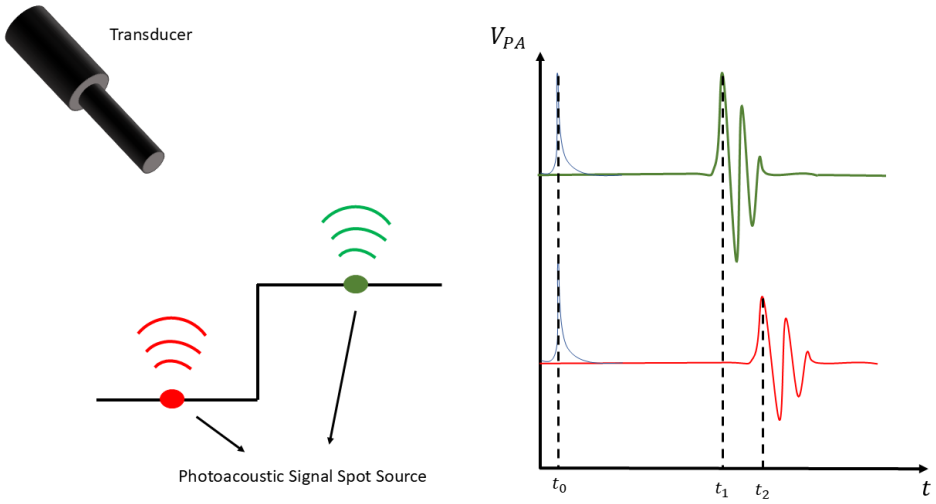

Source: The author (2025)

In addition to detecting faults on the surface of the samples, it was shown that, depending on the wavelength of the incident light, it was possible to reach deeper regions of the material and obtain subsurface information [47]. The change in the amplitude and phase of the signal allowed for the differentiation of defects from other components that might be present in the sample, based on the absorption coefficient. Therefore, photoacoustic microscopy is capable of characterizing the surface and subsurface of samples in a non-destructive manner [47].

This feature sparked the interest of many researchers, who began to conduct PAM experiments and improve the method, eventually reaching depths of hundreds of micrometers [46,47,50–52]. Due to these characteristics, it wasn't long before applications in the biomedical field were suggested, and the first photoacoustic imaging was performed in 1979, in which a hexagonal pattern on a chromium sample and aluminum foil was detected using a Nd:YAG laser emitting at 1064 nm [53]. This result is shown in Figure (3.3).

Figure 3.3: First photoacoustic microscopy measurement compared to others optical standard techniques (a) transmission, (b) reflection and (c) photoacoustic

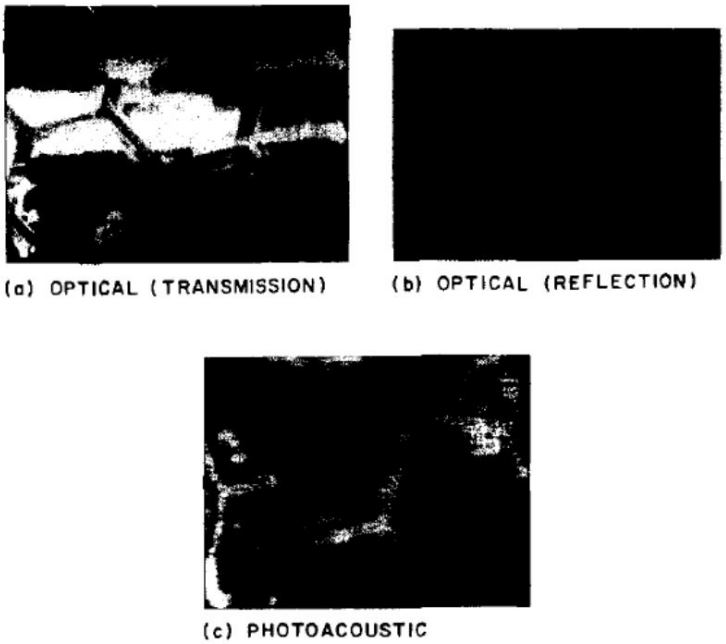

Source: [53]

Enlightened by this result, the proposal of a new imaging technique called Photoacoustic Microscopy emerged in 1979 [54], where it was demonstrated that this technique was more compatible than the ultrasonic microscopy technique used at the time. The applications of photoacoustic microscopy in biomedicine are varied. The first studies were conducted to determine peroxidase activity in biological tissue [54] and to identify biological components present in tissues [43]. The technique was further refined to the point where it could determine oxygen saturation in blood [55], as well as angiography, histography, and dermatology applications [7].

Another important feature of any imaging technique is the system's resolution. In Photoacoustic Imaging, the lateral resolution of the system is mainly limited by the ultrasonic transducer's central frequency. The lateral resolution can be estimated by the following equation [7]:

$$LR_{PA} = 0.71\frac{v}{f_c \cdot NA_s} \quad . \tag{3.5}$$

In Equation (3.5), v is the speed of sound in a medium, f_c is the ultrasonic transducer's central frequency and NA is the acoustic numerical aperture. Therefore, the lateral resolution can be improved by increasing the central frequency of the ultrasonic transducer. The increased center frequency also results in increased acoustic attenuation, limiting the imaging depth. Therefore, when designing a PAM system, it is very important to carefully consider the trade-off between imaging depth and lateral resolution [7]. As an example, with a center frequency of 50 MHz and an NA of 0.44, 45-μm lateral resolution and 3-mm imaging depth have been achieved. Such a system is adequate to see through human skin lesions *in vivo*, as required for accurate diagnosis and staging. Reducing the center frequency to 5 MHz extends the imaging depth to 4 cm and relaxes the lateral resolution to 560 μm [13].

Imaging techniques that exploit the photoacoustic effect present certain advantages when compared to conventional techniques, such as ultrasound and optical coherence tomography (OCT), due to their non-destructive nature, high contrast, and good spatial resolution — especially in biological tissues, where the scattering of the electromagnetic wave is approximately one hundred times greater than that of the acoustic wave, allowing better resolution for PAM.

3.3 RESULTS IN PHOTOACOUSTICS

In this section, the results on photoacoustic microscopy will be presented. The experimental setup is represented in Figure (3.4). A nanosecond laser with a repetition rate of 10 Hz and a pulse width of 7 ns was used as the light source for different kinds of samples, as will be presented. The samples were placed in a plastic container filled with distilled water for better acoustic coupling. The container was placed on two motorized stages (THORLABS MTS50-Z8) positioned perpendicular to each other, allowing the sample to be moved for a 2D scan.

Figure 3.4: Photoacoustic Microscopy setup. M, mirror; PD, photodetector; OSC, oscilloscope, ST, stage; L, lens; T, transducer.

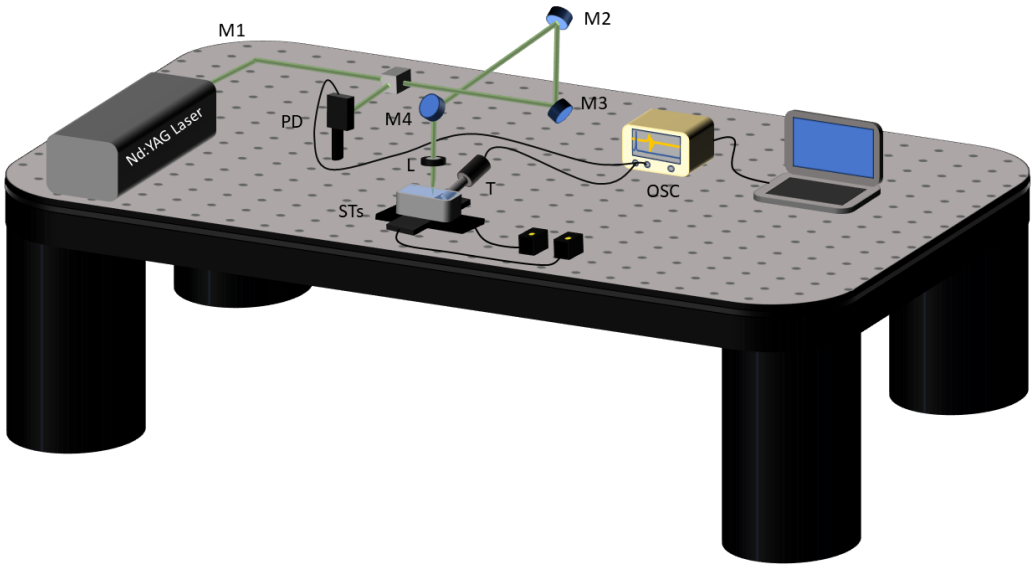

Source: The author (2025)

The photoacoustic wave is detected by an ultrasonic transducer (OLYMPUS V312-N-SU) with a central frequency of 10 MHz. The signal is then amplified (MINI-CIRCUITS ZFL-500-LN-BNC) and digitized by a two-channel oscilloscope (TEKTRONIX 3032B), connected to a computer running LABView software with a homemade acquisition program for PAM. A 100 mm focal length lens is used to achieve micrometer resolution (around 70 µm). Figure (3.5) illustrates the focused beam and the transducer detecting the photoacoustic wave. The inset (Figure 3.5b) shows the oscilloscope signal. The blue plot is the trigger from the photodetector (reference), and the yellow curve is the photoacoustic signal. The delay between the blue peak and the photoacoustic one corresponds exactly to the time interval for the acoustic wave to travel from the sample to the transducer.

Figure 3.5: Scheme representing the photoacoustic detection. (a) the focusing beam onto the sample and detected by the transducer and (b) the digitalized signal from the oscilloscope.

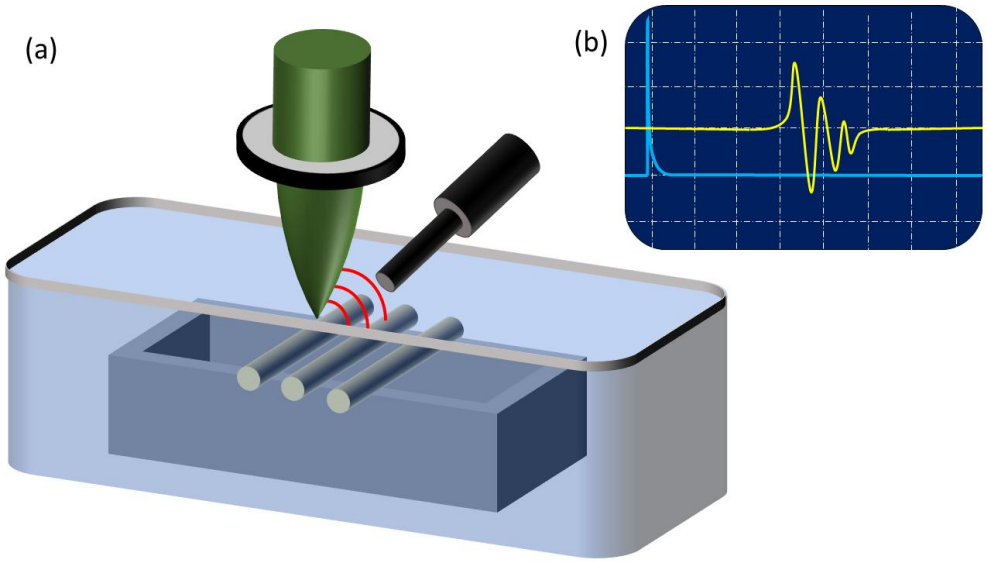

Source: The author (2025)

The samples were placed in an acrylic holder with a hole in the middle to increase the distance from the sample to the bottom of the container. By doing this, if there is any contribution to the photoacoustic effect from the container, it would be shifted, making it possible to separate both signals. The samples studied using this system were: titanium nitride (TiN), gold nanoparticles (nanospheres and nanorods), erbium-ytterbium (Er^{3+}-Yb^{3+}) codoped nanoparticles and an iron oxide (Fe_3O_4) nanocomposite (Fe_3O_4@βCD-PHY). For the first three samples, an optical parametric oscillator (OPO) VIBRANT 355 LD, ranging from 410 nm to 2.4 µm, was used. This OPO allows selecting the desired wavelength for each measurement. Meanwhile, for the last sample (Fe_3O_4@βCD-PHY) a typical Nd:YAG laser was used (Continumm, Surelite II) operating in 1064 nm.

3.3.1 Titanium Nitride (TiN) Nanoparticles

The fact that the emitted photoacoustic wave depends only on the material's absorption, as shown in Equation (3.2), and propagates as a sound wave, allows the photoacoustic effect to be used in various applications that require knowledge of the material's absorption. One interesting and simple application is the study of two-photon absorption (TPA) [9]. The number of photons absorbed by a material per unit of time can be expressed as [21]:

$$N_{abs} = \int_V \sigma^{(2)} C(\vec{r},t) E^2(\vec{r},t) dV \quad , \tag{3.6}$$

where $C(\vec{r},t)$ is the samples' concentration, $\sigma^{(2)}$ the two-photon absorption cross section and $E^2(\vec{r},t)$ is the energy density on the sample. Considering a homogeneous sample and the thickness of the sample bigger than the depth of focus (DoF) of the beam, the number of absorbed photons will be:

$$N_{abs} = S^2 C \sigma^{(2)} E^2(t) \quad . \tag{3.7}$$

In Equation (3.7), *S* is a constant depending on the wavelength, refractive index and the numerical aperture of the lens, only spatial parameters. Since the photoacoustic signal depends solely on the absorption, and therefore the number of absorbed photons:

$$PA \propto E^2 \quad . \tag{3.8}$$

This means that $\ln(PA) \propto 2\ln(E)$. Therefore, the slope of a plot of the logarithm of the photoacoustic signal versus the logarithm of energy density will provide the number of photons absorbed.

This work [56] deals with the TiN nanoparticles synthesized using the laser ablation technique, a process in which material is removed from a solid surface by irradiation with a laser beam. For this set of nanoparticles, a Yb:KGW femtosecond laser (TETA 10, AVESTA, Moscow, Russia) was used, with a wavelength of 1030 nm, a repetition rate of 10 kHz, and a pulse duration of 270 fs [57]. The bulk TiN sample (GoodFellow), with 99.5% purity, was placed vertically in a cuvette with acetone (Sigma Aldrich). The beam passed through a 100 mm focal length lens to reduce its diameter, which was initially approximately 3 mm. This led to the removal of TiN nanoparticles. To avoid material removal from the same spot, a galvanometer scanner was used, allowing for a change in the beam's incidence direction, thereby targeting different regions of the TiN sample. In this process, which lasted around 20 minutes, the pulse energy was 100 µJ, and the final sample concentration was 50 µg/mL [56]. A schematic representation of the nanoparticle synthesis system is shown in Figure (3.6a).

Figure 3.6: (a) Laser ablation method for synthesize TiN nanoparticles and (b) Size distribution of the TiN nanoparticles.

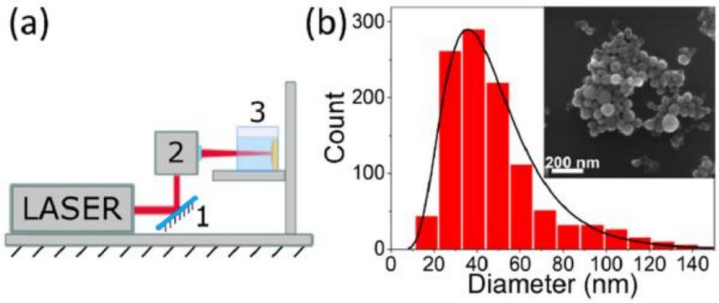

Source: [57]

The chemical and structural characteristics of the nanoparticles were measured using a scanning electron microscope (SEM) (MAIA 3, Tescan), along with an energy-dispersive X-ray spectroscopy system (X-act, Oxford Instruments). The SEM results confirmed the formation of spherical nanoparticles. A statistical analysis established a size distribution for the generated nanoparticles, with a most frequent diameter around 40 nm, as shown in Figure (3.6b).

The first step to perform photoacoustic microscopy is determining the best wavelength for the measurement, which means the one with the highest absorption. Therefore, the absorption spectrum of the nanoparticles synthesized in acetone was measured using a UV-Vis-NIR spectrophotometer (Fluoromax, HORIBA) and is presented in Figure (3.7a). It shows two regions of high absorption: one in the ultraviolet (UV) region due to interband transitions, and another around 725 nm caused by surface plasmon resonance. This can be confirmed through a nonlinearity measurement, as previously mentioned, in which we analyze the amplitude of the photoacoustic signal as a function of the optical fluence incident on the sample. By plotting a log-log graph, from Equation (3.7), one can confirm the nonlinear absorption of any kind of material. For the TiN NPs, this measurement was performed using three different wavelengths (532, 725, and 880 nm). The result, represented in Figure (3.7b), shows that only at 725 nm does two-photon absorption occur, since it is the only wavelength for which the fitting slope is equal to 2, while for 532 nm and 880 nm the slope is close to one, indicating one-photon absorption.

Figure 3.7: (a) Absorption spectra of TiN nanoparticles and (b) Two-photon absorption measurement of TiN nanoparticles for different wavelengths.

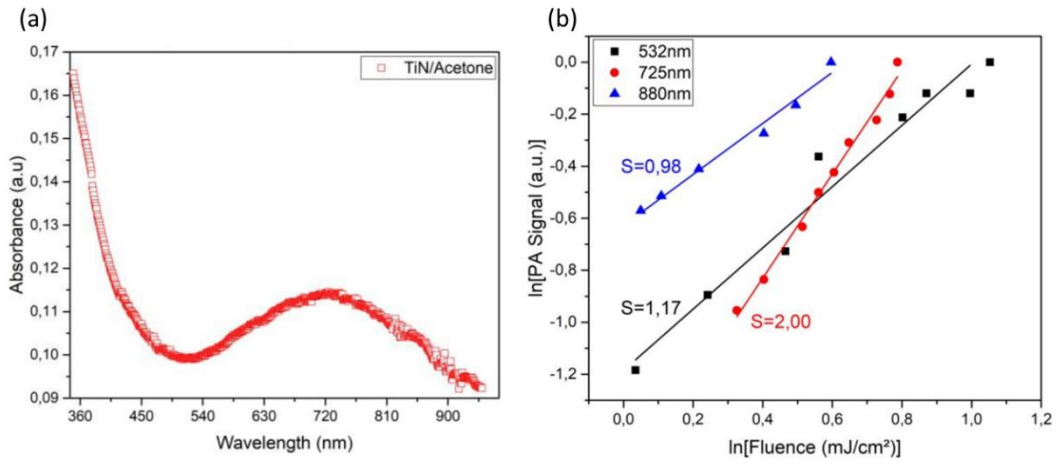

Source: [56]

Photoacoustic microscopy was performed using the system described previously for the same three wavelengths (532, 725, 880 nm) reported in Figure (3.7b) for the nonlinear absorption measurement. The samples were placed in a capillary tube (PRECISION, China) with an internal (external) diameter of 1 mm (1.5 mm). Since the maximum fluence achieved was 1.85 mJ/cm² for the 880 nm wavelength, all the PAM measurements were recorded keeping this energy density constant for all three wavelengths. The results are shown in Figure (3.8). By keeping the power constant for all wavelengths in question, we ensure that the change and increase in the photoacoustic signal is a result of the material's different absorption at different wavelengths. It is verified that the three images show excellent contrast and resolution, as it is even possible to measure the thickness of the tube in which the sample is placed, represented by the vertical dashed line. It is noticeable that the best image is obtained at 725 nm, as expected from the absorption spectra presented in Figure (3.7a), and this is due to the two-photon absorption.

Figure 3.8: Photoacoustic microscopy of the TiN nanoparticles at (a) 532 nm, (b) 725 nm and (c) 880 nm.

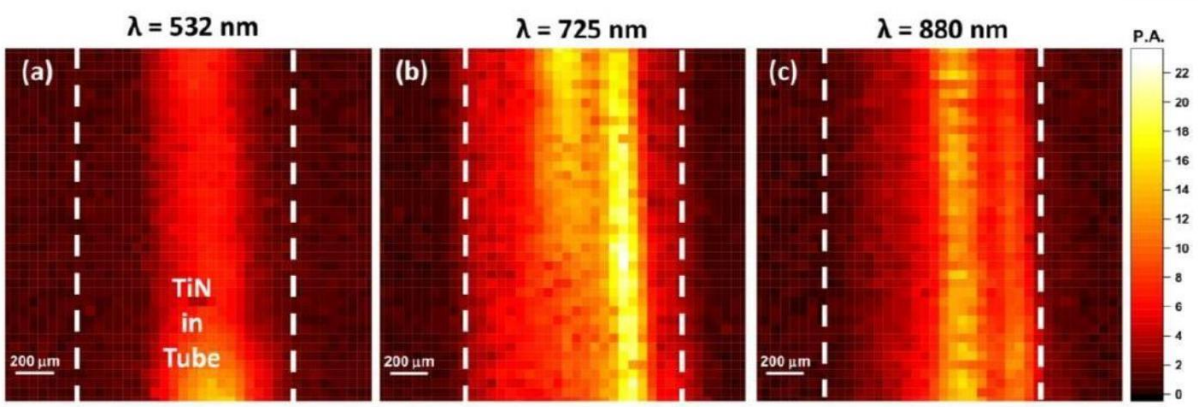

Source: [56]

3.3.2 Gold Nanoparticles

Recently, metallic nanoparticles (such as gold nanoparticles) have been studied as an alternative for tumor detection due to their greater photostability and absorption compared to conventional contrast agents. This absorption peak is typically found within the first biological window (a region where tissues are less absorbent), which is in the near-infrared (NIR) range (700 nm – 1000 nm). This results in images with improved resolution since regions without nanoparticle accumulation generate a much lower signal than those containing them, providing higher image contrast [58]. By tailoring the appropriate shape and dimensions [59], these nanoparticles exhibit a well-defined absorption band due to a phenomenon known as surface plasmon resonance (SPR) [60], which occurs in materials that have free electrons, such as metals. When the incident beam has a wavelength larger than the dimensions of the sample, the free electrons on the material's surface oscillate in sync with the electric field of the incoming light, constantly changing the polarization of the nanoparticles. This electronic oscillation, combined with that of the electric field, enhances the material's absorption and scattering effects [59,61]. The scattering and absorption cross section for a conductive sphere is [23]:

$$\sigma_{sca} = \frac{8}{3}\pi k^4 r^6 \frac{(\epsilon' - \epsilon_m) + \epsilon''^2}{(\epsilon' + 2\epsilon_m)^2 + \epsilon''^2} \quad , \tag{3.9}$$

$$\sigma_{abs} = 4\pi k r^3 \frac{\epsilon_m \epsilon''^2}{(\epsilon' + 2\epsilon_m)^2 + \epsilon''^2} \quad . \tag{3.10}$$

In Equations (3.9) and (3.10), ϵ is the complex permittivity of the NP ($\epsilon = \epsilon' + i\epsilon''$), k is the wavenumber, and r is the radius of the nanosphere. For thermal applications, structures with high absorption are desired, and as shown in Equation (3.10), the shape and size of the nanoparticles play an important role in their absorption. A clever way to tailor and optimize the size and dimensions of the nanoparticles is to use the Joule number as a figure of merit to assess the temperature variation in the nanoparticle [62], as proposed in this work.

The size-dependent absorption can be experimentally demonstrated with photoacoustic microscopy. In this work [63], in collaboration with the Laboratory of Biomedical Optics and Imaging (LOBI) at UFPE, simulations in COMSOL Multiphysics were performed for different dimensions of gold nanospheres (Au NSs) (5, 50, and 100 nm diameter) and nanorods (Au NRs) (41 × 10, 90 × 25, and 134 × 40 nm) to obtain the theoretical value of the Joule number for each nanoparticle. The Joule number (J_0) can be expressed as:

$$J_0 = \frac{\lambda_{ref}}{2\pi}\frac{\sigma_{abs}}{V} \quad . \tag{3.11}$$

In Equation (3.11), V is the nanoparticles volume and λ_{ref} is the reference wavelength of a photon with energy of 1 eV ($\lambda_{ref} \approx 1240\ nm$). The simulations result from the nanospheres and nanorods are presented in Figure (3.9), where the insets in each figure show the absorption spectra of the respective nanostructure.

Figure 3.9: Joule number as a function of the dimensions of the nanostructure for (a) Au NSs and (b) Au NRs.

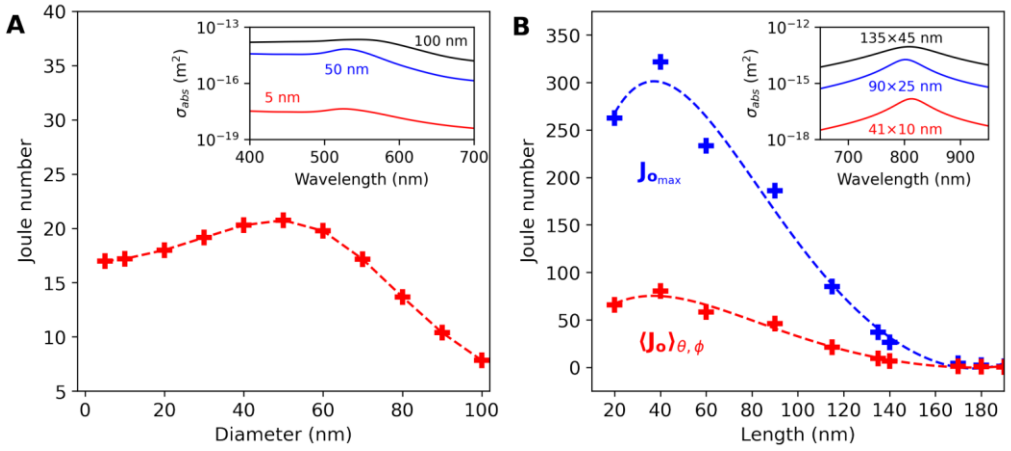

Source: [63]

The blue curve in Figure (3.9b) is the Joule number when the polarization of the light is parallel to the long axis of the nanorod. The average Joule number ($\langle J_0 \rangle_{\theta,\phi}$) is shown as the red line in Figure (3.9b), considering all the possible angular configurations (θ and ϕ spanning from 0º to 90º). From the insets of Figure (3.9), one can see that the highest absorption for the nanospheres is at 530 nm, while for the nanorods it is at 808 nm, thus determining the respective wavelength for PAM for each nanostructure. It is important to state that the concentration for all sets of samples was the same (for AuNSs, the final concentration among samples was 17.4 µg/mL, while for AuNRs it was 42 µg/mL). The samples were placed in a capillary tube with an internal (external) diameter of 1 mm (1.5 mm). From the simulations presented in Figure (3.9), it is expected that the 50 nm diameter nanosphere exhibits a higher photoacoustic signal due to the higher Joule number and, therefore, higher absorption. The results of the PAM performed for these nanoparticles are represented in Figure (3.10):

Figure 3.10: Photoacoustic microscopy of (a) Au NPs and (b) Au NRs. The photoacoustic signal of (c) Au NPs and (d) Au NRs.

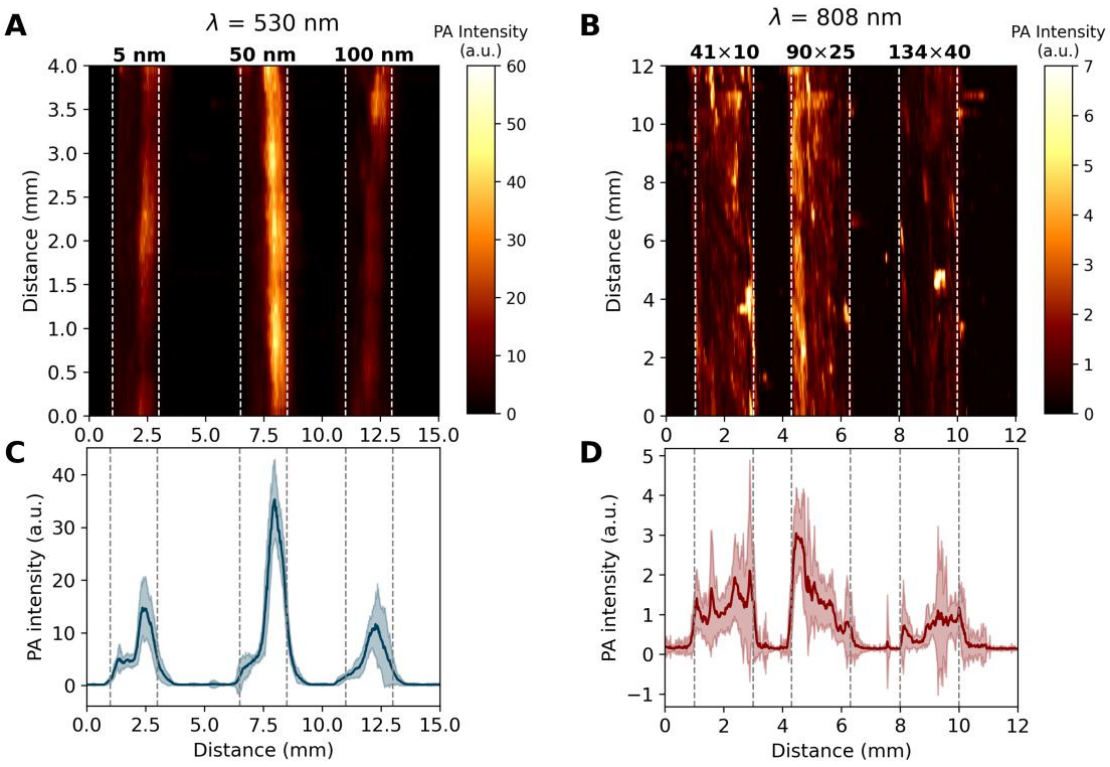

Source: [63]

As we can see from Figure (3.10), it's evident that the results from PAM are in perfect agreement with the simulations performed. As expected from the Joule number, represented in

Figure (3.9), the 50 nm nanosphere has the highest absorption and the highest photoacoustic signal. The results for the nanorods may, at first glance, seem somewhat contradictory to the simulations presented in Figure (3.9), since $\langle J_0 \rangle_{\theta,\phi}$ is higher for the 41 × 10 nm dimension NR. However, it is important to remember that nanorods are highly sensitive to the beam's polarization and also depend highly on their own orientation. Therefore, although the 41 × 10 nm nanorod may appear to have greater absorption, this is not entirely valid since there is a dependence on the beam's polarization. This feature explains why the photoacoustic signals from the 41 × 10 nm and 90 × 25 nm are comparable.

3.3.3 Er^{3+}-Yb^{3+} Nanoparticles

Rare-earth-doped (RED) nanoparticles absorbing in the biological window are promising candidates for working as contrast agents for photoacoustic imaging, providing high-contrast and high-resolution for photoacoustic imaging [64–66]. Biocompatibility is required for materials choice to act as contrast agents, and RED has already been used for this purpose in photoacoustic imaging [67,68]. In this work [69], Er^{3+}-Yb^{3+} co-doped KGd_3F_{10} nanoparticle is proposed as a contrast agent for PAM. Another set of this nanoparticle was also functionalized with SiO_2 (Er^{3+}-Yb^{3+}:KGd_3F_{10}@SiO_2). The results of the PAM are in Figure (3.11) for different wavelengths (520 and 980 nm).

Figure 3.11: Photoacoustic microscopy of nanoparticles. (a) and (b) Yb^{3+}/Er^{3+}:KGd_3F_{10} nanoparticles; (c) and (d) Yb^{3+}/Er^{3+}:KGd_3F_{10}@ SiO_2. Figures (a) and (c) the wavelength used was 980 nm; and (b) and (d) 520 nm.

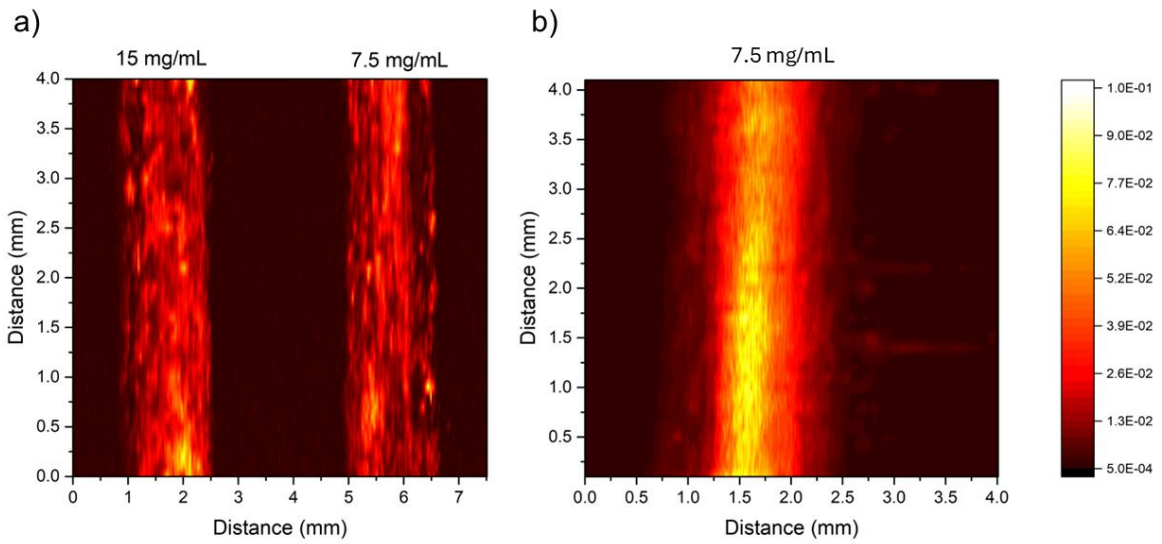

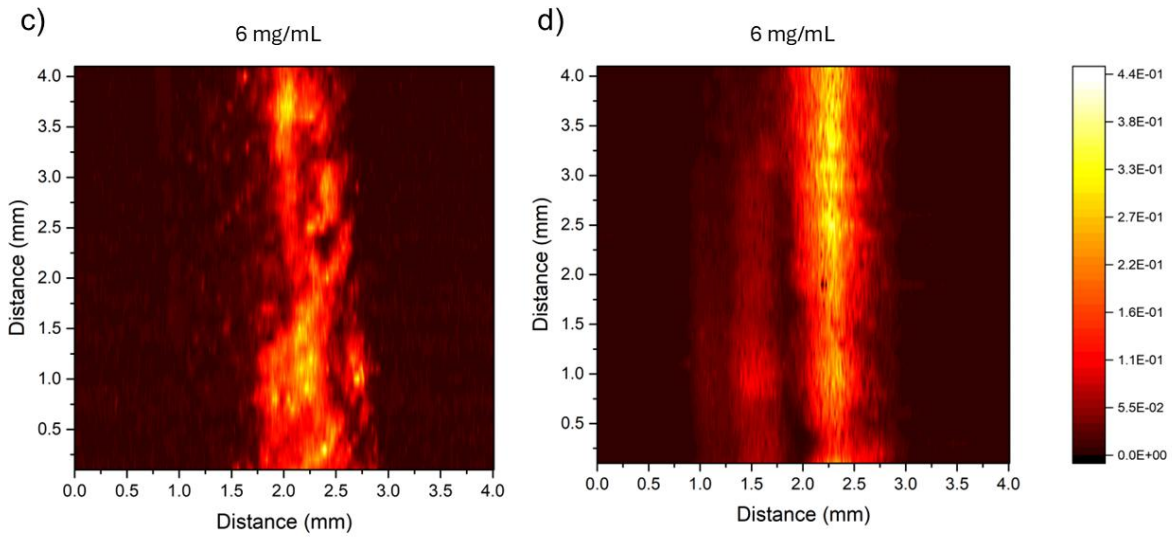

Source: [69]

The photoacoustic microscopy measurement in Figure (3.11) shows good resolution and contrast for the core-shell sample, as indicated by the color scale on the right side, which means that the functionalization of the NPs increases the optical absorption at both wavelengths. The good absorption at 980 nm is due to the Yb^{3+}-Er^{3+} dopants, which are extensively exploited because of their up-conversion emission, as shown in Figures (3.11a) and (3.11c). The 980 nm beam excites the Yb^{3+} ion more efficiently, and through energy transfer, excites the Er^{3+} ion.

Figure 3.12: Simplified energy diagram for the Er3+ and Yb3+ based NP, showing the excitation path at 980 nm and 520 nm.

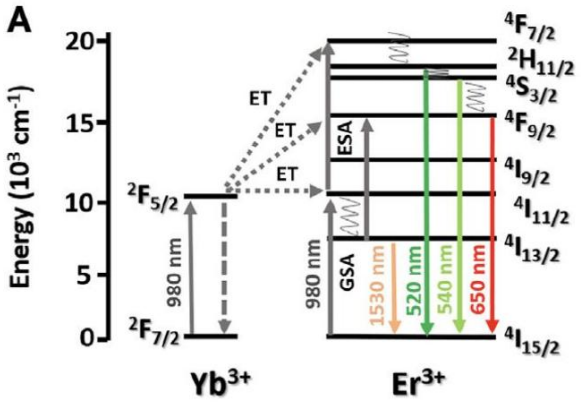

Source: [69]

The good results on PAM concluded that the Er^{3+}-Yb^{3+} co-doped KGd_3F_{10} cores and core-shell Er^{3+}-Yb^{3+}:KGd_3F_{10}@SiO2 are very promising candidates for photoacoustic imaging as contrast agents for biomedical applications because of the high absorption in the biological window, implying that there will be a higher penetrability in the tissues.

3.3.4 Iron Oxide (Fe_3O_4) Nanoparticles

Photoacoustic Microscopy has been widely studied for biomedical applications [37], and the use of nanoparticles as contrast agents — as biosensors (for sensing metal ions, pH, enzymes, temperature, hypoxia, reactive oxygen species, and reactive nitrogen species) and in bioimaging (lymph nodes, vasculature, tumors, and brain tissue) — improves photoacoustic imaging performance, enhancing the contrast of the final image [70,71], as mentioned before. One kind of contrast agent is magnetic nanocarriers, such as iron oxide (Fe_3O_4), which have already been studied as nanocarriers for drug delivery systems [72].

In this particular work [73], a collaboration with the Rare-earth Laboratory (BSTR) of UFPE, a nanoparticle of Fe_3O_4 coated with β-cyclodextrin (β-CD) to load phyllacanthone—a compound with antitumor activity—is studied. The nanocomposite (Fe_3O_4@βCD-PHY) presents good absorption in the near-infrared (NIR) region, around 1064 nm, making it a promising contrast agent due to the fact that this particular wavelength lies in the second biological window (1000–1400 nm), where biological tissues are more transparent to light [43]. For this measurement, 200 µL microtubes were used to place the sample on the acrylic holder. The size of the microtube is larger than the capillary tube used in the previous measurements, so to avoid a very long acquisition time, the laser beam diameter and the stage step size were increased to 1 mm, but the optical fluence was kept at 83 mJ/cm², below the maximum exposure for this wavelength [74]. Also, a pulsed Q-switch Nd:YAG (Continuum, Surelite II) emitting in 1064 nm laser was used as light source, as mentioned before.

Figure 3.13: Photoacoustic microscopy of iron oxide composite. (a) Image of the detection, (b) two samples in different concentrations with an empty microtube and one with the solvent; (c) PAM of the nanocarrier in different concentrations and the iron oxide.

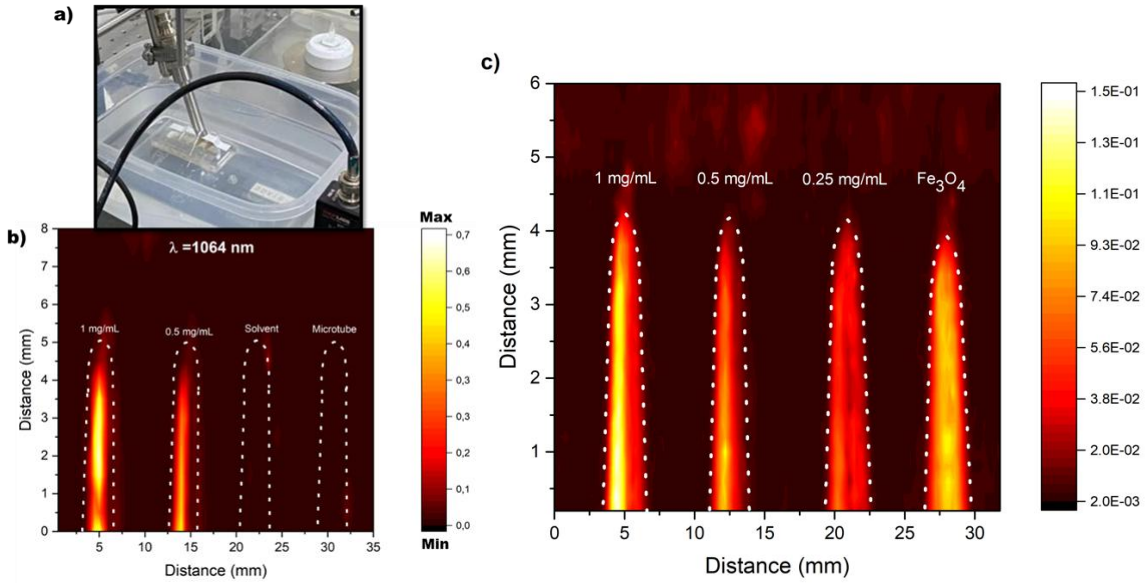

Source: [73]

In Figure (3.13b), one can notice that there is no photoacoustic signal coming either from the solvent or from the microtube, which means that the measured photoacoustic signal in every measurement comes from the samples. Figure (3.13c) shows that although the highest photoacoustic signal comes from the highest concentration nanocarrier, there is a considerable signal generated from the ones with lower concentration. Since the 1 mg/mL nanocarrier concentration sample had the highest photoacoustic signal, phyllacanthone (PHY) was added to this nanocarrier, and photoacoustic microscopy was performed comparing the signal from the nanocomposite and the nanocarrier, as shown in Figure (3.14).

Figure 3.14: Photoacoustice microscopy of the nanocarrier (on the left) and the nanocomposite (on the right).

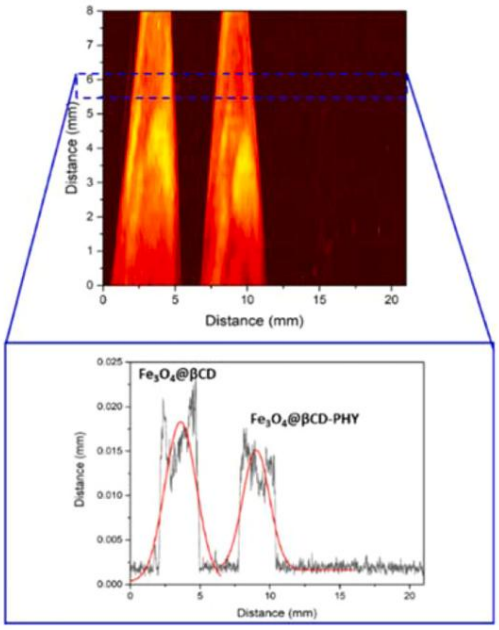

Source: [73]

After confirming that the nanocomposite has a good photoacoustic signal, a measurement with biological tissue was performed, placing chicken skin above the samples to simulate a biomedical application and see if this sample could be used as a nanocarrier for cancer diagnosis. The result is presented in Figure (3.15):

Figure 3.15: Photoacoustic microscopy with biological tissue with different thickness.

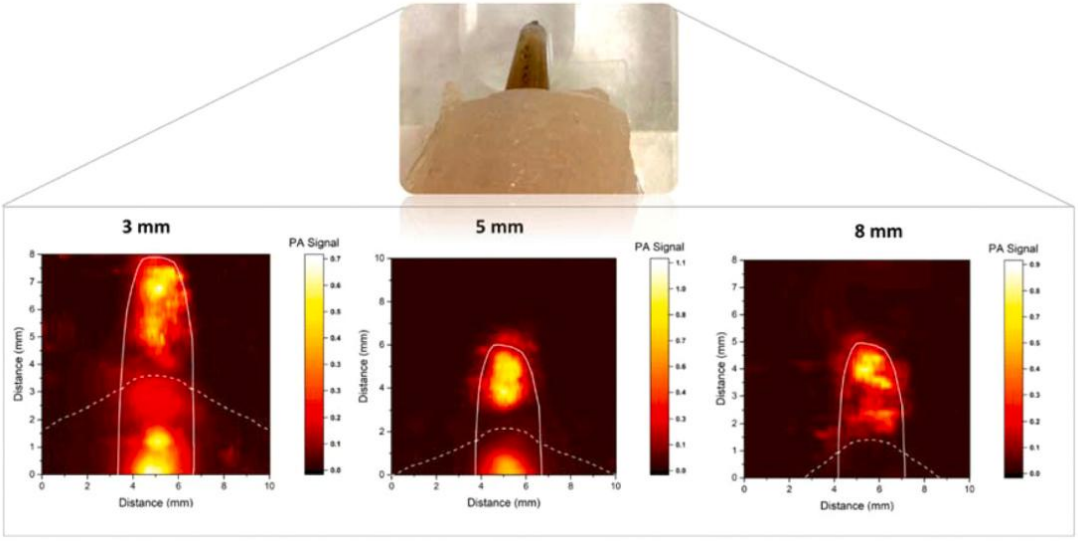

Source: [73]

As one can see, in Figure (3.15) three PAM were performed with different biological tissue thickness. For the thinner layer, the signal is almost unchanged. As the thickness increases, the photoacoustic signal decreases due to light attenuation, but even with a 5 mm thick tissue the photoacoustic signal is achievable and therefore confirms this nanocarrier as a promising candidate for biomedical applications.

3.4 CONCLUSION

The dependence of the photoacoustic signal on the absorption of the material makes this technique an excellent tool for material characterization and imaging. Besides, the capability of studying amorphous, powdered, solid, and gaseous samples makes it an interesting technique to be used.

The four results presented show how powerful photoacoustics can be. Measuring how the photoacoustic signal changes with optical fluence is an easy experiment to determine two-photon absorption in any kind of material, as observed in the first result on TiN. Another interesting feature of photoacoustics is the possibility of building an imaging system, such as photoacoustic microscopy (PAM). For all four samples, the PAM measurements are in complete accordance with what was expected from the absorption measurements and theoretical calculations, as presented in the gold nanoparticle results, where PAM was used to confirm not only the size-dependent SPR.

Photoacoustic microscopy proved to be very effective in absorption-based measurements, as expected. By combining the optical contrast with the resolution of acoustic techniques, it is possible to perform biological tests with new contrast agents for biomedical applications, as reported in the iron oxide sample.

4 TERAHERTZ

This chapter is dedicated to presenting the basic principles of terahertz (THz) radiation and explaining the most common systems used in its numerous applications. First, I will explain the spectral region of THz radiation and its importance in different fields of research. I will briefly describe the generation and detection processes of THz pulses and how they can be measured in a laboratory setting. After that, I will introduce two techniques for sample characterization: Terahertz Time-Domain Spectroscopy (THz-TDS) and Optical Pump–Terahertz Probe (OPTP). I will conclude this chapter by presenting some results obtained during my internationalization program at the Institut National de la Recherche Scientifique (INRS, Canada), where I built and performed THz-TDS measurements on 2D Transition Metal Dichalcogenides (TMDs) and designed a continuously tunable filter for a THz two-wire waveguide for telecommunication systems, with simulations showing great potential for future applications.

4.1 THEORY

The terahertz (THz) spectral range, also known as the THz gap or far-infrared (FIR), spans the electromagnetic spectrum from 30 μm to 3 mm, corresponding to frequencies between 100 GHz (0.1 THz) and 10 THz, as shown in Figure (4.1). In recent years, these frequencies have gained significant attention for a wide range of applications, including sample characterization, wireless communication, sensing, imaging, and positioning [75]. However, studying this region has not been without challenges. Historically, the THz range has been considered one of the most difficult parts of the electromagnetic spectrum to explore due to the lack of bright sources and sensitive detectors [76].

Figure 4.1: Electromagnetic spectrum highlighting the THz gap.

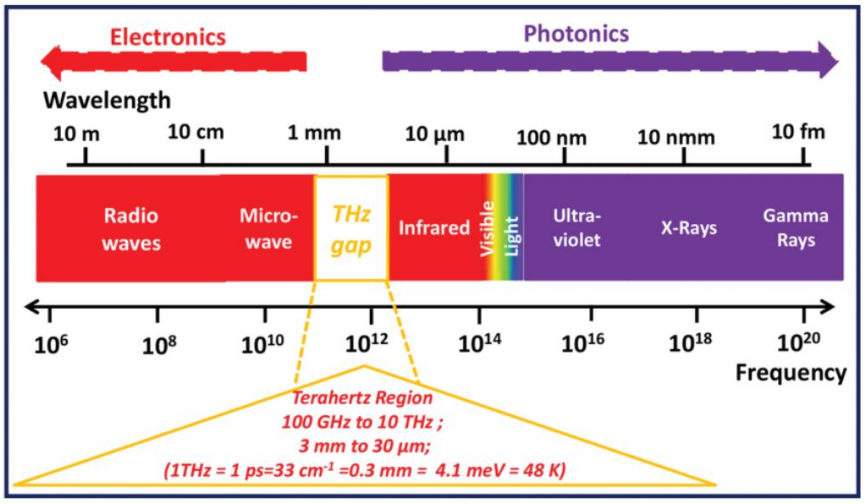

Source: [77]

Almost one hundred years after the near infrared experiment by Herschel [78], the first significant experiment on the THz region was only reported in 1893 by Heinrich Rubens [79], in which he studied the refraction of long-wavelength rays in rock salt, sylvite, and fluorite. He continued to study these long-wavelength rays for almost 30 years, making this period known as Rubens' era [80]. One of his major contributions to the study of long-wavelength rays is related to Planck's Radiation Law, which incorporates the long-wavelength radiation results by Rubens. A remarkable achievement was made in 1924, when the first generation of a THz source from a Hertzian dipole was produced, with wavelengths of 90 µm [81] and 220 µm [82]. Most of the early works in the FIR focused on instrumentation, mainly in the generation process, since the bolometer, invented by Langley in 1880 [83], was almost universally used for detecting infrared radiation [80]. Only in 1947 Marcel Golay invented a pneumatic infrared detector, now known as Golay cell, an opto-acoustic device capable of measuring infrared radiation [84].

All these inventions were an important step towards the so-called "THz era," starting in the early 1950s, when several instruments that are still in use today were fabricated, such as photoconductive detectors [85] and germanium bolometer [86]. Of course, the most important contribution was the laser itself, which led to the first high power far infrared laser in 1964 [20]. From that moment, the development of new lasers sources was inevitable and the first optically pump far-infrared laser was built [87].

Over the years, significant advancements have been made in instrumentation, alongside numerous efforts focused on practical applications. One notable milestone was achieved in 1974 when the first terahertz image was captured using a THz gas laser [88]. Since then, THz imaging science and technology have progressed tremendously. THz radiation offers unique advantages for imaging, as it occupies a distinct region of the electromagnetic spectrum. As a result, THz images provide complementary information to those obtained using microwaves, infrared, visible light, ultraviolet, or x-rays [89]. Compared to lower-frequency imaging, THz imaging benefits from superior spatial resolution due to its shorter wavelength. Additionally, many common materials — such as paper and cardboard — are relatively transparent in the THz range, making it particularly useful for security applications, including the detection of drugs and explosives [90–92]. Furthermore, every explosive and narcotic have a distinct THz spectral signature, enabling precise differentiation between illicit substances and benign compounds.

Another great feature is the fact that THz radiation is very sensitive to polar molecules, allowing the observation of intermolecular vibrations [93]. This feature, combined with the fact that water content in malignant tissues has been observed in various tumor types and is commonly used as a marker for malignancy, makes THz imaging possible with excellent contrast, without any contrast agent [94,95]. Terahertz has also been applied to study microorganisms [96,97], organic compounds [98–102] and in dentistry [103–107].

Obviously, the THz range is not restricted to imaging and biomedical applications only. Nowadays, wireless data traffic has drastically increased, demanding higher speeds for wireless communication [75]. The 5G technology is becoming obsolete, and data rates on the order of 100 Gbps or more will flourish at frequencies above 100 GHz, where the available spectrum is massively abundant. Thus, the terahertz band is envisioned as a key wireless technology to satisfy this high demand [108–110].

The vast potential of the THz region makes it a highly promising area for research, and conducting experiments within the THz regime is of significant interest in the field. As a result, understanding how to generate and detect THz pulses in a laboratory to perform experiments is fundamental.

4.1.1 Generation

Generating THz beams has been a big challenge over the past years. Nowadays, there are different means to do that, but only those called “tabletop sources” (the ones we can have in a laboratory, whose basic principle involves a femtosecond laser) will be presented. Under these conditions, photoconductivity and nonlinear optical processes are the two major techniques that have been used to generate THz electromagnetic transients from femtosecond lasers [111].

A photoconductive antenna (PCA), represented in Figure (4.2), operates as a photoconductive switch. The idea is to generate electric currents by modulating the resistance of a semiconductor through the absorption of a short laser pulse. Such a device is sometimes called “Auston switch” after its inventor, David Henry Auston, and it was invented in 1974 [112]. We can divide the THz generation by PCAs into three different stages: the antenna before illumination, the antenna when the optical pulse meets the antenna gap, and finally the THz pulse emission.

A supply voltage V between the two antenna contacts results in an electric field in the semiconducting antenna gap between the metal contacts. Since the semiconductor is highly resistive, there are no free electrons in the conduction band, and therefore nothing happens before the IR beam reaches the antenna gap. The external voltage is provided by a pulse generator with a square shape at a frequency of some kHz.

When a short optical pulse meets the antenna gap, the optical energy is absorbed, and free carriers are created in the semiconductor material. Each absorbed photon creates a free electron, which follows the applied electric field, creating a short current pulse j(t) in the semiconducting gap material. In other words, the optical pulse acts as a switch for an electric circuit, as represented in Figure (4.2c).

Figure 4.2: Sketch of a photoconductive antenna. (a) side view, with a silicon hyperhemispherical lens for collimation; (b) back view, showing the wires connections and the semiconductor chip; (c) circuit representation of the working principle of the antenna.

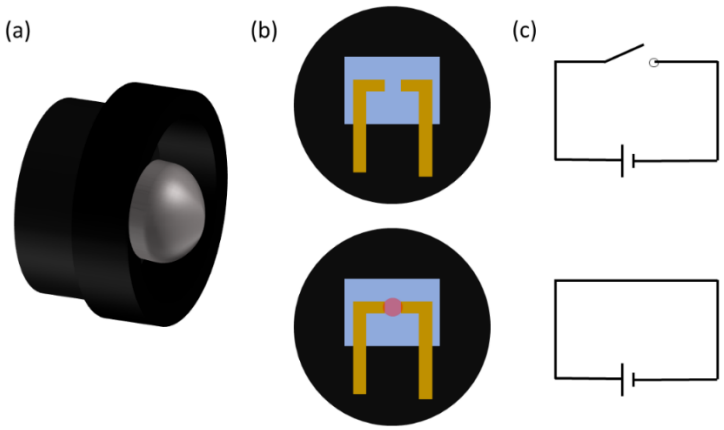

Source: The author (2025)

While the IR beam is on the antenna gap, an electromagnetic field is emitted by the dipole if the current pulse changes with time. The current increases during the illumination of the gap and emits the first part of the THz pulse. Eventually, the current will decrease because the electric field is subsequently compensated by the transferred carriers, then the second part of the THz pulse is emitted with a reverse polarization direction. The THz pulse has the shape of the derivative of a Gaussian pulse, as the IR pulse. It is longer than the optical pulse because it is determined by the antenna's length L. In Figure (4.3) there is a simple comparison between the current/optical pulse and the THz waveform.

Figure 4.3: Comparison between the optical pulse and the THz pulse generated by the photoconductive antenna.

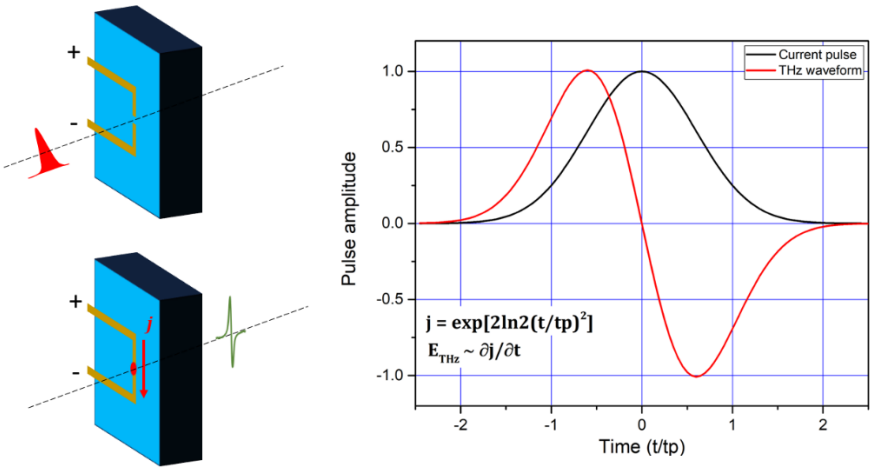

Source: The author (2025)

One important feature of the PCAs regards the polarization of the generated beam. This polarization will be along the axis of the gap of the circuit on the antenna, which means that it's possible to change the polarization of the beam by simply rotating the antenna itself.

Another process to generate THz pulses is based on nonlinear optics. Optical rectification (OR) [113] is a specific case of difference frequency mixing (DFG) and is described by the second-order nonlinear susceptibility $\chi^{(2)}$ [114]. For sufficiently high intensities, the polarization in a material can be described as a linear term in the electric field but also includes higher-order terms. These higher-order terms give rise to a nonlinear polarization ($\boldsymbol{P}^{NL}$), which is customarily written as the following expansion in powers of the electric field [115]:

$$\boldsymbol{P}^{NL} = \epsilon_0\left[\chi^{(2)}\boldsymbol{EE} + \chi^{(3)}\boldsymbol{EEE} + \chi^{(4)}\boldsymbol{EEEE} + \cdots\right] \quad . \tag{4.1}$$

Here, the time dependence of the polarization and the electric field is omitted, and the bold letters indicate vectors. Since OR is a second-order nonlinearity, hereafter we are going to consider only the first non-linear term, related to $\chi^{(2)}$. We can perform a Fourier transform and write the nonlinear polarization in the frequency-space (also called ω-space) as:

$$\widetilde{\boldsymbol{P}}^{(NL)} = \epsilon_0\chi^{(2)}\widetilde{\boldsymbol{E}}_{\boldsymbol{1}}(\omega_1)e^{ik_1 z}\widetilde{\boldsymbol{E}}_{\boldsymbol{2}}^{*}(\omega_2)e^{-ik_2 z} \quad . \tag{4.2}$$

In eq. 4.2, ω_1 and ω_2 are the possible pump frequencies of the pulse which has a bandwidth $\Delta\omega$ related to the temporal width of the pulse $\Delta\tau$ according to the temporal bandwidth product (also called duration-bandwidth product). Considering that the pump pulse has a gaussian shape, this relation can be written as:

$$\Delta\tau\Delta\omega = 4\ln 2 \quad . \tag{4.3}$$

From Maxwell's equation we can derive the electromagnetic wave equation with the polarization as a source:

$$\nabla^2\boldsymbol{E} - \frac{1}{c^2}\frac{\partial^2}{\partial t^2}\boldsymbol{E} = \frac{1}{c^2\epsilon_0}\frac{\partial^2}{\partial t^2}\left[\boldsymbol{P}^{(L)} + \boldsymbol{P}^{(NL)}\right] \quad , \tag{4.4}$$

where $\boldsymbol{P}^{(L)}$ is the linear polarization, which we can write as $\boldsymbol{P}^{(L)} = \epsilon_0(n^2(\Omega) - 1)\boldsymbol{E}$. Therefore:

$$\nabla^2\boldsymbol{E} - \frac{n^2}{c^2}\frac{\partial^2}{\partial t^2}\boldsymbol{E} = \frac{1}{c^2\epsilon_0}\frac{\partial^2}{\partial t^2}\boldsymbol{P}^{(NL)} \quad . \tag{4.5}$$

Defining $\omega_1 - \omega_2 = \Omega$ and $k_1 - k_2 = k_{12}$, in frequency space we can write this equation as:

$$\frac{d^2}{dz^2}\tilde{E}(z) + \frac{n^2\Omega^2}{c^2}\tilde{E}(z) = \frac{\Omega^2}{c^2\epsilon_0}\tilde{P}^{(NL)} \quad , \tag{4.6}$$

$$\frac{d^2}{dz^2}\tilde{E}(z) + \frac{n^2\Omega^2}{c^2}\tilde{E}(z) = \frac{\Omega^2}{c^2}\chi^{(2)}\tilde{E}_1(\omega_1)\tilde{E}_2^*(\omega_1 - \Omega)e^{ik_{12}z} \quad . \tag{4.7}$$

The solution for this equation is the following:

$$\tilde{E}(z) = -\frac{\Omega^2}{c^2(k_{12} - K^2)}\chi^{(2)}\tilde{E}_1(\omega_1)\tilde{E}_2^*(\omega_1 - \Omega)\left[ae^{iKz} + be^{-iKz} + e^{ik_{12}z}\right] \tag{4.8}$$

where $K \stackrel{\text{def}}{=} n^2\Omega^2/c^2$ and a and b are constants to be defined from the boundary conditions of the system. Considering that we are focused on the transmission of the beam, we can neglect the reflection part ($b = 0$). Also, $\tilde{E}(z = 0) = 0$, implying in $a = 0$. Therefore:

$$\tilde{E}(z) = -\frac{\Omega^2}{c^2(k_{12}^2 - K^2)}\chi^{(2)}\tilde{E}_1(\omega_1)\tilde{E}_2^*(\omega_1 - \Omega)\left[e^{ik_{12}z} - e^{iKz}\right] \quad . \tag{4.9}$$

Writing $\Delta k = k_{12} - K$:

$$\tilde{E}(z) = -\frac{\Omega^2}{c^2(k_{12} + K)}\chi^{(2)}\tilde{E}_1(\omega_1)\tilde{E}_2^*(\omega_1 - \Omega)\frac{e^{i\Delta kz} - 1}{\Delta k} \quad . \tag{4.10}$$

If ω_1 and ω_2 have the same polarization, we can show that the phase matching condition ($\Delta k = 0$) is easily satisfied when we consider $\omega = \omega_1 + \frac{\Omega}{2} = \omega_2 - \frac{\Omega}{2}$ and the refractive index can be written as:

$$\tilde{n}\left(\omega \pm \frac{\Omega}{2}\right) = \tilde{n}(\omega) \pm \frac{\Omega}{2}\frac{d\tilde{n}}{d\omega} \quad . \tag{4.11}$$

This condition is equivalent to the condition that the phase velocity of the THz radiation is equal to the group velocity of the pump pulses and, therefore, phase matching is fulfilled [111]. We can also check from Equation (4.10) that the electric field is proportional to $\boldsymbol{\Omega}$. Considering a 100-fs laser pulse, the bandwidth $\Delta\omega$ is around 5 THz, as we can check from the temporal bandwidth product expressed in Equation (4.3). This means that by selecting a proper material, it's possible to generate THz pulses from femtosecond lasers. Obviously, there are some requirements for these selected materials for optical rectification: they must possess a relevant nonlinear susceptibility, and since it is necessary to use high intensities, the damage threshold should be high enough to tolerate such intensities. Lithium niobate ($LiNbO_3$), lithium tantalate ($LiTaO_3$), and zinc telluride (ZnTe) are the most common crystals used for OR to generate THz pulses.

It's important to state that, since the focus of this section is only on "tabletop sources," THz sources such as synchrotrons [116,117], free-electron lasers [118], quantum cascade lasers [119] and gas lasers [20] have not been discussed.

4.1.2 Detection

Once the THz pulse is generated, it must be detected. Most optical detection systems measure the intensity of the light reaching the detector, and the phase information about the electric field is lost. One reason the THz detection system is so powerful is that it measures the electric field associated with THz radiation, rather than the light intensity as is common in most optical detection systems. This means that both amplitude and phase are acquired simultaneously. Measuring THz pulses based on a femtosecond laser follows the same principles as those explained for the generation and can be achieved by either PCAs or nonlinear optical methods [120].

The working principle of a photoconductive antenna as a detector is almost the same as in the emitter case. The difference lies in the fact that the detection antenna is not externally biased. Here, an optical probe beam and a THz pulse simultaneously interact with the switch, with the former producing charge carriers and the latter driving them to form a current. It's important to state that the measured electric field occurs at one moment: when the probe pulse reaches the antenna. Therefore, to obtain the entire waveform, we need to apply what is called the "sampling technique."

The principle of the sampling technique is to create a delay between the two pulses: the THz and the probe. By doing this, it's possible to measure the electric field at different times and the entire waveform is obtained. Figure (4.4) shows a sketch of the acquisition of the waveform: when two mirrors are placed on a motorized stage and moved, a delay in the probe beam is created and the waveform is acquired. For each mirror position, represented in different colors, a single point is measured. Combining all these points, the waveform is obtained, as represented in Figure (4.4). Thus, the sampling technique maps the waveform by creating a delay between the THz pulse and the probe.

Figure 4.4: Working principle of sampling technique. The colored squares on the left represent a different time point in the THz waveform, on the right side of the figure.

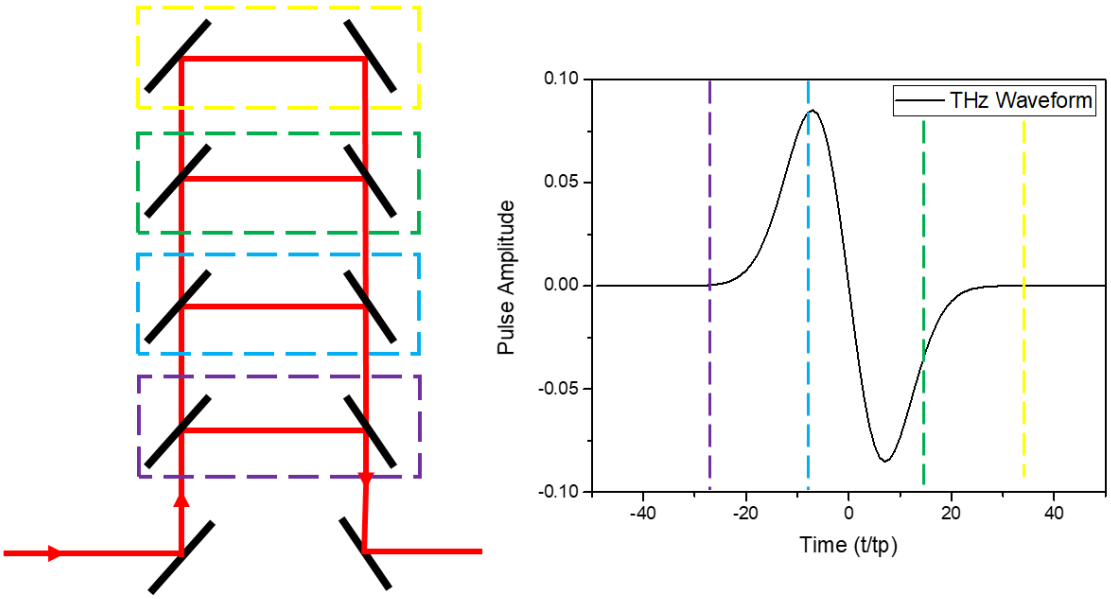

Source: The author (2025)

The current created by the THz electric field on the antenna is on the order of picoamperes to nanoamperes [8]. For such small currents, an amplifier capable of measuring the signal within a noisy background is required. For this purpose, a lock-in amplifier is the most suitable equipment because it can selectively amplify a signal at a known reference frequency. The noisy incoming signal is multiplied by a sine wave at the reference frequency and then sent through a low-pass filter to obtain the DC component, which is the signal of interest [121]. In the case of the photoconductive switches, the reference frequency is the one from the function generator that supplies the antenna.

Besides the photoconductive switch, it's also possible to detect the THz signal by electro-optic sampling (EOS) [122], represented in Figure (4.5). In this method, based on the Pockels effect, an applied electric field (THz pulse) modulates the birefringence of a detector crystal [122]. Thus, if the visible sampling pulse travels through the crystal at the same time as one point in the THz pulse, its polarization will be rotated. The magnitude of rotation is proportional to the magnitude of the THz field, and the direction of rotation is proportional to the sign of the field. Therefore, the modulation of the polarization of the probe beam can be analyzed to provide information about both the amplitude and the phase of the THz pulse that created the birefringence. The thickness of the crystal plays an important role in the acquired signal, since there is a trade-off between sensitivity and frequency response [123]. If the crystal is too thick, it will have a longer interaction length. On the other hand, there will be a group velocity mismatch between the two pulses. The most common crystals used for EOS are lithium tantalate ($LiTaO_3$), lithium niobate ($LiNbO_3$), and zinc telluride (ZnTe) [124]. Sampling techniques and the lock-in amplifier are also necessary to acquire the whole waveform of the THz pulse. Since the OR does not need a function generator, chopping the probe pulse at a particular rate (kHz or MHz) is the most common way to have a reference frequency for the lock-in amplifier.

Figure 4.5: Working principle of electro-optic sampling.

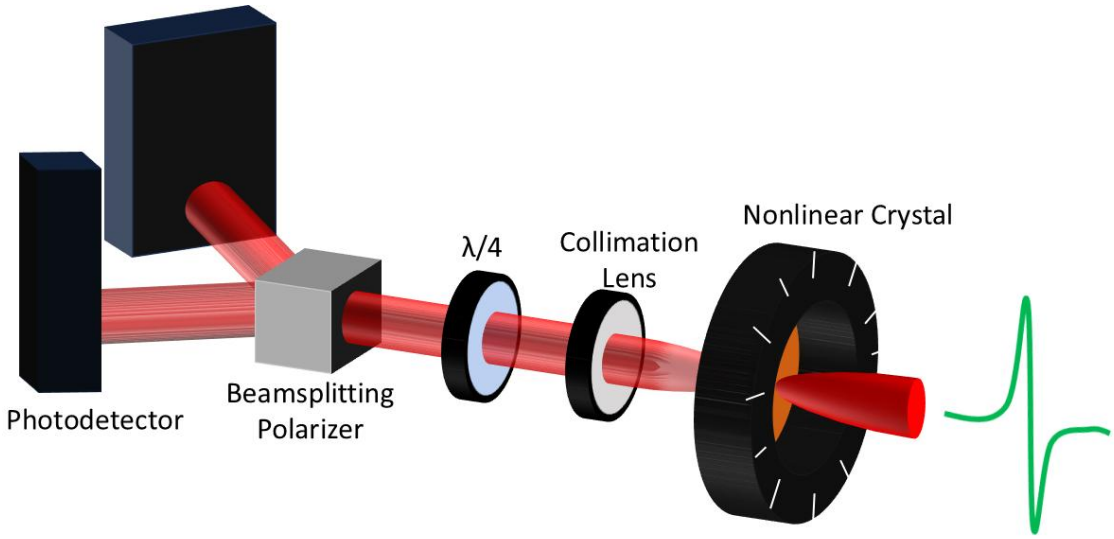

Source: The author (2025)

Although it's possible to use both generation and detection techniques interchangeably, there are some considerations to be made. The first and most important one regards the bandwidth [123]. The bandwidth of the detector must be higher than that of the emitter to acquire the whole waveform of the THz pulse; otherwise, information will be lost. Since photoconductive switches have a smaller bandwidth, the combination of a nonlinear crystal as a THz generator and a photoconductive antenna as a detector is not a good idea. Photoconductive antennas have superior detection responsivity, and their signal-to-noise ratio is typically far better for chopping frequencies of a few kHz [125]. Meanwhile, in EOS it's easily possible to calibrate the THz electric field [123], and since it is a purely optical technique, it allows faster acquisition (rapid delay line scan) because the response time is faster than the electrical one. Besides, due to its low dispersion, EOS plays an important role in THz imaging.

Now that the generation and detection processes have been explained, the applications for THz pulses will be presented. To begin with, it will be shown how the capability of measuring directly the electric field (both amplitude and phase) makes THz a powerful tool for material characterization and spectroscopy.

4.2 SAMPLE CHARACTERIZATION

4.2.1 Terahertz Time Domain Spectroscopy (THz-TDS)

From Terahertz Time Domain Spectroscopy (THz-TDS) measurements, one can obtain the frequency-dependent complex refractive index of the sample in question. One of the greatest advantages of this technique is that, since the transient electric field is measured (both amplitude and phase), the real and imaginary parts of the refractive index can be measured simultaneously, which means that the Kramers-Kronig relationship is not necessary. Thus, the goal of the THz-TDS experiment is usually to extract the material response, such as the refractive index and the optical conductivity [126].

Due to its long wavelength, THz radiation is suitable for noninvasive detection without damaging the material under study, as mentioned before. Besides, it's very sensitive to various kinds of resonance, such as vibrational, translational, and rotational. Additionally, the fact that THz waves are nonionizing, non-invasive, and have good penetration depth makes them suitable for identifying and analyzing a variety of materials. Therefore, THz-TDS is widely used in pharmacy, dentistry, biomedicine, security screening, military use, and so on [77].

The low energy and the transparency of terahertz pulses for paper and plastic bags make it possible to achieve nondestructive inspection for illicit drugs, such as heroin and morphine [90]. Other drugs like ecstasy (MDMA) and cocaine can also be detected due to their unique fingerprints in the THz range [92]. Terahertz TDS can also be applied to explosive and weapons detection for security applications [90,91,127,128].

In dentistry, the THz-TDS system has been used mainly for diagnosis and characterization [107]. It has been shown that carious tissues typically have greater THz transmission attenuation than healthy ones, allowing the diagnosis of caries in early stages [105]. There are also studies showing that the refractive index of enamel is higher than dentin [129] and characterizing primary and permanent teeth [103].

There is also a great number of THz-TDS measurements for quality control in the food industry. There are reports about using the spectroscopy for antibiotic detection in milk and egg powder [130] and to pesticide detection in food powders [131]. Characterization of optical properties of some vegetable oils have also been reported [132], and the prediction of sugar and alcoholic content in some beverages [133].

An example of experimental setup, working on transmission mode and electro-optic sampling detection, is shown in Figure (4.6).

Figure 4.6: Terahertz time domain spectroscopy setup (THz-TDS). M, mirror; PBS, polarizing beamsplitter; PCA, photoconductive antenna; DL, delay line; L, lens; PM, parabolic mirror; PD, photodetector; LA, lock-in amplifier; FG, frequency generator.

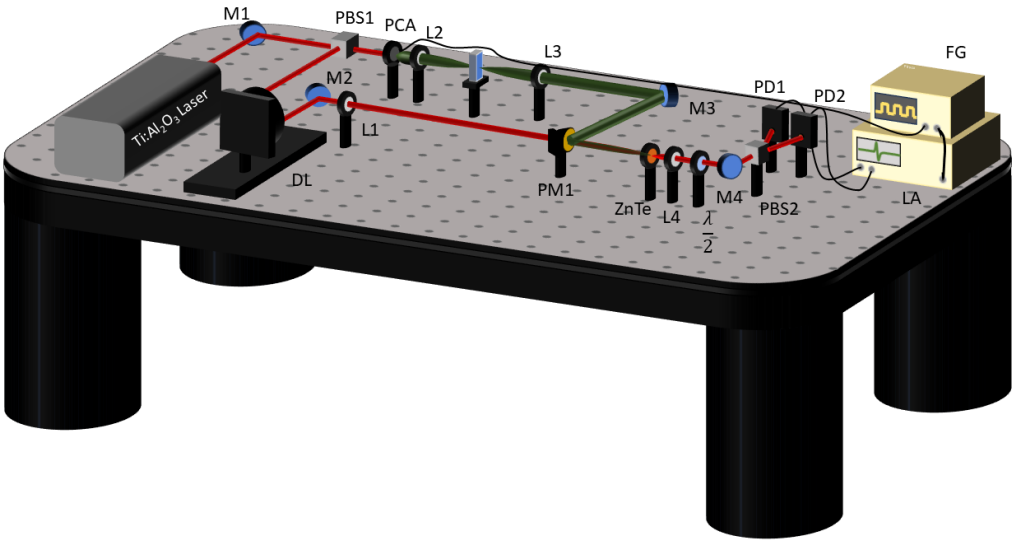

Source: The author (2025)

The procedure to obtain the complex refractive index is quite simple: first, the THz electric field $E_{ref}(t)$ of a reference material - could be just air or a substrate in which the sample is deposited - is measured. A Fourier transform is performed to write $E_{ref}(\nu)$. The following step is to repeat the same procedure, but now for the sample in question. Thus, writing $E(\nu)$ for the sample, the next step is to solve the transfer function $T(\nu)$ – which is simple the ratio between the sample and reference electric field in the Fourier space.

$$T(\nu) = \frac{E(\nu)}{E_{ref}(\nu)} \quad . \tag{4.12}$$

After solving the boundary conditions, in Equation (2.6), for all interfaces, the theoretical transfer function is built, and the complex refractive index is obtained after numerical calculations, comparing the experimental data $T(\nu)$ and the theoretical one. The complex

transfer function is written depending on the experiment itself. For example, suppose one sample is a layered material on a substrate, as represented in Figure (4.7).

Figure 4.7: THz pulse interaction with sample and substrate.

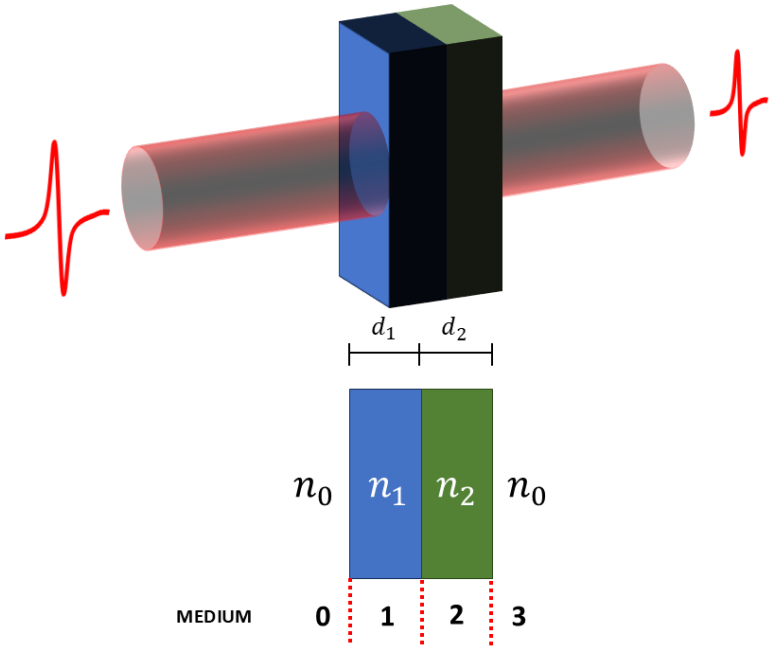

Source: The author (2025)

In this situation, it is better to use the transmission through the substrate alone without the sample material as a reference. The advantage of this referencing method is that the influence of the substrate thickness cancels out. The theoretical transfer function of this system can be easily built after introducing the Fresnel transmission and reflection coefficients (t_{ij} and r_{ij}):

$$r_{ij} = \frac{\tilde{n}_i - \tilde{n}_j}{\tilde{n}_i + \tilde{n}_j} \quad , \quad t_{ij} = \frac{2\tilde{n}_i}{\tilde{n}_i + \tilde{n}_j} \quad , \tag{4.13}$$

where the subscript *ij* represents the interface between the mediums *i* and *j*. Also, writing $P_j = e^{-ik_0 d_j n_j}$ as the propagation through layer *j* and considering the Fabry-Pérot etalon caused by partial reflections of *M* pulses, defined by [8]:

$$FP_{jkl} = \sum_{m=0}^{M} \left(r_{kl} P_k r_{jk} P_k\right)^m \quad . \tag{4.14}$$

From Figure (4.6), considering the material with refractive index n_2 as the substrate and the one with n_1 as the sample, the transfer function in the transmission mode is described by:

$$\frac{E(\nu)}{E_{ref}(\nu)} = \frac{t_{01}P_1t_{12}P_2t_{23}FP_{012}FP_{123}E_0}{t_{02}P_2t_{23}P_3FP_{023}E_0} = \frac{t_{01}t_{12}P_1}{t_{02}P_3}\frac{FP_{012}FP_{123}}{FP_{023}} \quad . \tag{4.15}$$

From Equation (4.15) it's possible to solve it for $\tilde{n}_1$ once the refractive index of the substrate is known. This equation can also be simplified in most cases, depending on the samples and the substrate's thickness and conductivity [8]. Silicon compounds are the best substrate materials for electronics [134], since they are the most transparent dielectric materials in the THz frequency range. Besides, they show little dispersion and a relatively constant refractive index in the THz frequency range [135]. Dai *et al.* performed a THz-TDS measurement on high-resistivity (HR) silicon to obtain its refractive index and the absorption coefficient. These results show that there is almost no absorption in the THz range and that the refractive index is almost constant (n = 3.417) between 0.5 THz and 4.5 THz, as shown in Figure (4.8). This is an important measurement, since the refractive index of the substrate must be considered when the THz-TDS measurement is performed with layered samples.

Figure 4.8: Silicon refractive index and power absorption coefficient from THz-TDS measurement.

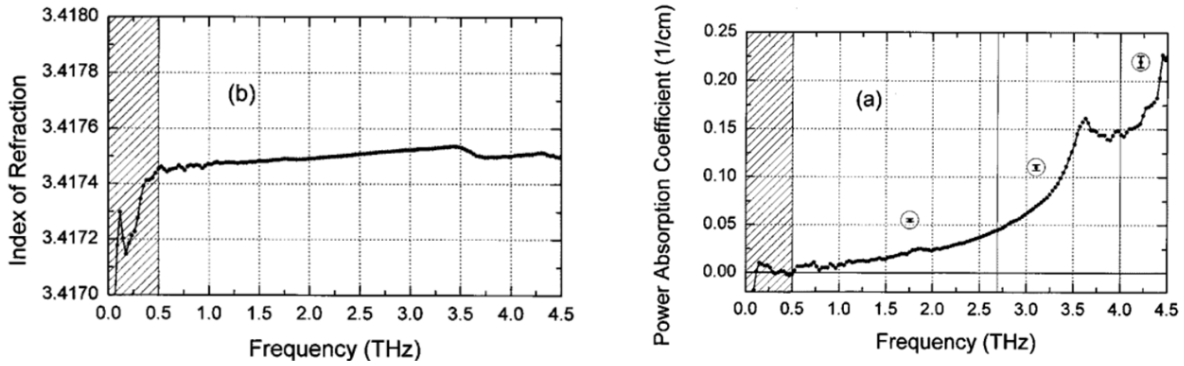

Source: [135]

It's important to state that these parameters measured by the THz-TDS technique are at equilibrium. Despite this limitation, there are two other techniques that probe charge carriers' dynamics and therefore measure the photoinduced change in conductivity resulting from the

photoexcitation of charge carriers. They are called Time-Resolved THz Spectroscopy (TRTS) and Optical Pump – Terahertz Probe (OPTP) [100].

4.2.2 Optical Pump Terahertz Probe (OPTP) and Time-Resolved Terahertz Spectroscopy (TRTS)

The main idea behind the Optical Pump – Terahertz Probe (OPTP) and Time-Resolved Terahertz Spectroscopy (TRTS) lies in a pump/probe system. To build this setup, basically one should add another beam path to the THz-TDS setup. This new path will act as the pump and must pass through a mechanical delay stage, which controls the time interval between the pump pulse and the THz pulse. This is known as the pump–probe delay time. The pump will induce some changes in the sample, while the probe measures how the system evolves over time as a result of this excitation. Both techniques are important tools to investigate quasiparticle dynamics in nanostructures on time scales that range from sub-picosecond to nanosecond [136].

In OPTP, the delay stage in the THz path is fixed at its maximum value, while the stage in the pump path is scanned. To guarantee a uniform photoexcited carrier density, the pump beam spot size must be larger than that of the THz pulse [137]. This technique records the change in the peak transmission of the THz beam as a function of the pump-probe delay time. Therefore, the transmission of the THz pulse will be measured before, during, and after the interaction between the pump and the sample. From this measurement, one can obtain photoconductivity decay, relaxation and scattering rates, and how the conductivity changes due to photoexcitation. Supposing that the THz transmitted pulse with and without the pump excitation are expressed by $T^{ON}(t)$ and $T^{OFF}(t)$, respectively, the fractional change in transmittance because of the photoexcitation will be given by:

$$\frac{\Delta T}{T_0} = \frac{(T^{ON} - T^{OFF})}{T^{OFF}} \quad , \tag{4.18}$$

where all these variables are frequency dependent. From this difference transmission the photoconductivity can be expressed by [136]:

$$\Delta\sigma(t) = \frac{1+\tilde{n}}{Z_0 d}\left[\frac{1}{1+\Delta T/T_0} - 1\right] \quad , \tag{4.19}$$

in which Z_0 is the impedance of free space ($Z_0 = 377\ \Omega$) and the refractive index is the one from the substrate.

There are numerous reports studying the photoconductivity of semiconductors using OPTP setup. As an example of a possible result from this kind of measurement, Figure (4.9) presents the results from Liu *et al.,* who studied the carrier relaxation dynamics of CdS and Se-alloyed CdS nanobelts [136].

Figure 4.9: Typical optical pump – terahertz probe measurement for CdS and $CdS_{0.65}Se_{0.35}$. (a) the THz amplitude of the transmitted pulse and (b) the pump – probe result.

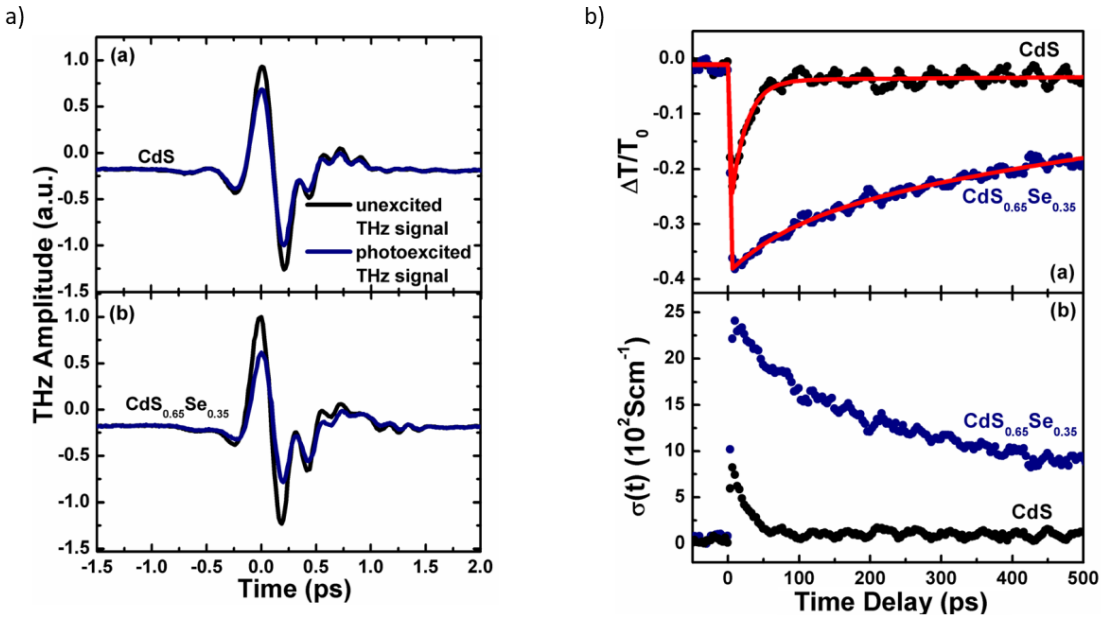

Source: [136]

From these 4 plots in Figure (4.9) it's possible to better understand how the measurement is done. Figure (4.9 a) brings the THz pulse recorded at 3.5 and 3.8 ps after pump excitation for CdS and $CdS_{0.65}Se_{0.35}$, respectively. The amplitude of the THz wave decreases because of the generation of free carriers, leading to an increase in conductivity. Meanwhile, Figure (4.9b) shows the differential transmittance of the THz pulse. In this situation, the THz delay stage is fixed at the maximum THz signal, and the pump path is scanned. A decrease in the transmission

is evident exactly when the pump and probe overlap in time, followed by an increase after photocarrier depletion, and from Equation (4.17), the photoconductivity is calculated.

The Optical Pump Terahertz Probe (OPTP) technique has been widely used to study the carrier dynamics of different materials, such as hexane [138], MoS_2 [139], graphene [140–142], InGaAs [143] and silicon [144] . Also, OPTP has also been applied to study the insulator-metal transition in vanadium dioxide (VO_2) films [145]. However, this technique has one limitation: since this measurement is done by fixing the THz signal at its maximum, it is assumed that the refractive index is constant for all THz frequencies. Therefore, this scan is not very suitable when the sample has a frequency-dependent photoresponse, since the change in transmission could be due to a change in the refractive index, and not to THz absorption by the free carriers. In this situation, Time-Resolved Terahertz Spectroscopy is more adequate [146], as it consists of taking a series of fixed pump delay scans at a variety of times after sample photoexcitation. Such technique will provide a 2D grid that maps the THz waveform for different pump delay times, as shown in Figure (4.10) [147]:

Figure 4.10: Terahertz-Time Resolved Spectroscopy (TRTS) plot example, showing the frequency dependence of the conductivity.

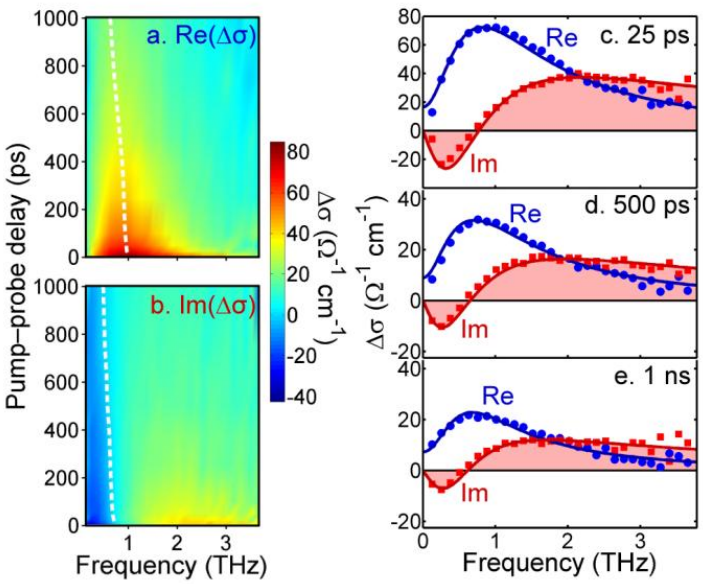

Source: [147]

These TRTS measurements were performed with GaAs/AlGaAs core-shell nanowires by fixing the pump delay and taking the THz waveform for each pump-probe delay. Each spectrum

measures the frequency-dependent conductivity at a fixed delay after photoexcitation at a fixed fluence, leading to a 2D counterplot of the conductivity of the studied material.

4.3 TERAHERTZ MEASUREMENTS RESULTS

In this section, I will present the results obtained during my internationalization program at INRS (Institut National de la Recherche Scientifique). Two main projects were carried out in different fields. The first one that I will discuss is the design of a continuous tunable filter for terahertz two-wire waveguides. The second is the characterization of 2D Transition Metal Dichalcogenides (TMDs) that can work as THz modulators.

The experimental setup is the same as shown in Figure (4.6): a Ti:Sapphire laser (Mai Tai, Spectra Physics, 100 fs, 800 nm, 3 W) was used to generate free carriers in a commercial photoconductive antenna (iPCA, BATOP). The beam was collimated to a 1 mm diameter and 500 mW average power. A function generator (KEYSIGHT 33600A) applied a square 10 mV voltage with a 10 kHz frequency for THz emission. Electro-optic detection was performed using a 1 mm thick ZnTe crystal. To measure the polarized probe beam, free-space balanced amplified photodetectors (PDB 210A) were used and connected to a lock-in amplifier (STANFORD RESEARCH SR860).

4.3.1 Terahertz Continuous Tunable Filter

Future 6G networks and wireless applications are probably a few years away from implementation and are sure to benefit from operation in the 100 GHz to 1 THz frequency bands [75] and therefore the ever-growing demand for high data rates could be achieved. Developing a new series of components, such as modulators, switches, couplers, filters, and multiplexers, that can serve as the fundamental blocks for manipulating THz communication signals [148], is a must.

Inspired by the possibility of surface engineering and optical components for signal processing inside the waveguide [149], the idea of a continuously tunable filter for THz frequencies is proposed. This filter will allow changing the cutoff frequency by only moving one grating that will be held between the two-wire waveguide, as represented in Figure (4.11). By moving this grating up and down, it will be possible to select the desired cutoff frequency.

To fabricate the grating, a 3D printer (ELEGOO Mars 4 Ultra) and ELEGOO Rapid Standard Grey Resin were used.

Figure 4.11: Terahertz continuous tunable filter between two wire waveguide.

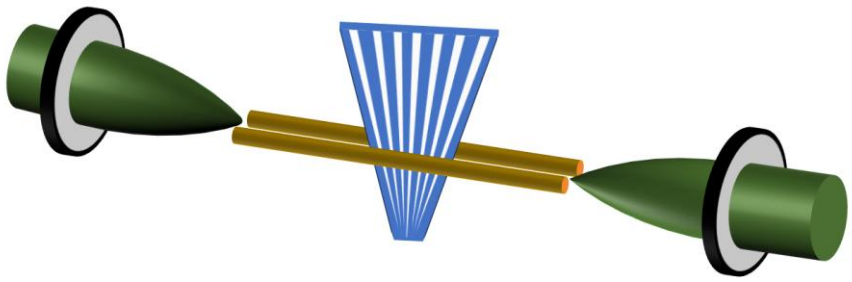

Source: The author (2025)

Once the idea is just to cut off one specific frequency, taking advantage of the Bragg grating is an excellent start. The proposed design consists of a Bragg grating with different Bragg periods, depending on the position of the grating. The idea is quite simple, but increasing the signal to its maximum and making the bandwidth of the reflected frequency as narrow as possible (increasing the Q-factor) is not an easy task. For this purpose, Lumerical software was used to perform simulations and optimize the grating parameters. The first and most important parameter is the refractive index of the grating, which is why one THz-TDS measurement was performed, and the result is shown in Figure (4.12).

Figure 4.12: Complex refractive index measurement of the grey resin from the 3D printer.

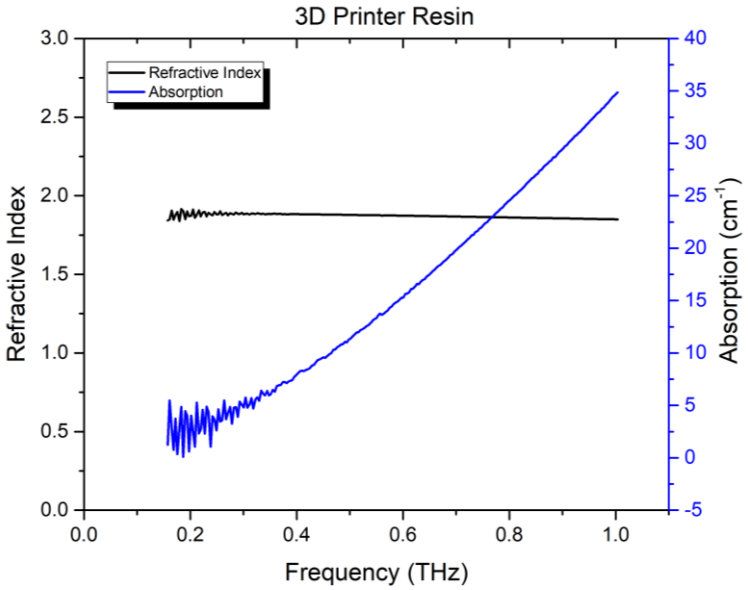

Source: The author (2025)

To perform this measurement, a 1 mm thick wafer was printed and then characterized by using THz-TDS technique. The result shows a linear refractive index n = 1.9. This value was used for all the simulations. The gap distance between the two wires is $g = 300\ \mu m$ for better coupling, as represented in Figure (4.13).

Figure 4.13: Two wire waveguide coupling. (a) the electric field profile, showing the coupling and (b) the transmission through the two-wire waveguide.

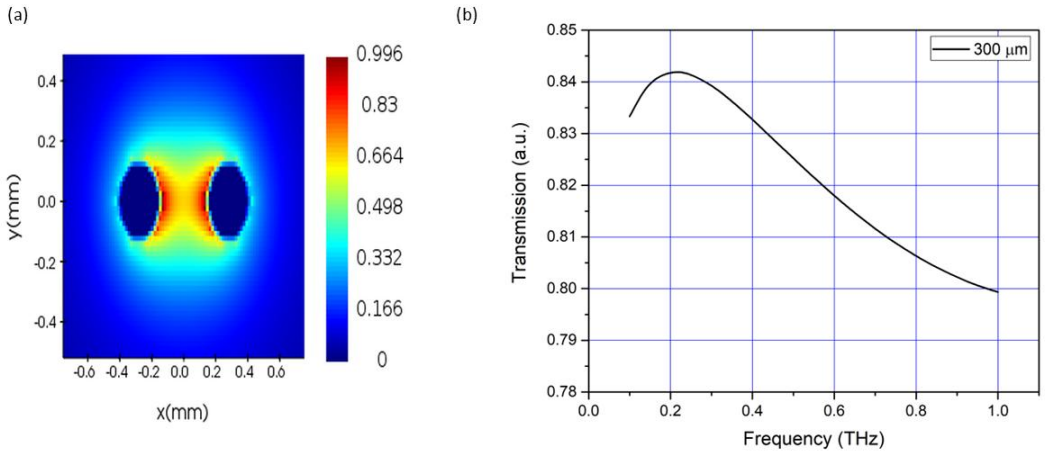

Source: The author (2025)

Once there is a limitation due to the distance between the wires, the thickness of the grating was kept fixed at 100 µm, while the other parameters, such as the length and the Bragg period, were optimized. After some trials, it was shown that 36 gratings were the best configuration for the filter design, leading to 2 cm on one side and 8 mm on the other, and a total length of 4 cm. The grating parameters are reported in Figure (4.14), and the transmitted spectra at different positions are plotted in Figure (4.15).

Figure 4.14: Continuous tunable filter grating parameters

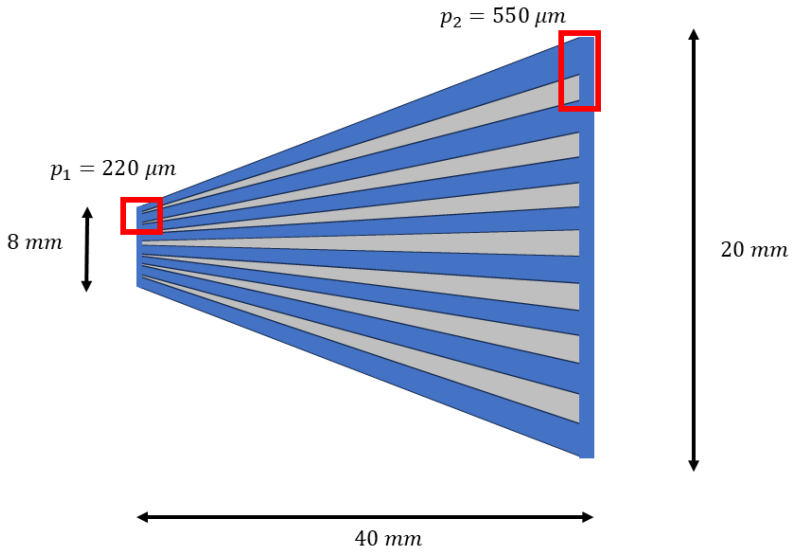

Source: The author (2025)

Figure 4.15: Transmission spectra of the grating in different positions.

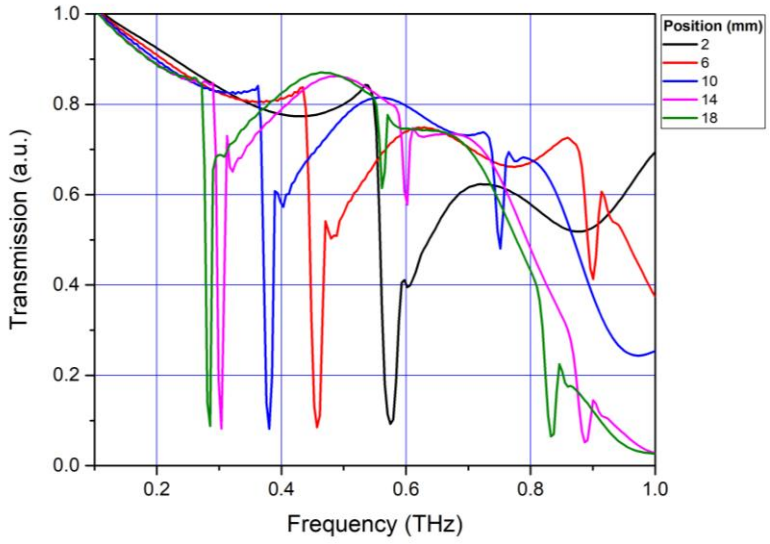

Source: The author (2025)

Figure (4.15) shows the simulations performed by Lumerical. By changing the vertical position of the grating, the transmission spectra will change, and a new different frequency will be cut off. To illustrate this, Figure (4.16) brings the electric field profile at 0.3 THz when the grating is at 14 mm.

Figure 4.16: Electric field profile at 0.3 THz when the grating is positioned at 14 mm.

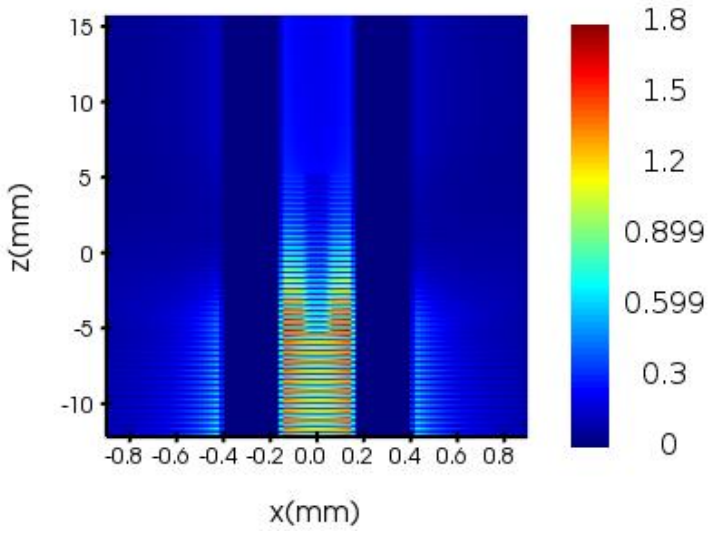

Source: The author (2025)

The electric field profile in Figure (4.16) shows that, when the grating is at the 14 mm position, there is no transmitted signal at 0.3 THz because it is reflected by the grating placed between the two wires. Obviously, there are some concerns about how the grating should be hung between the wires. Thus, the actual printed grating, represented in Figure (4.17), is slightly longer, with an aperture in the middle where a post can be screwed in to hold it steady. Also, to avoid bending, some structures were added between the gratings to prevent it from stretching.

Figure 4.17: Printed grating.

Source: The author (2025)

To perform the measurement after the filter had been optimized, we used two different lenses: a 10 mm lens to focus the beam between the two wires and couple the THz pulse, and a 100 mm lens to collimate the beam after the two wires, which were placed in an acrylic holder. The filter was mounted on a 3-axis stage for better positioning. While the terahertz beam was successfully coupled between the two wires, the limited space made it difficult to position the grating freely. This constraint increased the risk of the sample touching the wires (possibly due to some bending) and losing the coupling. So far, no experimental data has been obtained from this setup. A potential solution to overcome this issue is to increase the gap between the wires, which will be discussed in Chapter 5 (Future Works).

4.3.2 Characterization of 2D Transition Metal Dichalcogenides (TMDs)

Transition Metal Dichalcogenides (TMDs) have a chemical formula of “MX_2”, where "M" is a transition metal and "X" is a chalcogen (excluding oxygen and polonium). Atomically, the transition metal is sandwiched by two chalcogens. The structure MX_2 is called a “layer.” These layers are bonded via Van der Waals forces. The bulk TMD is a set of layers, one on top of the

other. Regarding synthesis, there are a couple of methods to obtain a 2D material from the bulk, including bottom-up approaches, such as Chemical Vapor Deposition (CVD), and top-down methods, like mechanical exfoliation [1].

TMDs are promising materials for optoelectronics due to their tunable bandgap, high carrier mobility, and strong optical response [150]. Thus, the characterization of new 2D materials is a major step toward potentially improving the performance of certain devices. Therefore, this section is designated to presenting new results regarding the characterization of 2D TMDs. The characterized samples are $ZrTe_2$, $NbSe_2$, and MoS_2. Their synthesis follows a bottom-up process called "redox exfoliation" [151]. From this set of samples, there are already studies of MoS_2 in THz frequencies [152–158], which will be important for future comparisons. A literature result [139] of the complex refractive index is expressed in Figure (4.18):

Figure 4.18: THz-TDS measurement of MoS2. a) the comparison signal of reference and sample; b) the real and imaginary part of the complex refractive index.

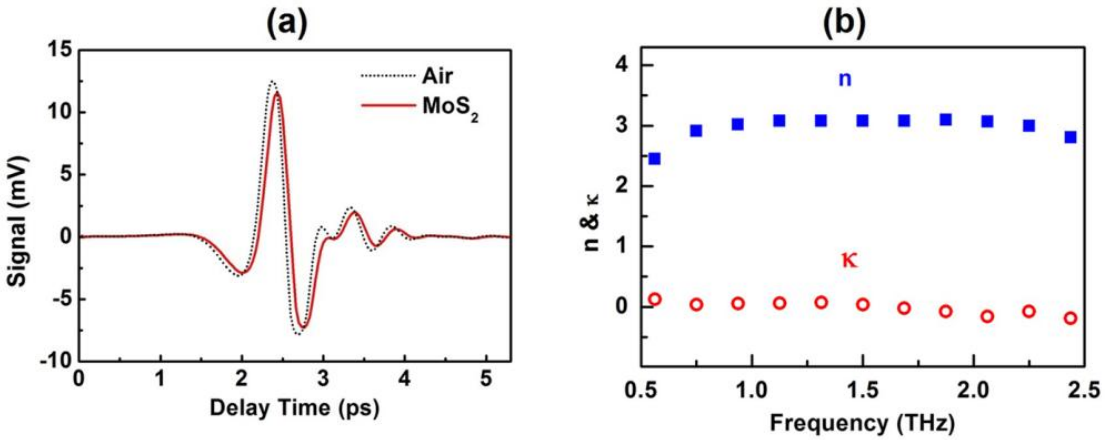

Source: [139]

An important consideration before the measurements themselves is regarding the parameters necessary to solve Equation (4.15). For this purpose, a Python script was coded to use FFT (Fast Fourier Transform) and solve the boundary equations for every sample in question. To obtain the refractive index of the TMDs, the thickness of the deposition and the refractive index of the substrate must be known. All three samples were deposited on high resistivity (> 10 kΩ) 1 mm thick silicon wafers (VIRGINIA SEMICONDUCTORS) by spin coating technique for a uniform deposition. Thus, Scanning Electron Microscopy (SEM) was performed to measure the layer thickness, showing a 35 nm deposition (these results are in Figure 1 in Appendix A).

Regarding the refractive index of silicon, it was already mentioned in Figure (4.8) that this value is around 3.42. Even though this value is well known, we took the opportunity to measure it. Terahertz Time-Domain Spectroscopy was performed to obtain experimental results of the refractive index of the high-resistivity silicon used in the TMDs deposition. The results are shown in Figure (4.19):

Figure 4.19: THz-TDS measurement on silicon wafer. (a) both air (reference) and silicon (sample) signal; (b) the Fourier transformed signal to obtain the frequency dependent spectra; (c) refractive index of the silicon.

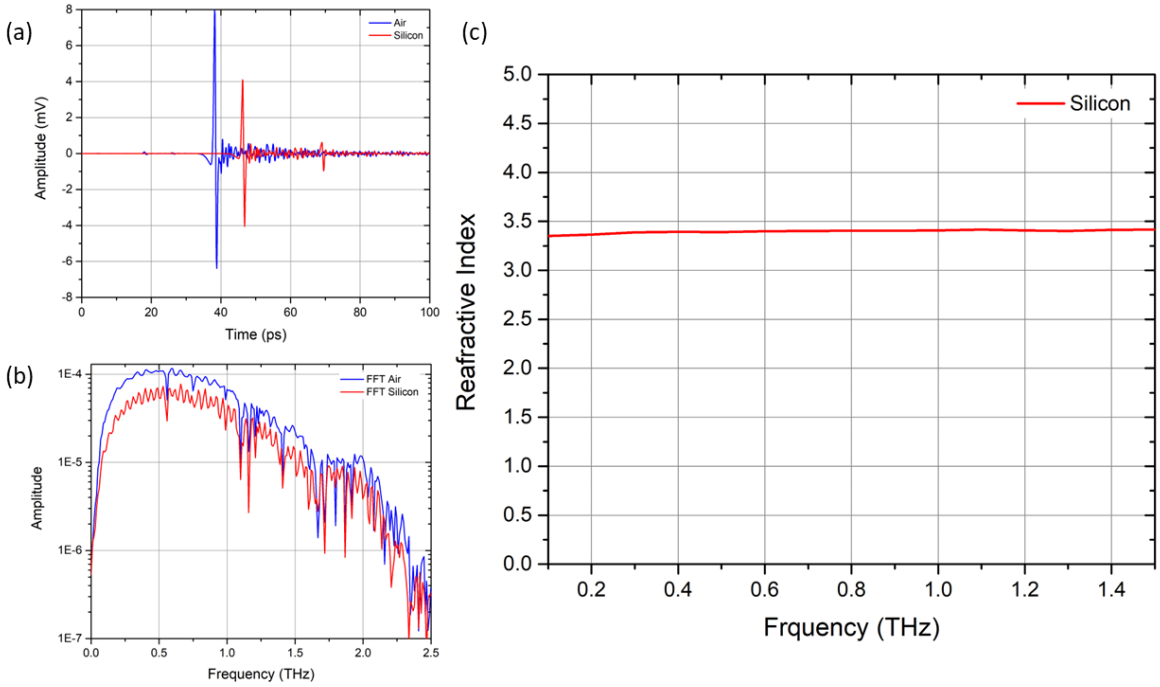

Source: The author (2025)

It's noticeable that there is a delay and a decrease in the amplitude of the THz signal after passing through the silicon wafer, as shown in Figure (4.19a). Since the imaginary part of high-resistivity silicon is close to zero, one possible way to estimate the real part of the refractive index of silicon is, considering that it's frequency independent, measuring the distance between the maximum amplitude of the highest signal and that of the etalon. The etalon is nothing more than a multiple reflection signal after one roundtrip, so the beam propagates through the silicon twice. Therefore, the refractive index will be estimated by only calculating $n = c\Delta t/2l$, where l is the substrate thickness. From the data, one peak is at 46.25 ps while the other is at 69.01 ps. The estimated real part of the refractive index is around 3.414, in agreement with the experimental results.

In possession of the necessary parameters, now it's possible to solve Equation (4.16). One possible simplification is using the thin film approximation [159], leading to:

$$\frac{E_s}{E_{ref}} = \frac{t_{01}P_1t_{12}}{t_{02}P_2}\frac{1}{1-r_{12}r_{01}P_2^2} \quad . \tag{4.20}$$

After solving Equation (4.20), all three samples refractive index are presented in Figure (4.20), where the absorption coefficient is not shown because it is close to zero for all samples (the plot for each sample separately is in Figure 2 on Appendix A).

Figure 4.20: Refractive index of the samples MoS_2, $NbSe_2$ and $ZrTe_2$.

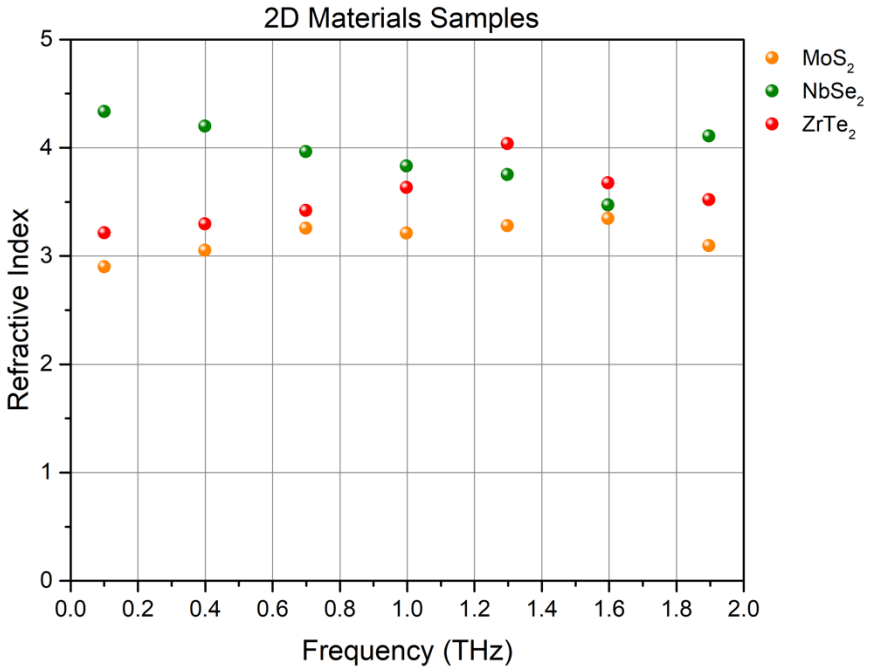

Source: The author (2025)

A single plot of the MoS_2 sample is presented in Figure (4.21). The reason for that is to compare the result obtained experimentally to the one from Figure (4.18). It's evident that both components of the complex refractive index of the MoS_2 agree with the literature, getting a real part close to $n = 3$ and an almost zero absorption coefficient.

Figure 4.21: MoS_2 real and imaginary part of the refractive index.

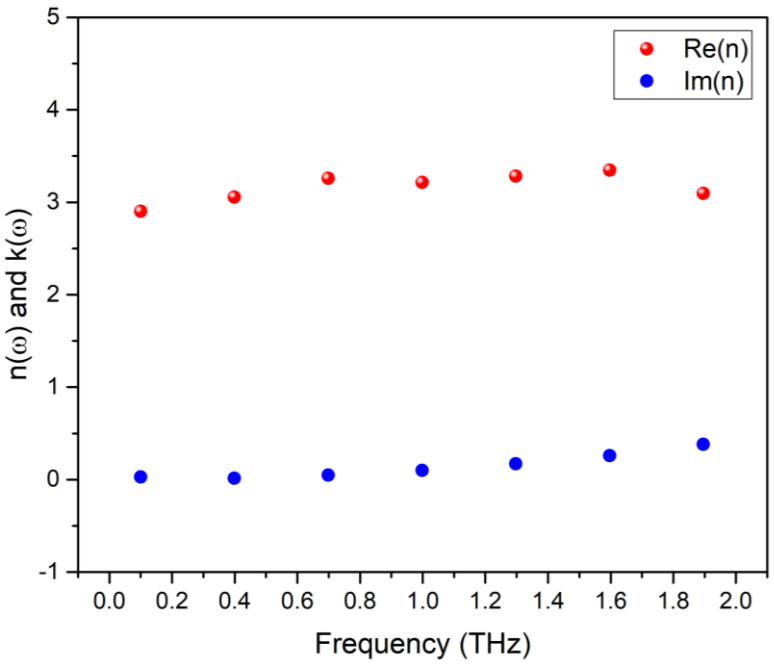

Source: The author (2025)

There are numerous applications for TMDs in electronics, such as transistors, photodetectors, biosensors, and energy [160–164]. Additionally, in the communications field, especially in the THz range, these samples can work as optical THz modulators [157]. Not only MoS2, but also other TMDs such as WSe2, ReSe2, ReS2, and SnS2 have shown this property [165]. Thus, it is of great interest to verify if the samples in question have this property as well. The measurement consists of applying an optical CW pump (Fabry-Perot Laser Diode, FPL808S, 250 mW, 808 nm, Thorlabs) with a spot size larger than the THz beam and measuring its transmission for different pump powers. By applying this external pump, the conductivity of the samples will increase and therefore the transmission of the THz will decrease. Two 35 mm Teflon lenses were used to focus and collimate the THz beam onto the sample, as represented in Figure (4.22). The diameter of the THz beam at the silicon was around 3 mm and the IR beam was around 3.2 mm.

Figure 4.22: Sketch representing the modulation experiment on TMDs.

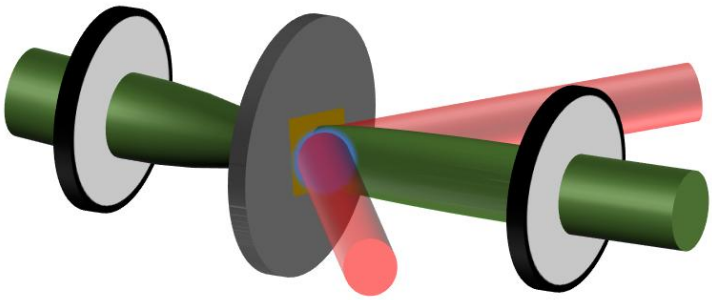

Source: The author (2025)

Calculating the modulation for each sample consists of comparing the transmission of the beam with and without the pump, following the same idea as the OPTP experiment. In contrast, here a CW pump is applied, so there is no interest in the conductivity or the recombination time of the photocarriers. The modulation $M(\omega)$ can be easily obtained by [157]:

$$M(\omega) = \left| \frac{t_i(\omega) - t_0(\omega)}{t_0(\omega)} \right| , \tag{4.21}$$

where t_i and t_0 are the transmission with and without the pump after the Fourie transform. The full spectra of all samples are represented in Figures 3, 4 and 5 in Appendix A. For comparison, choosing one specific frequency (0.7 THz, for example), it's possible to check the modulation depth of each sample compared to the bare silicon, for example. This result is in Figure (4.23).

Figure 4.23: THz modulation result for each of the samples.

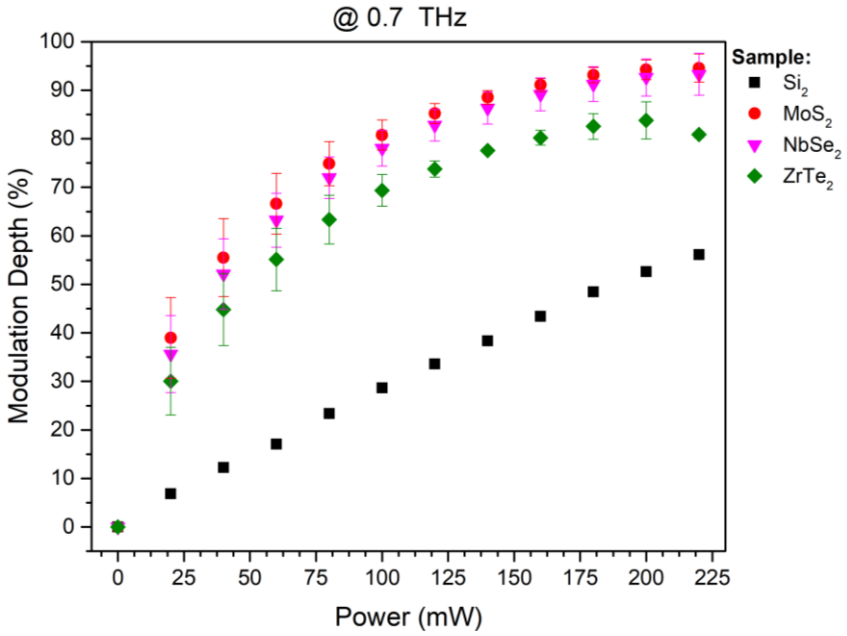

Source: The author (2025)

By applying an external pump, photocarriers will be generated, leading to an increase in conductivity and, therefore, a decrease in transmission. The modulation depth represents how much signal is lost due to the pump. Obviously, increasing the power will increase not only the number of photocarriers but also the modulation depth. High resistivity (HR) silicon shows this property, as represented by the plot in Figure (4.23). More importantly, when the samples are deposited, there is an increase in the modulation depth, reaching almost 100% for MoS_2 and $NbSe_2$. One possible explanation is that TMDs have the ability to catalyze HR silicon to aggregate more electrons at the interface, resulting in better modulation performance. Electrons and holes generated in HR silicon would recombine in HR silicon. However, TMDs on the surface of the HR silicon could capture electrons to reduce the concentration of electrons in HR silicon, which could reduce the rate of recombination. Therefore, more free carriers could exist in HR silicon to provide higher photoconductivity, which could lower the transmission of the THz wave [165].

4.4 CONCLUSION

Terahertz (THz) techniques have emerged as transformative tools in modern science, bridging the gap between microwave and infrared technologies. Their ability to penetrate

various materials while remaining non-ionizing makes them invaluable for applications in spectroscopy, imaging, and wireless communication. From biomedical diagnostics and security screening to next-generation electronics and fundamental physics, THz technology continues to unlock new possibilities across multiple disciplines.

In this study, we successfully characterized a set of 2D Transition Metal Dichalcogenides (TMDs) using THz Time-Domain Spectroscopy (THz-TDS) and obtained their refractive indices. Additionally, modulation measurements demonstrated that these materials have the potential to function as THz modulators for future applications.

Another promising result is the design of a continuously tunable THz filter in a two-wire waveguide system. While it has yet to be experimentally characterized, our findings suggest that this filter could serve as an efficient tool for signal processing in the THz frequency range. These results contribute to the growing field of THz science and highlight the potential of TMDs and waveguide-based components in shaping future THz technologies. As research in this field progresses, continued advancements will further expand the applications and impact of THz techniques in both fundamental science and industry.

5 FUTURE WORKS

The next step for these measurements is to perform the pump-probe experiment, which is already aligned at INRS. To do this, we need to change the substrate to quartz, since silicon is not transparent at 800 nm. Before coming back to Brazil, I took some measurements to obtain the refractive index of quartz for future work, as demonstrated in Figure (5.1). The idea is to have a more comprehensive result, presenting the photoconductivity and the characteristics of each sample. Also, in collaboration with the Air Force Laboratory (USA), other TMDs could be characterized. Besides, another deposition could be made with a thicker layer of sample to compare the results.

Figure 5.1: Characterization of quartz slit for OPTP experiment.

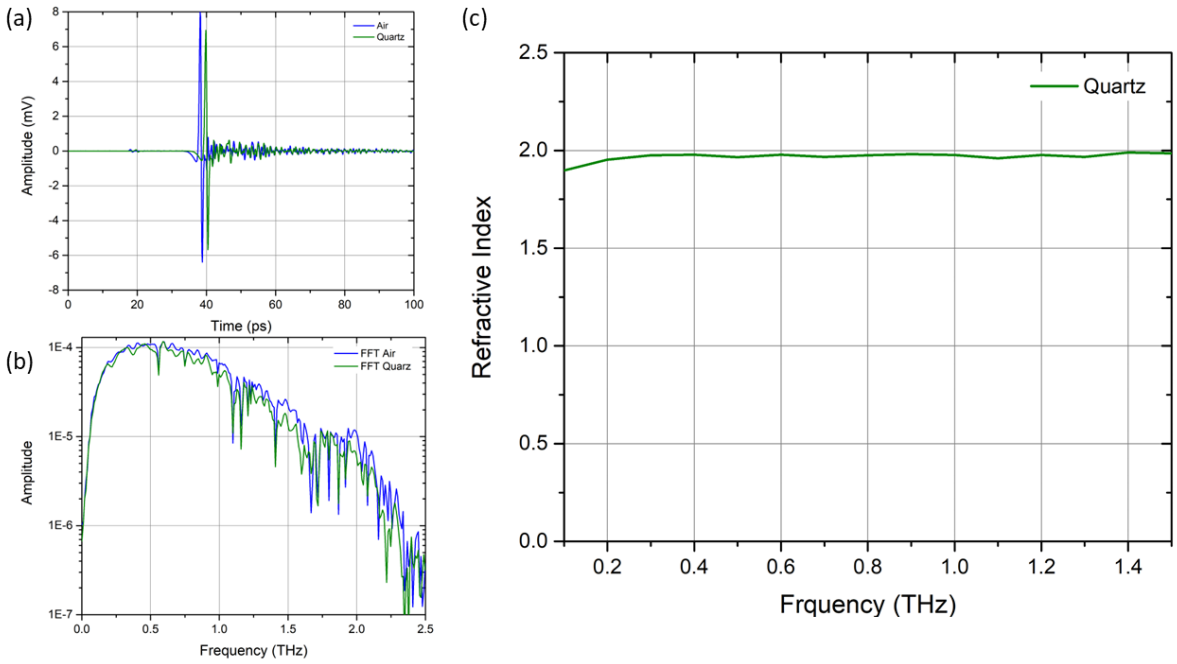

Source: The author (2025)

Also, I want to perform the continuous tunable filter experiment using a 500 µm gap between the two wires. There were some limitations due to the distance between the wires for inserting the grating and placing it correctly. Therefore, by increasing the distance between the wires, we will have more freedom to position it. I performed some simulations to check the transmission of the THz pulse under this configuration, and we still have some signal coupled between the wires, as represented in Figure (5.2). So, it might be possible to achieve a good

result. Although, there will be some changes and modifications to the grating parameters to optimize the signal.

Figure 5.2: Comparison between two-wire waveguides with 300 µm and 500 µm gap. (a) the electric field profile of 300 µm (above) and 500 µm (below), and (b) transmission of the signal in both configurations.

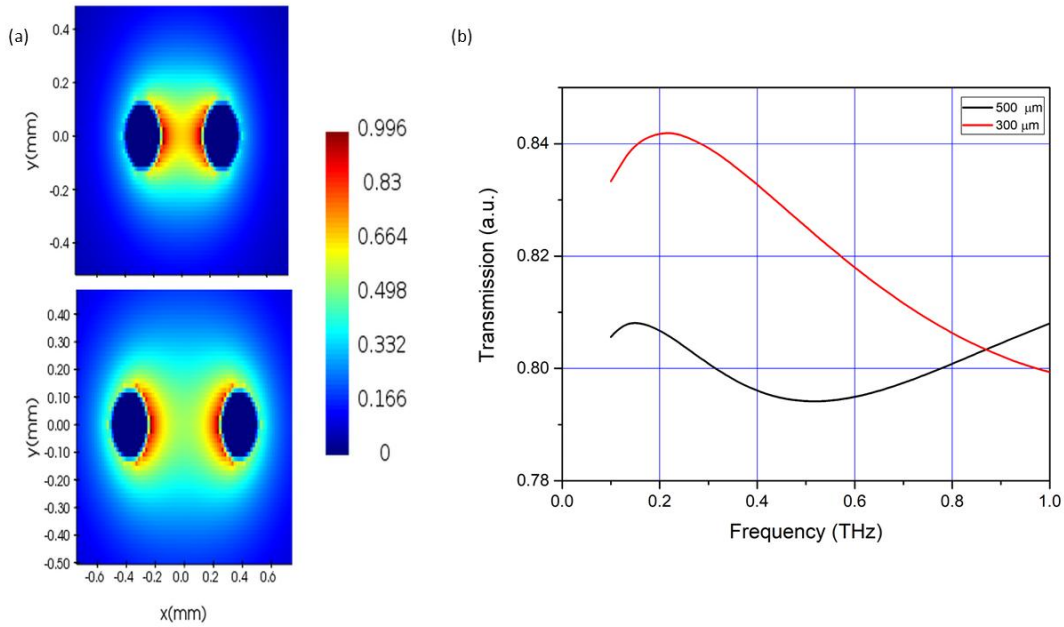

REFERENCES

[1] X. Cai, Y. Luo, B. Liu, and H. M. Cheng, *Preparation of 2D Material Dispersions and Their Applications*, Chemical Society Reviews.

[2] S. M. Dadfar, K. Roemhild, N. I. Drude, S. von Stillfried, R. Knüchel, F. Kiessling, and T. Lammers, *Iron Oxide Nanoparticles: Diagnostic, Therapeutic and Theranostic Applications*, Advanced Drug Delivery Reviews.

[3] A. G. Ricciardulli and P. W. M. Blom, *Solution-Processable 2D Materials Applied in Light-Emitting Diodes and Solar Cells*, Advanced Materials Technologies.

[4] G. A. Naikoo et al., *2D Materials, Synthesis, Characterization and Toxicity: A Critical Review*, Chemico-Biological Interactions.

[5] S. J. Ikhmayies, *Characterization of Nanomaterials*, JOM.

[6] P. Beard, *Biomedical Photoacoustic Imaging*, Interface Focus.

[7] S. Jeon, J. Kim, D. Lee, J. W. Baik, and C. Kim, *Review on Practical Photoacoustic Microscopy*, Photoacoustics.

[8] J. Neu and C. A. Schmuttenmaer, Tutorial: An introduction to terahertz time domain spectroscopy (THz-TDS), J Appl Phys **124**, (2018).

[9] K. H. Song and L. V. Wang, *Deep Reflection-Mode Photoacoustic Imaging of Internal Organs*, in *Photons Plus Ultrasound: Imaging and Sensing 2008: The Ninth Conference on Biomedical Thermoacoustics, Optoacoustics, and Acousto-Optics*, Vol. 6856 (SPIE, 2008), p. 68561W.

[10] P. K. Upputuri and M. Pramanik, Photoacoustic imaging in the second near-infrared window: a review, J Biomed Opt **24**, 1 (2019).

[11] K. Nishizawa, T. Maruyama, M. Takayama, M. Okada, J.-I. Hachiya, and Y. Furuya, Determinations of Organ Doses and Effective Dose Equivalents from Computed Tomographic Examination, 1991.

[12] D. J. Brenner, E. J. Hall, and D. Phil, Computed Tomography-An Increasing Source of Radiation Exposure, 2007.

[13] L. V. Wang and S. Hu, *Photoacoustic Tomography: In Vivo Imaging from Organelles to Organs*, Science.

[14] D. M. Mittleman, Twenty years of terahertz imaging, Opt Express **26**, 9417 (2018).

[15] X. Li, J. Li, Y. Li, A. Ozcan, and M. Jarrahi, *High-Throughput Terahertz Imaging: Progress and Challenges*, Light: Science and Applications.

[16] J. Dong, P. You, A. Tomasino, A. Yurtsever, and R. Morandotti, Single-shot ultrafast terahertz photography, Nat Commun **14**, (2023).

[17] A. Rosencwaig, PHOTOACOUSTIC SPECTROSCOPY, 1980.

[18] J. P. Gordon, H. J. Zeiger, and C. H. Townes, The Maser New Type of Microwave Ampli6er, Frequency Standard, and Spectrometer*f, Physical Review **99**, (1955).

[19] A. L. Schawlow and A. C. H. Townes, Infrared and Optical Masers, Physical Review **112**, (1958).

[20] A. Crocker, H. A. Gebbie, M. F. Kimmitt, and L. E. S. Mathias, Stimulated Emission in the Far Infra-red, Nature **201**, 250 (1964).

[21] W. Kaiser and C. G. B. Garrett, TWO-PHOTON EXCITATION IN CaF2:Eu2+, Phys Rev Lett **7**, (1961).

[22] M. Göppert-Mayer, Elementary processes with two quantum transitions, Annalen Der Physik (Leipzig) **18**, 466 (2009).

[23] J. D. Jackson, *Classical Eletrodynamics*, 3rd ed., Vol. 1999 (John Wiley & Sons, Inc., 2001).

[24] A. G. Bell, On the Production and Reproduction of Sound by Light, American Journal Science **XX**, 305 (1880).

[25] Action o f an Intermittent Beam 307 III. " Action of an Interm Ittent Beam of Radiant H Eat upon Gaseous Matter." B y J o h n T y n d a l l, n.d.

[26] W. C. Rontgen, Ueber Tone, welche durch intermittirende Bestrahlung eines Gases entschen, (n.d.).

[27] S. Manohar and D. Razansky, Photoacoustics: a historical review, Adv Opt Photonics **8**, 586 (2016).

[28] A. Rosencwaig and A. Gersho, Theory of the photoacoustic effect with solids, J Appl Phys **47**, 64 (1976).

[29] A. C. M. V. P. Pereira, Espectroscopia Não Linear e Geração de Imagem Fotoacústica Com Nanopartículas de Nitreto de Titânio, Universidade Federal de Pernambuco, 2021.

[30] L. V. Wang, Tutorial on photoacoustic microscopy and computed tomography, IEEE Journal on Selected Topics in Quantum Electronics **14**, 171 (2008).

[31] L. V. Wang and J. Yao, *A Practical Guide to Photoacoustic Tomography in the Life Sciences*, Nature Methods.

[32] J. G. Parker, Optical Absorption in Glass: Investigation Using an Acoustic Technique, n.d.

[33] Reports Nitric Oxide Air Pollution: Detection by Optoacoustic Spectroscopy, n.d.

[34] D. A. BERLINCOURT, D. R. CURRAN, and H. JAFFE, *Piezoelectric and Piezomagnetic Materials and Their Function in Transducers*, in *Physical Acoustics* (Elsevier, 1964), pp. 169–270.

[35] Y. Bae, J. J. Song, and Y. B. Kim, Photoacoustic Detection of Nanosecond-Pulse-Induced Optical Absorption in Solids, 1982.

[36] A. Hordvik and H. Schlossberg, Photoacoustic Technique for Determining Optical Absorption Coefficients in Solids, n.d.

[37] M. Xu and L. V. Wang, *Photoacoustic Imaging in Biomedicine*, Review of Scientific Instruments.

[38] A. Rosencwaig, PHOTOACOUSTIC SPECTROSCOPY OF SOLIDS, 1973.

[39] A. Rosencwaig and E. Pines, A PHOTOACOUSTIC STUDY OF NEWBORN RAT STRATUM CORNEUM, 1977.

[40] A. A. Oraevsky, S. L. Jacques, and F. K. Tittel, Measurement of Tissue Optical Properties by Time-Resolved Detection of Laser-Induced Transient Stress, 1997.

[41] A. A. Oraevsky, E. V. Savateeva, S. V. Solomatin, A. A. Karabutov, V. G. Andreev, Z. Gatalica, T. Khamapirad, and P. M. Henrichs, *<title>Optoacoustic Imaging of Blood for Visualization and Diagnostics of Breast Cancer</Title>*, in *Biomedical Optoacoustics III*, Vol. 4618 (SPIE, 2002), pp. 81–94.

[42] G. Ku, X. Wang, G. Stoica, and L. V. Wang, Multiple-bandwidth photoacoustic tomography, Phys Med Biol **49**, 1329 (2004).

[43] G. Ku and L. V Wang, Deeply Penetrating Photoacoustic Tomography in Biological Tissues Enhanced with an Optical Contrast Agent, 2005.

[44] A. Greco, M. Mancini, S. Gargiulo, M. Gramanzini, P. P. Claudio, A. Brunetti, and M. Salvatore, *Ultrasound Biomicroscopy in Small Animal Research: Applications in Molecular and Preclinical Imaging*, Journal of Biomedicine and Biotechnology.

[45] P. K. Upputuri and M. Pramanik, Photoacoustic imaging in the second near-infrared window: a review, J Biomed Opt **24**, 1 (2019).

[46] G. Busse and A. Rosencwaig, Subsurface imaging with photoacoustics, Appl Phys Lett **36**, 815 (1980).

[47] Y. H. Wong, R. L. Thomas, and G. F. Hawkins, Surface and subsurface structure of solids by laser photoacoustic spectroscopy, Appl Phys Lett **32**, 538 (1978).

[48] A. Rosencwaig, Thermal wave microscopy with photoacoustics, J Appl Phys **51**, 2210 (1980).

[49] R. J. Von Gutfeld and R. L. Melcher, 20-MHz acoustic waves from pulsed thermoelastic expansions of constrained surfaces, Appl Phys Lett **30**, 257 (1977).

[50] G. Busse, Optoacoustic phase angle measurement for probing a metal, Appl Phys Lett **35**, 759 (1979).

[51] Y. H. Wong, R. L. Thomas, and J. J. Pouch, Subsurface structures of solids by scanning photoacoustic microscopy, Appl Phys Lett **35**, 368 (1979).

[52] R. L. Thomas, J. J. Pouch, Y. H. Wong, L. D. Favro, P. K. Kuo, and A. Rosencwaig, Subsurface flaw detection in metals by photoacoustic microscopya, J Appl Phys **51**, 1152 (1980).

[53] H. K. Wickramasinghe, R. C. Bray, V. Jipson, C. F. Quate, and J. R. Salcedo, Photoacoustics on a microscopic scale, Appl Phys Lett **33**, 923 (1978).

[54] M. Luukkala and A. Penttinen, Photoacoustic Microscope, Electron Lett **15**, (1979).

[55] C. Zhang, K. Maslov, and L. V Wang, Subwavelength-Resolution Label-Free Photoacoustic Microscopy of Optical Absorption in Vivo, n.d.

[56] A. Das, A. C. M. V. Pereira, A. A. Popov, A. Pastukhov, S. M. Klimentov, A. V. Kabashin, and A. S. L. Gomes, Plasmonically enhanced two-photon absorption induced photoacoustic microscopy with laser-synthesized TiN nanoparticles, Appl Phys Lett **121**, (2022).

[57] M. E. Maldonado, A. Das, A. M. Jawaid, A. J. Ritter, R. A. Vaia, and A. S. L. Gomes, Optical and Photoacoustic Z-Scan in 2D Layered Transition Metal Dichalcogenides, n.d.

[58] D. J. de Aberasturi, A. B. Serrano-Montes, and L. M. Liz-Marzán, Modern Applications of Plasmonic Nanoparticles: From Energy to Health, Adv Opt Mater **3**, 602 (2015).

[59] P. K. Jain, K. S. Lee, I. H. El-Sayed, and M. A. El-Sayed, Calculated absorption and scattering properties of gold nanoparticles of different size, shape, and composition: Applications in biological imaging and biomedicine, Journal of Physical Chemistry B **110**, 7238 (2006).

[60] J. Olson, S. Dominguez-Medina, A. Hoggard, L. Y. Wang, W. S. Chang, and S. Link, *Optical Characterization of Single Plasmonic Nanoparticles*, Chemical Society Reviews.

[61] D. Jaque, C. Richard, B. Viana, K. Soga, X. Liu, and J. García Solé, Inorganic nanoparticles for optical bioimaging, Adv Opt Photonics **8**, 1 (2016).

[62] A. Lalisse, G. Tessier, J. Plain, and G. Baffou, Quantifying the Efficiency of Plasmonic Materials for Near-Field Enhancement and Photothermal Conversion, Journal of Physical Chemistry C **119**, 25518 (2015).

[63] T. de L. Pedrosa, G. M. F. de Oliveira, A. C. M. V. Pereira, M. J. B. da S. Crispim, L. A. da Silva, M. S. da Silva, I. A. de Souza, A. M. M. de A. Melo, A. S. L. Gomes, and R. E. de Araujo, Tailoring Plasmonic Nanoheaters Size for Enhanced Theranostic Agent Performance, Bioengineering **11**, (2024).

[64] S. Jiang, J. Lin, and P. Huang, *Nanomaterials for NIR-II Photoacoustic Imaging*, Advanced Healthcare Materials.

[65] T. Lee, H. W. Baac, Q. Li, and L. J. Guo, *Efficient Photoacoustic Conversion in Optical Nanomaterials and Composites*, Advanced Optical Materials.

[66] V. T. C. Tsang, X. Li, and T. T. W. Wong, *A Review of Endogenous and Exogenous Contrast Agents Used in Photoacoustic Tomography with Different Sensing Configurations*, Sensors (Switzerland).

[67] Y. Sheng, L. De Liao, N. Thakor, and M. C. Tan, Rare-earth doped particles as dual-modality contrast agent for minimally-invasive luminescence and dual-wavelength photoacoustic imaging, Sci Rep **4**, (2014).

[68] Y. Sheng, L. De Liao, A. Bandla, Y. H. Liu, J. Yuan, N. Thakor, and M. C. Tan, Enhanced near-infrared photoacoustic imaging of silica-coated rare-earth doped nanoparticles, Materials Science and Engineering C **70**, 340 (2017).

[69] A. C. M. V. Pereira, R. S. Pugina, A. Das, K. d. Lima, L. F. dos Santos, R. R. Gonçalves, and A. S. L. Gomes, *Er3+-Yb3+ Co-Doped Nanoparticles as Contrast Agents for near Infrared Biomedical Photoacoustic Imaging Application*, in (SPIE-Intl Soc Optical Eng, 2023), p. 25.

[70] Q. Fu, R. Zhu, J. Song, H. Yang, and X. Chen, *Photoacoustic Imaging: Contrast Agents and Their Biomedical Applications*, Advanced Materials.

[71] C. Lee, M. Jeon, and C. Kim, *Photoacoustic Imaging in Nanomedicine*, in *Applications of Nanoscience in Photomedicine* (Elsevier Inc., 2015), pp. 31–47.

[72] L. Sen Lin, Z. X. Cong, J. B. Cao, K. M. Ke, Q. L. Peng, J. Gao, H. H. Yang, G. Liu, and X. Chen, Multifunctional Fe3O4@polydopamine core-shell nanocomposites for intracellular mRNA detection and imaging-guided photothermal therapy, ACS Nano **8**, 3876 (2014).

[73] G. N. da S. A. O. Rocha, J. Y. R. Silva, D. K. D. do N. Santos, A. C. M. V. Pereira, J. V. R. Rocha, C. dos S. C. Alves, J. R. G. da S. Almeida, A. S. L. Gomes, A. F. Bakuzis, and S. A. Junior, Design of a magnetic nanocarrier containing phyllacanthone as delivery of anticancer phytochemical: Characterization and theranostic in vitro applications, J Alloys Compd **1010**, (2025).

[74] A. N. Standard, American National Standard for Safe Use of Lasers, n.d.

[75] T. S. Rappaport, Y. Xing, O. Kanhere, S. Ju, A. Madanayake, S. Mandal, A. Alkhateeb, and G. C. Trichopoulos, Wireless communications and applications above 100 GHz: Opportunities and challenges for 6g and beyond, IEEE Access **7**, 78729 (2019).

[76] A. Hadni, A SHORT HISTORY OF 50 YEARS OF RESEARCH IN THE FAR INFRARED: 1952-2002, 2003.

[77] W. Ghann and J. Uddin, *Terahertz (THz) Spectroscopy: A Cutting-Edge Technology*, in *Terahertz Spectroscopy - A Cutting Edge Technology* (InTech, 2017).

[78] W. Herschel, Experiments on the Refrangibility of invisible Rays of the Sun, Royal Society 284 (1800).

[79] H. Rubens and Benj. W. Snow, II. On the refraction of rays of great wave-length in rock-salt, sylvite, and fluorite , The London, Edinburgh, and Dublin Philosophical Magazine and Journal of Science **35**, 35 (1893).

[80] M. F. Kimmitt, Restrahlen to T-Rays-100 Years of Terahertz Radiation, 2003.

[81] A. G. Arkadiewa, Short Electromagnetic Waves of wave-length up to 82 Microns, Nature **113**, 640 (1924).

[82] E. F. Nichols and J. D. Tear, SHORT ELECTRIC WAVES, n.d.

[83] S. P. Langley, The Bolometer, Nature 14 (1881).

[84] M. J. E. Golay, A pneumatic infra-red detector, Review of Scientific Instruments **18**, 357 (1947).

[85] S. J. Fray and J. F. C. Oliver, Photoconductive Detector of Radiation of Wavelength Greater than 50 u, Macdonald and Co. Ltd, 1959.

[86] F. J. Low, Low-Temperature Germanium Bolometer, 1961.

[87] T. Y. Chang and T. J. Bridges, Laser action at 452, 496 and 541 um in optically pumped CH3F, Optics Communication **1**, 423 (1970).

[88] T. S. Hartwick, D. T. Hodges, D. H. Barker, and F. B. Foote, Far Infrared Imagery, n.d.

[89] P. U. Jepsen, D. G. Cooke, and M. Koch, Terahertz spectroscopy and imaging - Modern techniques and applications, Laser Photon Rev **5**, 124 (2011).

[90] M. Lu, J. Shen, N. Li, Y. Zhang, C. Zhang, L. Liang, and X. Xu, Detection and identification of illicit drugs using terahertz imaging, J Appl Phys **100**, (2006).

[91] J. F. Federici, B. Schulkin, F. Huang, D. Gary, R. Barat, F. Oliveira, and D. Zimdars, *THz Imaging and Sensing for Security Applications - Explosives, Weapons and Drugs*, Semiconductor Science and Technology.

[92] A. G. Davies, A. D. Burnett, W. Fan, E. H. Linfield, and J. E. Cunningham, Terahertz Spectroscopy of Explosives and Drugs Open Access under CC BY-NC-ND License, 2008.

[93] N. Nagai, R. Kumazawa, and R. Fukasawa, Direct evidence of inter-molecular vibrations by THz spectroscopy, Chem Phys Lett **413**, 495 (2005).

[94] C. Yu, S. Fan, Y. Sun, and E. Pickwell-Macpherson, The potential of terahertz imaging for cancer diagnosis: A review of investigations to date., Quant Imaging Med Surg **2**, 33 (2012).

[95] R. M. Woodward, V. P. Wallace, R. J. Pye, B. E. Cole, D. D. Arnone, E. H. Lin¢eld, and M. Pepper, Terahertz Pulse Imaging of Ex Vivo Basal Cell Carcinoma, 2003.

[96] S. J. Park, S. H. Cha, G. A. Shin, and Y. H. Ahn, Sensing viruses using terahertz nano-gap metamaterials, Biomed Opt Express **8**, 3551 (2017).

[97] S. J. Park, J. T. Hong, S. J. Choi, H. S. Kim, W. K. Park, S. T. Han, J. Y. Park, S. Lee, D. S. Kim, and Y. H. Ahn, Detection of microorganisms using terahertz metamaterials, Sci Rep **4**, (2014).

[98] B. Yu, F. Zeng, Y. Yang, Q. Xing, A. Chechin, X. Xin, I. Zeylikovich, and R. R. Alfano, Torsional Vibrational Modes of Tryptophan Studied by Terahertz Time-Domain Spectroscopy, Biophys J **86**, 1649 (2004).

[99] M. R. C. Williams, A. B. True, A. F. Izmaylov, T. A. French, K. Schroeck, and C. A. Schmuttenmaer, Terahertz spectroscopy of enantiopure and racemic polycrystalline valine, Physical Chemistry Chemical Physics **13**, 11719 (2011).

[100] J. Neu, C. T. Nemes, K. P. Regan, M. R. C. Williams, and C. A. Schmuttenmaer, Exploring the solid state phase transition in dl-norvaline with terahertz spectroscopy, Physical Chemistry Chemical Physics **20**, 276 (2017).

[101] T. M. Korter, R. Balu, M. B. Campbell, M. C. Beard, S. K. Gregurick, and E. J. Heilweil, Terahertz spectroscopy of solid serine and cysteine, Chem Phys Lett **418**, 65 (2006).

[102] M. D. King, P. M. Hakey, and T. M. Korter, Discrimination of chiral solids: A terahertz spectroscopic investigation of L- and DL-serine, Journal of Physical Chemistry A **114**, 2945 (2010).

[103] K. Kamburoglu, N. O. Yetimôglu, and H. Altan, Characterization of primary and permanent teeth using terahertz spectroscopy, Dentomaxillofacial Radiology **43**, (2014).

[104] N. P. Yadav, G. Z. Hu, Z. P. Yao, and A. Kumar, Diagnosis of Dental Caries Using Terahertz Technology, Journal of Electronic Science and Technology **19**, 255 (2021).

[105] J. Cai et al., Dental caries diagnosis using terahertz spectroscopy and birefringence, Opt Express **30**, 13134 (2022).

[106] C. Longbottom, D. Craw1ey, B. C. D. Arnonec, and V. Wallacec, Potential Uses of Terahertz Pulse Imaging in Dentistry: Caries and Erosion Detection, 2002.

[107] C. P. Da Silva, R. T. F. Costa, A. C. M. V. Pereira, J. M. de L. Gomes, A. S. L. Gomes, S. L. D. Moraes, and D. S. Lopes, *Applicability of Terahertz Spectroscopy in Dentistry: A Scoping Review*, Oral Surgery, Oral Medicine, Oral Pathology and Oral Radiology.

[108] I. F. Akyildiz, J. M. Jornet, and C. Han, Terahertz band: Next frontier for wireless communications, Physical Communication **12**, 16 (2014).

[109] S. Dang, O. Amin, B. Shihada, and M. S. Alouini, What should 6G be?, Nat Electron **3**, 20 (2020).

[110] W. Saad, M. Bennis, and M. Chen, A Vision of 6G Wireless Systems: Applications, Trends, Technologies, and Open Research Problems, IEEE Netw **34**, 134 (2020).

[111] K. Reimann, Table-top sources of ultrashort THz pulses, Reports on Progress in Physics **70**, 1597 (2007).

[112] D. H. Auston, Picosecond optoelectronic switching and gating in silicon, Appl Phys Lett **26**, 101 (1975).

[113] M. Bass, P. A. Franken, J. F. Ward, and G. Weinreich, OPTICAL RECTIFICATION, Phys Rev Lett **9**, (1962).

[114] F. Zernike and P. R. Bermanf, GENERATION OF FAR INFRARED AS A DIFFERENCE FREQUENCY, **15**, 999 (1965).

[115] R. Boyd, *Nonlinear Optics*, 3rd ed. (2007).

[116] G. P. Williams, P. Weightman, A. Doria, Y. Shen, D. M. Mittleman, M. Towrie, and H. Roskos, High-power terahertz synchrotron sources, Philosophical Transactions of the Royal Society A: Mathematical, Physical and Engineering Sciences **362**, 403 (2004).

[117] J. M. Byrd, W. P. Leemans, A. Loftsdottir, B. Marcelis, M. C. Martin, W. R. McKinney, F. Sannibale, T. Scarvie, and C. Steier, Observation of Broadband Self-Amplified Spontaneous Coherent Terahertz Synchrotron Radiation in a Storage Ring, Phys Rev Lett **89**, (2002).

[118] L. R. Elias, J. Hu, and G. Ramian, The UCSB electrostatic accelerator free electron laser: first operation, Nuclear Instruments and Methods in Physics Research **A237**, 203 (1985).

[119] R. Kohler, A. Tredicucci, F. Beltram, H. E. Beere, E. H. Linfield, A. G. Favies, D. A. Ritchie, R. C. Iotti, and F. Rossi, Terahertz Semiconductor-heterostructure laser, **417**, 156 (2002).

[120] R. Ulbricht, E. Hendry, J. Shan, T. F. Heinz, and M. Bonn, Carrier dynamics in semiconductors studied with time-resolved terahertz spectroscopy, Rev Mod Phys **83**, 543 (2011).

[121] W. C. Michels and N. L. Curtis, A pentode lock-in amplifier of high frequency selectivity, Review of Scientific Instruments **12**, 444 (1941).

[122] A. Nahata, D. H. Auston, T. F. Heinz, and C. Wu, Coherent detection of freely propagating terahertz radiation by electro-optic sampling, Appl Phys Lett **68**, 150 (1996).

[123] Y. Cai, I. Brener, J. Lopata, J. Wynn, L. Pfeiffer, J. B. Stark, Q. Wu, X. C. Zhang, and J. F. Federici, *Coherent Terahertz Radiation Detection: Direct Comparison between Free-Space Electro-Optic Sampling and Antenna Detection*, Applied Physics Letters.

[124] C. Winnewisser, P. Uhd Jepsen, M. Schall, V. Schyja, and H. Helm, Electro-optic detection of THz radiation in LiTaO3, LiNbO3 and ZnTe, Appl Phys Lett **70**, 3069 (1997).

[125] Q. Wu and X. C. Zhang, Free-space electro-optic sampling of terahertz beams, Appl Phys Lett **67**, 3523 (1995).

[126] R. Ulbricht, E. Hendry, J. Shan, T. F. Heinz, and M. Bonn, Carrier dynamics in semiconductors studied with time-resolved terahertz spectroscopy, Rev Mod Phys **83**, 543 (2011).

[127] D. G. Allis, D. A. Prokhorova, and T. M. Korter, Solid-state modeling of the terahertz spectrum of the high explosive HMX, Journal of Physical Chemistry A **110**, 1951 (2006).

[128] M. R. Leahy-Hoppa, M. J. Fitch, X. Zheng, L. M. Hayden, and R. Osiander, Wideband terahertz spectroscopy of explosives, Chem Phys Lett **434**, 227 (2007).

[129] Y. C. Sim, I. Maeng, and J. H. Son, Frequency-dependent characteristics of terahertz radiation on the enamel and dentin of human tooth, Current Applied Physics **9**, 946 (2009).

[130] A. Redo-Sanchez, G. Salvatella, R. Galceran, E. Roldós, J. A. García-Reguero, M. Castellari, and J. Tejada, Assessment of terahertz spectroscopy to detect antibiotic residues in food and feed matrices, Analyst **136**, 1733 (2011).

[131] Y. Hua and H. Zhang, Qualitative and quantitative detection of pesticides with terahertz time-domain spectroscopy, IEEE Trans Microw Theory Tech **58**, 2064 (2010).

[132] L. I. Jiusheng, Optical Parameters of Vegetable Oil Studied by Terahertz Time-Domain Spectroscopy, n.d.

[133] P. U. Jepsen, U. Møller, and H. Merbold, Investigation of Aqueous Alcohol and Sugar Solutions with Reflection Terahertz Time-Domain Spectroscopy, 2007.

[134] S. Dash and A. Patnaik, Impact of silicon-based substrates on graphene THz antenna, Physica E Low Dimens Syst Nanostruct **126**, (2021).

[135] J. Dai, J. Zhang, W. Zhang, and D. Grischkowsky, Terahertz Time-Domain Spectroscopy Characterization of the Far-Infrared Absorption and Index of Refraction of High-Resistivity, Float-Zone Silicon, 2004.

[136] H. Liu, J. Lu, H. F. Teoh, D. Li, Y. P. Feng, S. H. Tang, C. H. Sow, and X. Zhang, Defect engineering in CdSxSe1-x nanobelts: An insight into carrier relaxation dynamics via optical pump-terahertz probe spectroscopy, Journal of Physical Chemistry C **116**, 26036 (2012).

[137] J. Lu and H. Liu, A critical review on the carrier dynamics in 2D layered materials investigated using THz spectroscopy, Opt Commun **406**, 24 (2018).

[138] E. Knoesel, M. Bonn, J. Shan, F. Wang, and T. F. Heinz, Conductivity of solvated electrons in hexane investigated with terahertz time-domain spectroscopy, Journal of Chemical Physics **121**, 394 (2004).

[139] S. Kar, Y. Su, R. R. Nair, and A. K. Sood, Probing Photoexcited Carriers in a Few-Layer MoS2 Laminate by Time-Resolved Optical Pump-Terahertz Probe Spectroscopy, ACS Nano **9**, 12004 (2015).

[140] S. F. Shi, T. T. Tang, B. Zeng, L. Ju, Q. Zhou, A. Zettl, and F. Wang, Controlling graphene ultrafast hot carrier response from metal-like to semiconductor-like by electrostatic gating, Nano Lett **14**, 1578 (2014).

[141] J. N. Heyman, J. D. Stein, Z. S. Kaminski, A. R. Banman, A. M. Massari, and J. T. Robinson, Carrier heating and negative photoconductivity in graphene, J Appl Phys **117**, (2015).

[142] G. Jnawali, Y. Rao, H. Yan, and T. F. Heinz, Observation of a transient decrease in terahertz conductivity of single-layer graphene induced by ultrafast optical excitation, Nano Lett **13**, 524 (2013).

[143] A. K. Azad, R. P. Prasankumar, D. Talbayev, A. J. Taylor, R. D. Averitt, J. M. O. Zide, H. Lu, A. C. Gossard, and J. F. O'Hara, Carrier dynamics in InGaAs with embedded ErAs nanoislands, Appl Phys Lett **93**, (2008).

[144] J. Zielbauer and M. Wegener, Ultrafast optical pump THz-probe spectroscopy on silicon, Appl Phys Lett **68**, 1223 (1996).

[145] H. W. Liu, L. M. Wong, S. J. Wang, S. H. Tang, and X. H. Zhang, Ultrafast insulator-metal phase transition in vanadium dioxide studied using optical pump-terahertz probe spectroscopy, Journal of Physics Condensed Matter **24**, (2012).

[146] C. A. Schmuttenmaer, Exploring dynamics in the far-infrared with terahertz spectroscopy, Chem Rev **104**, 1759 (2004).

[147] H. J. Joyce, P. Parkinson, N. Jiang, C. J. Docherty, Q. Gao, H. H. Tan, C. Jagadish, L. M. Herz, and M. B. Johnston, Electron mobilities approaching bulk limits in "surface-free" GaAs nanowires, Nano Lett **14**, 5989 (2014).

[148] M. Ghazialsharif, J. Dong, A. Abbes, and R. Morandotti, *Broadband Terahertz Metal-Wire Signal Processors: A Review*, Photonics.

[149] J. Dong et al., Versatile metal-wire waveguides for broadband terahertz signal processing and multiplexing, Nat Commun **13**, (2022).

[150] Z. Shi, H. Zhang, K. Khan, R. Cao, Y. Zhang, C. Ma, A. K. Tareen, Y. Jiang, M. Jin, and H. Zhang, *Two-Dimensional Materials toward Terahertz Optoelectronic Device Applications*, Journal of Photochemistry and Photobiology C: Photochemistry Reviews.

[151] A. Jawaid, J. Che, L. F. Drummy, J. Bultman, A. Waite, M. S. Hsiao, and R. A. Vaia, Redox Exfoliation of Layered Transition Metal Dichalcogenides, ACS Nano **11**, 635 (2017).

[152] J. H. Strait, P. Nene, and F. Rana, High intrinsic mobility and ultrafast carrier dynamics in multilayer metal-dichalcogenide MoS2, Phys Rev B Condens Matter Mater Phys **90**, (2014).

[153] A. Singh, A. Nivedan, S. Kumar, M. Tondusson, J. Degert, J. Oberle, S. J. Yun, Y. H. Lee, and E. Freysz, *THz Conductivity and Photo-Induced Carrier Dynamics in a Graphene, MoS, Graphene Heterostructure*, in *International Conference on Infrared, Millimeter, and Terahertz Waves, IRMMW-THz*, Vols. 2020-November (IEEE Computer Society, 2020), pp. 476–477.

[154] J. H. Buss, R. P. Smith, G. Coslovich, and R. A. Kaindl, *Broadband Transient THz Conductivity of the Transition-Metal Dichalcogenide MoS 2* , in *Ultrafast Phenomena and Nanophotonics XIX*, Vol. 9361 (SPIE, 2015), p. 93611J.

[155] B. Radisavljevic, A. Radenovic, J. Brivio, V. Giacometti, and A. Kis, Single-layer MoS2 transistors, Nat Nanotechnol **6**, 147 (2011).

[156] B. Sapkota, W. Liang, A. VahidMohammadi, R. Karnik, A. Noy, and M. Wanunu, High permeability sub-nanometre sieve composite MoS2 membranes, Nat Commun **11**, (2020).

[157] Y. Cao, S. Gan, Z. Geng, J. Liu, Y. Yang, Q. Bao, and H. Chen, Optically tuned terahertz modulator based on annealed multilayer MoS2, Sci Rep **6**, (2016).

[158] F. Cai, Z. Kou, and Y. Li, THz Broadband Absorber Based on MoS2 with Split Rings and Archimedean Spiral Structures, Symmetry (Basel) **14**, (2022).

[159] J. Neu, K. P. Regan, J. R. Swierk, and C. A. Schmuttenmaer, Applicability of the thin-film approximation in terahertz photoconductivity measurements, Appl Phys Lett **113**, (2018).

[160] Z. Li and S. L. Wong, Functionalization of 2D transition metal dichalcogenides for biomedical applications, Materials Science and Engineering C **70**, 1095 (2017).

[161] K. F. Mak and J. Shan, *Photonics and Optoelectronics of 2D Semiconductor Transition Metal Dichalcogenides*, Nature Photonics.

[162] R. Kurapati, K. Kostarelos, M. Prato, and A. Bianco, *Biomedical Uses for 2D Materials Beyond Graphene: Current Advances and Challenges Ahead*, Advanced Materials.

[163] W. Choi, N. Choudhary, G. H. Han, J. Park, D. Akinwande, and Y. H. Lee, *Recent Development of Two-Dimensional Transition Metal Dichalcogenides and Their Applications*, Materials Today.

[164] B. Radisavljevic, A. Radenovic, J. Brivio, V. Giacometti, and A. Kis, Single-layer MoS2 transistors, Nat Nanotechnol **6**, 147 (2011).

[165] Z. Fan, Z. Geng, W. Fang, X. Lv, Y. Su, S. Wang, J. Liu, and H. Chen, Characteristics of transition metal dichalcogenides in optical pumped modulator of terahertz wave, AIP Adv **10**, (2020).

APPENDIX A

Figure 1: SEM measurements for MoS_2, $NbSe_2$ and $ZrTe_2$ to determine the thickness of the layered sample.

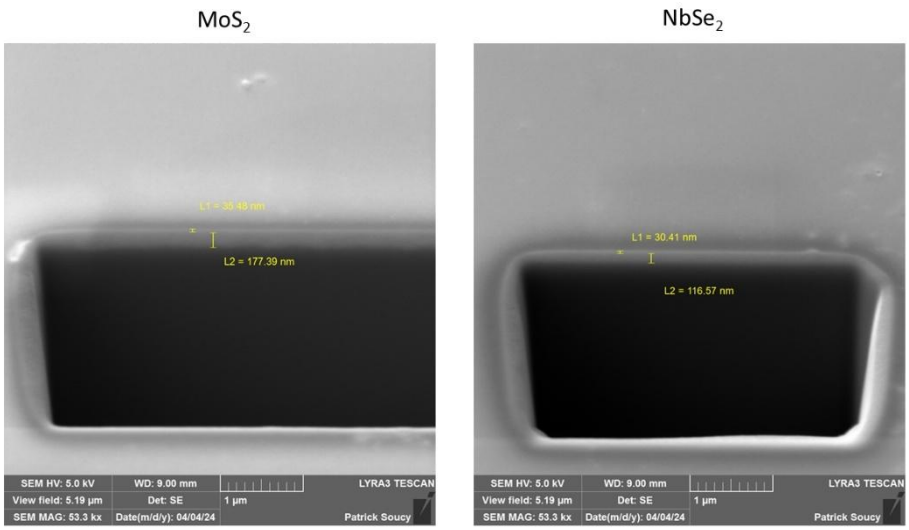

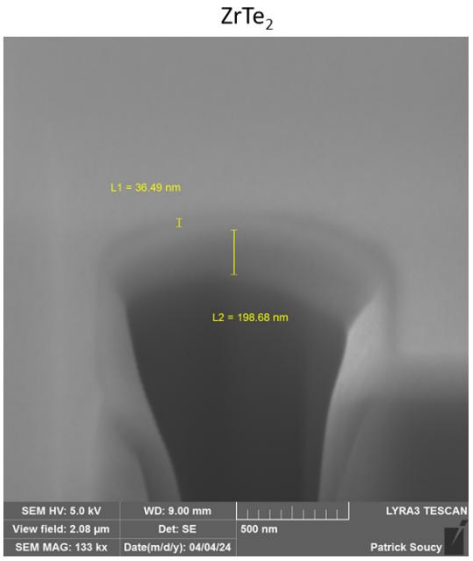

Figure 2: Complex refractive index for all the three samples studied.

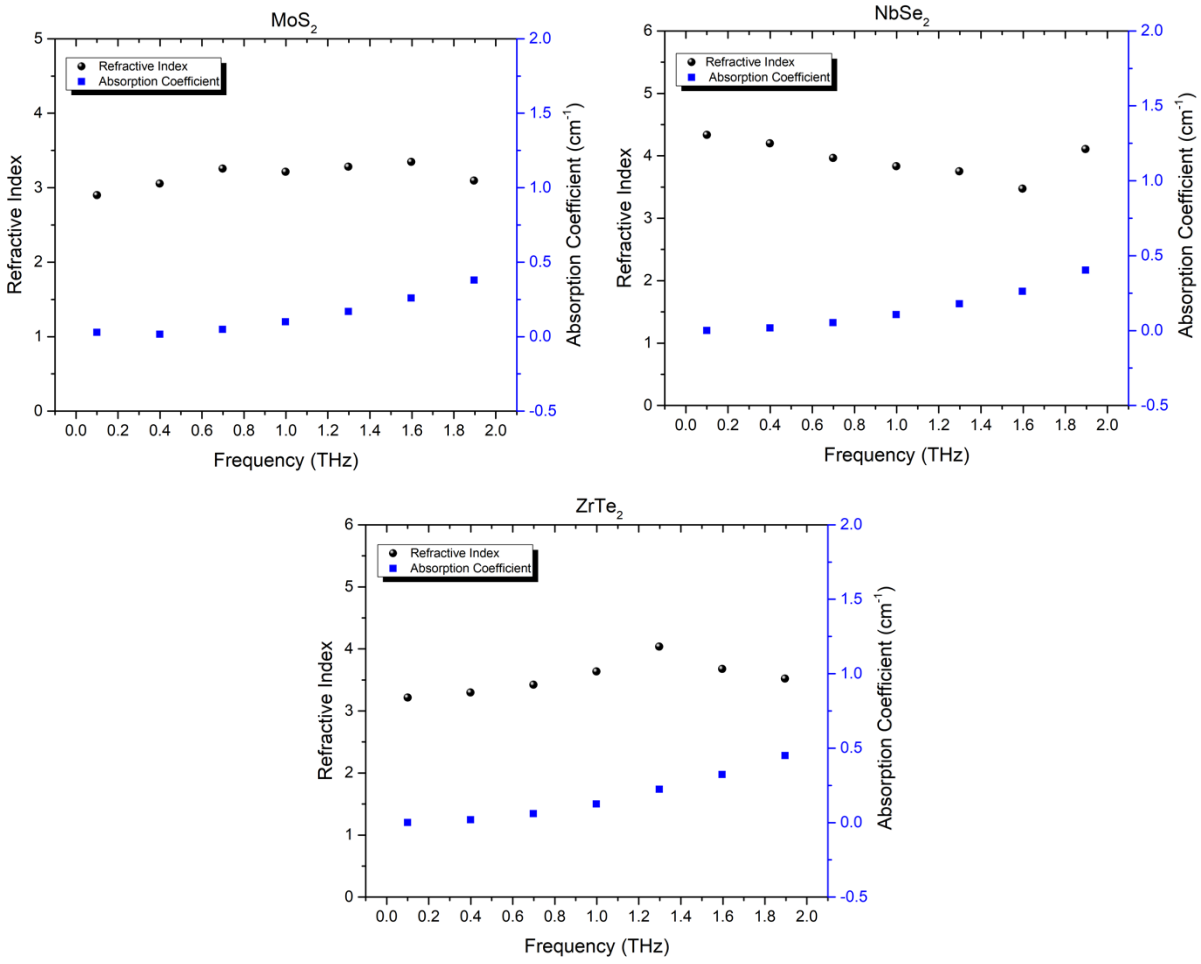

Source: The author (2025)

Figure 3: Transmission and modulation measurements for MoS_2 in different positions.

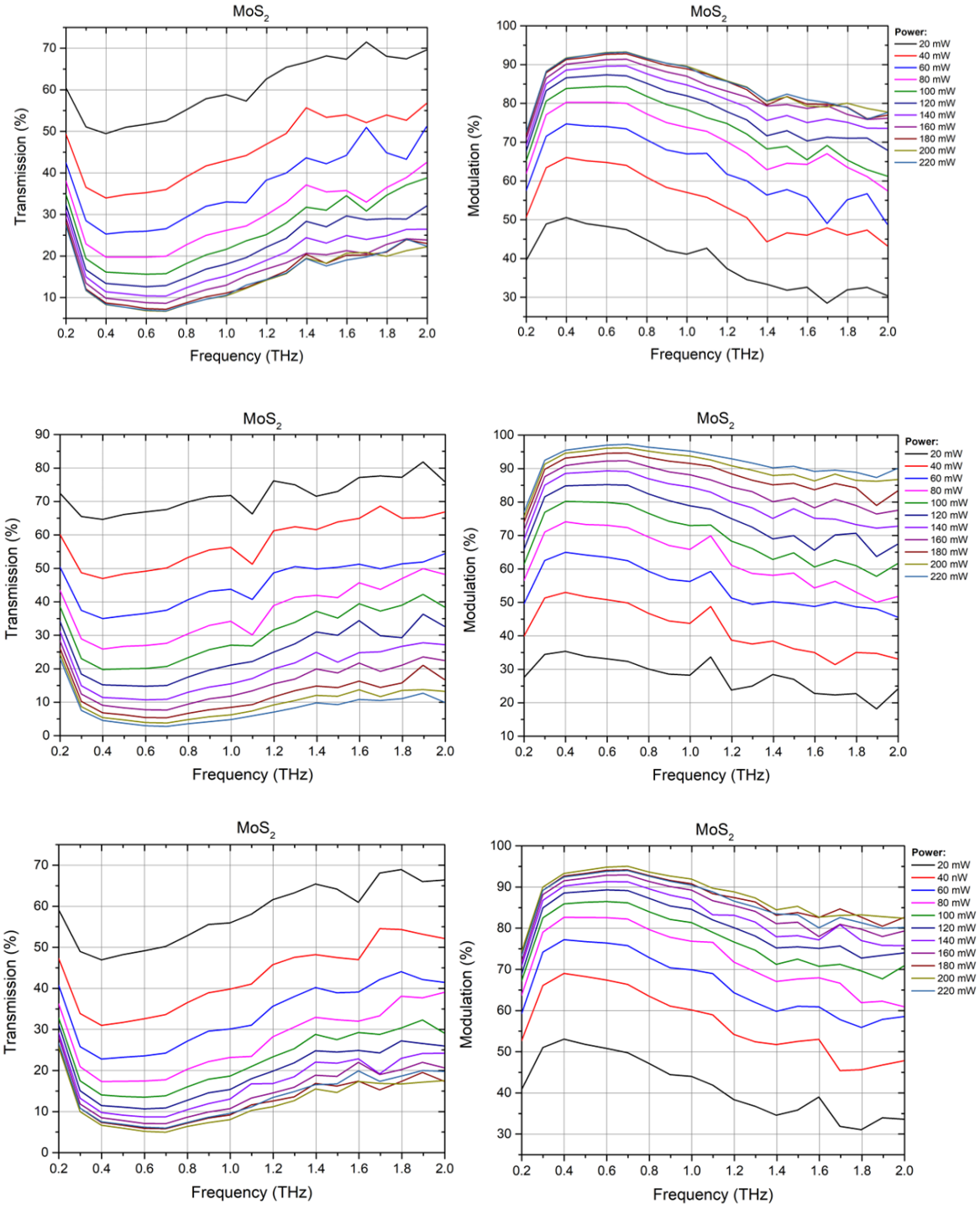

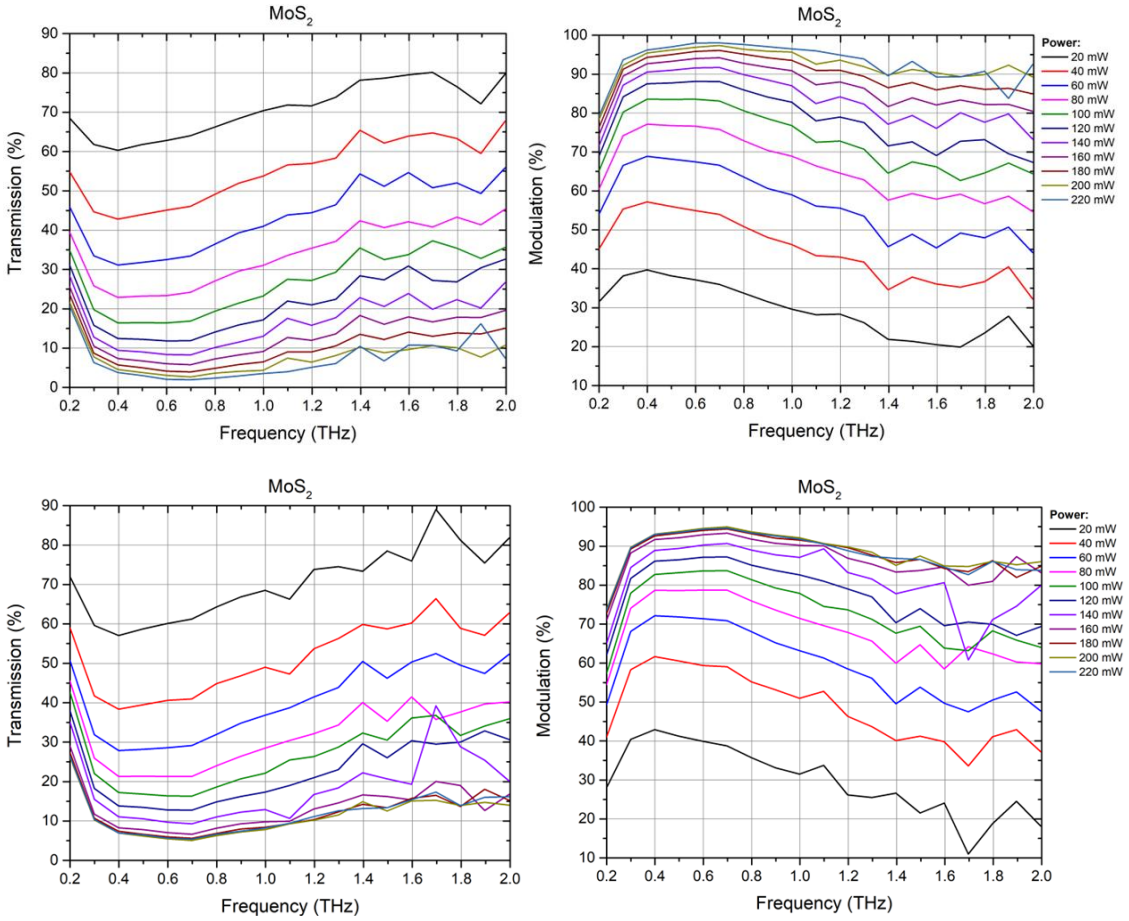

Figure 4: Transmission and modulation measurements for $NbSe_2$ in different positions.

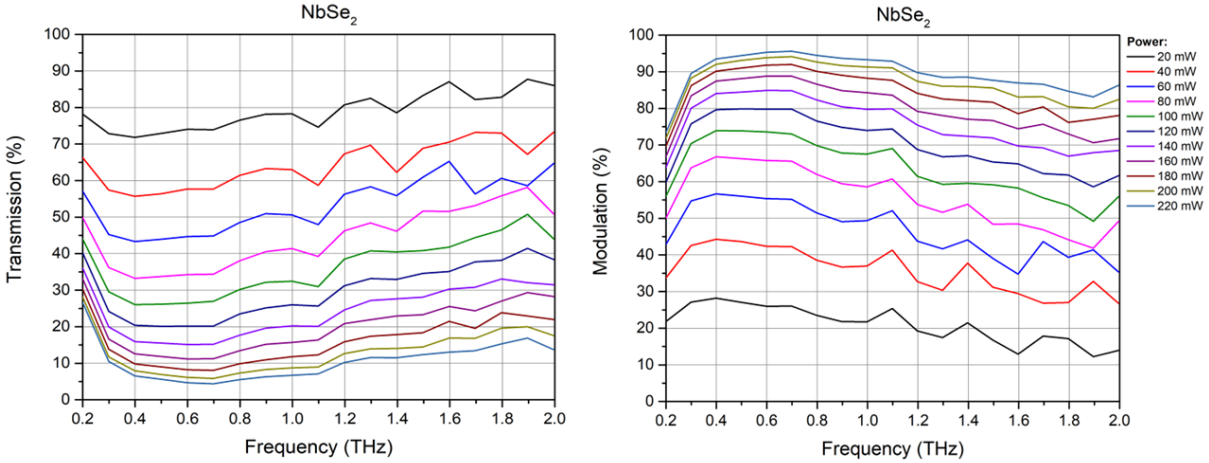

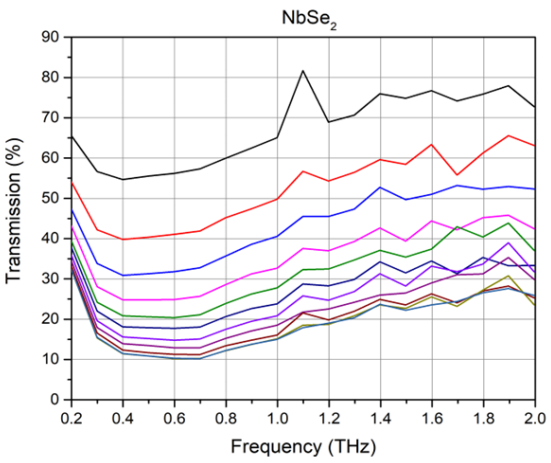
NbSe2
Transmission (%)
Frequency (THz)

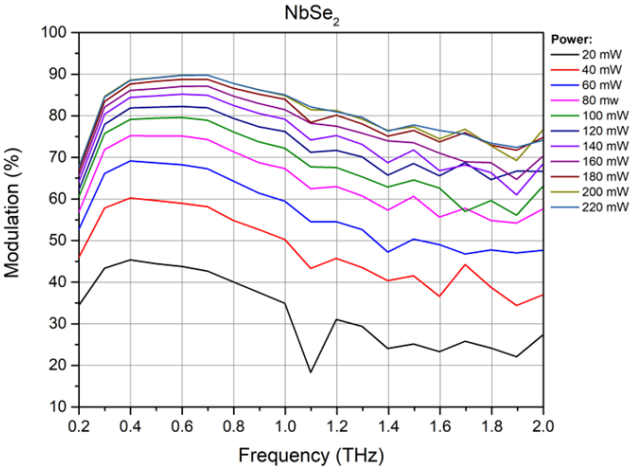
NbSe2
Modulation (%)
Frequency (THz)
Power:
20 mW
40 mW
60 mW
80 mw
100 mW
120 mW
140 mW
160 mW
180 mW
200 mW
220 mW

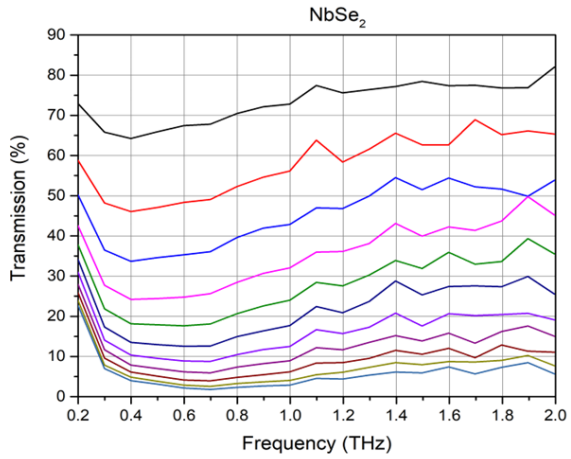
NbSe2
Transmission (%)
Frequency (THz)

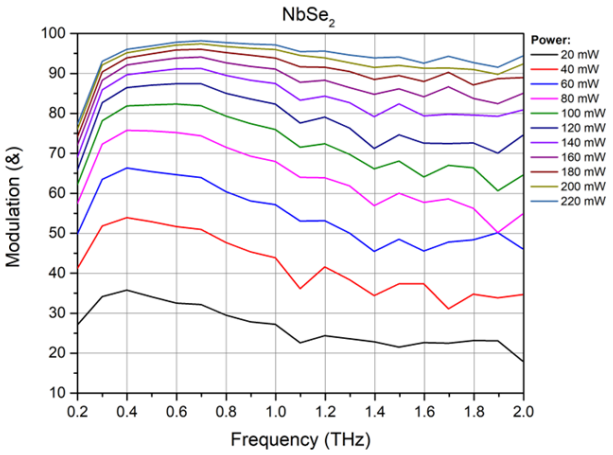
NbSe2
Modulation (&)
Frequency (THz)
Power:
20 mW
40 mW
60 mW
80 mW
100 mW
120 mW
140 mW
160 mW
180 mW
200 mW
220 mW

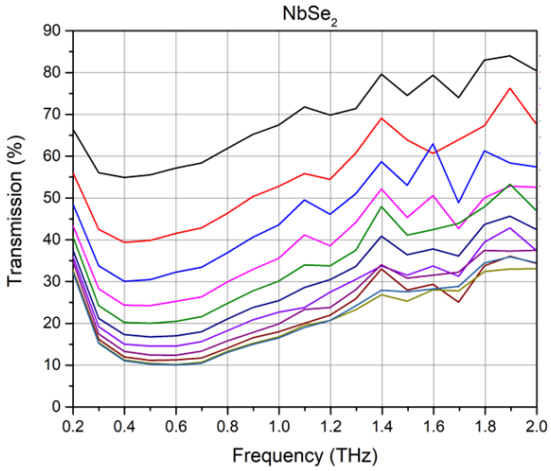
NbSe2
Transmission (%)
Frequency (THz)

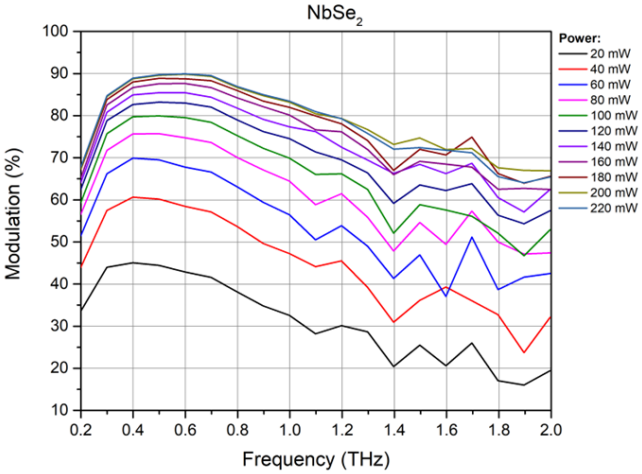
NbSe2
Modulation (%)
Frequency (THz)
Power:
20 mW
40 mW
60 mW
80 mW
100 mW
120 mW
140 mW
160 mW
180 mW
200 mW
220 mW

Figure 5: Transmission and modulation measurements for $ZrTe_2$ in different positions.

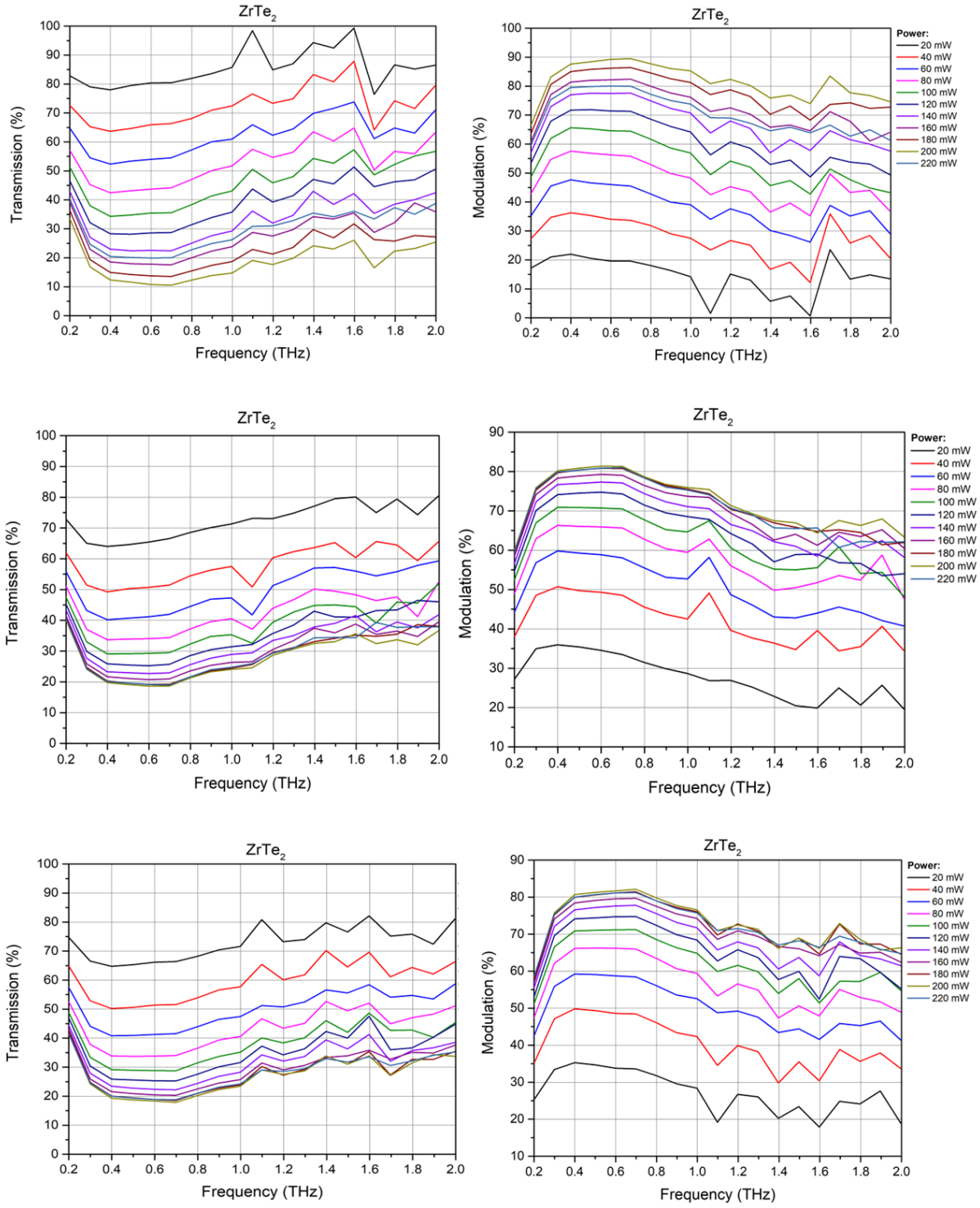

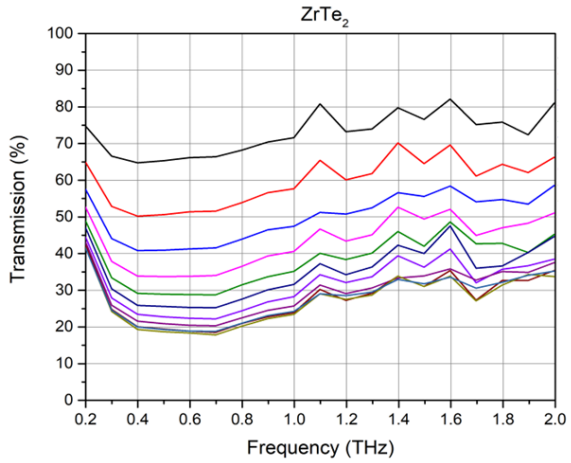
ZrTe2
Transmission (%)
Frequency (THz)

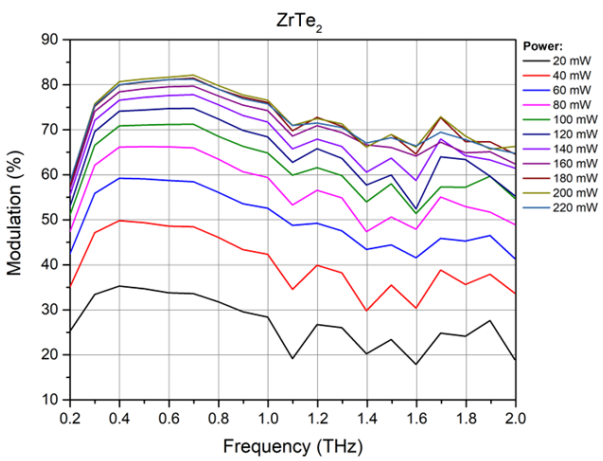
ZrTe2
Modulation (%)
Frequency (THz)
Power:
20 mW
40 mW
60 mW
80 mW
100 mW
120 mW
140 mW
160 mW
180 mW
200 mW
220 mW

APPENDIX B

[1] A. Das, A. C. M. V. Pereira, A. A. Popov, A. Pastukhov, S. M. Klimentov, A. V. Kabashin, and A. S. L. Gomes, Plasmonically enhanced two-photon absorption induced photoacoustic microscopy with laser-synthesized TiN nanoparticles, Appl Phys Lett **121**, (2022).

Applied Physics Letters ARTICLE scitation.org/journal/apl

Plasmonically enhanced two-photon absorption induced photoacoustic microscopy with laser-synthesized TiN nanoparticles

Cite as: Appl. Phys. Lett. **121**, 083701 (2022); doi: 10.1063/5.0101658
Submitted: 2 June 2022 · Accepted: 5 August 2022 ·
Published Online: 25 August 2022

Avishek Das,[1] Arthur C. M. V. Pereira,[1] Anton A. Popov,[2] Andrei Pastukhov,[3] Sergei M. Klimentov,[2] Andrei V. Kabashin,[3,a)] and Anderson S. L. Gomes[1,2,a)]

AFFILIATIONS

[1]Departamento de Física, Universidade Federal de Pernambuco, Recife 50670-901, Pernambuco, Brazil
[2]MEPhI, Institute of Engineering Physics for Biomedicine (PhysBio), 31 Kashirskoe sh., 115409 Moscow, Russia
[3]Aix Marseille University, CNRS, LP3, 163 Ave. De Luminy, Case 917, 13288 Marseille, France

[a)]Authors to whom correspondence should be addressed: anderson.lgomes@ufpe.br and andrei.kabashin@univ-amu.fr

[2] A. C. M. V. Pereira, R. S. Pugina, A. Das, K. d. Lima, L. F. dos Santos, R. R. Gonçalves, and A. S. L. Gomes, *Er3+-Yb3+ Co-Doped Nanoparticles as Contrast Agents for near Infrared Biomedical Photoacoustic Imaging Application*, in (SPIE-Intl Soc Optical Eng, 2023), p. 25.

Er^{3+}-Yb^{3+} co-doped nanoparticles as contrast agents for near infrared biomedical photoacoustic imaging application

Arthur C. M. V. Pereira[a], Roberta S. Pugina[a,b], Avishek Das[a], Karmel O. Lima[b], Luiz Fernando dos Santos[b], Rogéria R. Gonçalves[b] and Anderson S. L. Gomes[a]
[a]Departamento de Física, Universidade Federal de Pernambuco, Recife, PE, 50901-640, Brazil;
[b]Departamento de Química, Faculdade de Filosofia, Ciências e Letras de Ribeirão Preto, Universidade de São Paulo, Ribeirão Preto, SP, 14040-90, Brazil

[3] T. de L. Pedrosa, G. M. F. de Oliveira, A. C. M. V. Pereira, M. J. B. da S. Crispim, L. A. da Silva, M. S. da Silva, I. A. de Souza, A. M. M. de A. Melo, A. S. L. Gomes, and R. E. de Araujo, Tailoring Plasmonic Nanoheaters Size for Enhanced Theranostic Agent Performance, Bioengineering **11**, (2024).

bioengineering

MDPI

Article

Tailoring Plasmonic Nanoheaters Size for Enhanced Theranostic Agent Performance

Túlio de L. Pedrosa [1], Gabrielli M. F. de Oliveira [1], Arthur C. M. V. Pereira [2], Mariana J. B. da S. Crispim [1], Luzia A. da Silva [3], Marcilene S. da Silva [4], Ivone A. de Souza [4], Ana M. M. de A. Melo [5], Anderson S. L. Gomes [2] and Renato E. de Araujo [1,*,†]

1 Laboratory of Biomedical Optics and Imaging, Federal University of Pernambuco, Recife 50740-540, Brazil; tulio.pedrosa@ufpe.br (T.d.L.P.); gabrielli.oliveira@ufpe.br (G.M.F.d.O.); mariana.crispim@ufpe.br (M.J.B.d.S.C.)
2 Department of Physics, Federal University of Pernambuco, Recife 50670-901, Brazil; arthur.messias@ufpe.br (A.C.M.V.P.); anderson.lgomes@ufpe.br (A.S.L.G.)
3 Graduate Program in Biological Sciences, Federal University of Pernambuco, Recife 50670-420, Brazil; luzia.abilio@ufpe.br
4 Laboratory of Pharmacology and Experimental Cancerology, Federal University of Pernambuco, Recife 50740-521, Brazil; marcilene.souza1989@gmail.com (M.S.d.S.); ivone.souza@ufpe.br (I.A.d.S.)
5 Department of Biophysics and Radiobiology, Federal University of Pernambuco, Recife 50670-901, Brazil; ana.mamelo@ufpe.br
* Correspondence: renato.earaujo@ufpe.br
† Current address: Department of Electronics and Systems, Federal University of Pernambuco, Recife 50740-540, Brazil.

[4] G. N. da S. A. O. Rocha, J. Y. R. Silva, D. K. D. do N. Santos, A. C. M. V. Pereira, J. V. R. Rocha, C. dos S. C. Alves, J. R. G. da S. Almeida, A. S. L. Gomes, A. F. Bakuzis, and S. A. Junior, Design of a magnetic nanocarrier containing phyllacanthone as delivery of anticancer phytochemical: Characterization and theranostic in vitro applications, J Alloys Compd **1010**, (2025).

Contents lists available at ScienceDirect

Journal of Alloys and Compounds

journal homepage: www.elsevier.com/locate/jalcom

Design of a magnetic nanocarrier containing phyllacanthone as delivery of anticancer phytochemical: Characterization and theranostic *in vitro* applications

Giovanna Nogueira da Silva Avelino Oliveira Rocha [a], José Yago Rodrigues Silva [a,*], Dayane Kelly Dias do Nascimento Santos [a], Arthur Césare Messias Viana Pereira [b], João Victor Ribeiro Rocha [c], Cristiane dos Santos Cerqueira Alves [d], Jackson Roberto Guedes da Silva Almeida [d], Anderson Stevens Leonidas Gomes [b], Andris Figueiroa Bakuzis [c], Severino Alves Junior [a,*]

[a] Department of Fundamental Chemistry, Federal University of Pernambuco, Recife, PE, Brazil
[b] Department of Physics, Federal University of Pernambuco, Recife, PE, Brazil
[c] Physics Institute, Federal University of Goias, Goiania, Brazil
[d] Center for Studies and Research of Medicinal Plants, Federal University of San Francisco Valley, Petrolina, PE 56304-205, Brazil

[5] C. P. Da Silva, R. T. F. Costa, A. C. M. V. Pereira, J. M. de L. Gomes, A. S. L. Gomes, S. L. D. Moraes, and D. S. Lopes, *Applicability of Terahertz Spectroscopy in Dentistry: A Scoping Review*, Oral Surgery, Oral Medicine, Oral Pathology and Oral Radiology.

Vol. 138 No. 5 November 2024

Applicability of terahertz spectroscopy in dentistry: a scoping review

Carolina Pereira Da Silva, DDS,[a] Rayanna Thayse Florêncio Costa, DDS, MSc,[a] Arthur Césare Messias Viana Pereira, MSc,[b] Jéssica Marcela de Luna Gomes, DDS, MSc, PhD,[c,d] Anderson Stevens Leônidas Gomes, MSc, PhD,[e] Sandra Lúcia Dantas Moraes, DDS, MSc, PhD,[a] and Daniela Siqueira Lopes, DDS, MSc, PhD[f]